UNIVERSITÀ DEGLI STUDI FIRENZE

PHD IN

INTERNATIONAL DOCTORATE IN ATOMIC AND MOLECULAR PHOTONICS

CYCLE XXXIII

COORDINATOR PROF. FRANCESCO SAVERIO CATALIOTTI

Solvation water role in driving structural conformation and self-assembly of peptides and proteins

---

Academic Discipline (SSD): CHIM/02 - FIS/03

Doctoral Candidate:

Dr. Sara Catalini

Supervisor:

Prof. Paolo Foggi

Co-Supervisor:

Prof. Renato Torre

Coordinator:

Prof. Francesco Saverio Cataliotti

Years 2017/2020

Contents

1 Introduction **1**

2 A survey of Resonance Raman and Transient Grating techniques **5**

2.1 Ultraviolet Resonance Raman Spectroscopy 6

2.1.1 Classical description of Raman scattering 7

2.1.2 Quantum mechanical description of Raman scattering 9

2.1.3 Resonance Raman scattering 11

2.1.4 Synchrotron set-up 18

2.2 Heterodyne Transient Grating Spectroscopy 21

2.2.1 Description of Transient Grating experiment 21

2.2.2 Four-wave mixing description 24

2.2.3 Optical set-up 31

2.2.4 Data collection and fitting procedure 33

3 Glutathione hydration in pure water and in water/salts mixtures **37**

3.1 Experimental methods 41

3.1.1 Samples preparation 41

3.1.2 UVRR spectra 41

3.1.3 MD simulations 42

3.2 Results and discussion 44

3.2.1 Influence of GSH on the water H-bond network 44

3.2.2 Dependence of Amide bands on pH and concentration 47

3.2.3 Deuteration and temperature effect on Amide bands 54

3.2.4 Ions effect on GSH structure and hydration 58

4 Self-assembly of lysozyme in self-crowded conditions **77**

4.1 Experimental methods 80

4.1.1 Solutions preparation 80

4.1.2 HD-TG experiments . . . 80
4.1.3 FTIR spectra . . . 81
4.1.4 CD spectra . . . 81
4.1.5 Micro-DSC thermograms . . . 81
4.1.6 Rheologcal experiments . . . 82
4.1.7 SAXS measurements . . . 82
4.1.8 SANS measurements . . . 82
4.2 Results and discussion . . . 83
4.2.1 Concentration effect on LYS structure . . . 83
4.2.2 Thermal unfolding of dilute LYS solution . . . 85
4.2.3 Thermal unfolding of LYS in self-crowded conditions . . . 88
4.2.4 Amyloid aggregation of LYS in self-crowded conditions . . . 97
4.2.5 Thermal aggregation kinetic and gelation of LYS . . . 108
4.2.6 Structural and elastic properties of LYS hydrogel . . . 112
4.2.7 Thermo-reversibility and oligomers dissociation of LYS hydrogel . . . 119

5 Conclusions **123**

6 Appendices **129**
6.1 A basic principals of SAXS and SANS . . . 129
6.2 List of publications . . . 131
6.3 List of conferences . . . 132
6.4 Experiences abroad . . . 134
6.5 Research activities at European large facilities . . . 135

Bibliography **137**

Chapter 1

Introduction

The term complexity derives from the Latin "*complexus*", meaning something intertwined, composed of a multiplicity of interdependent parts. A situation can be considered complex because it originates from the interconnection of elements that interact with each other. In a complex situation, it is difficult to identify and manage all the variables involved, just as it is extremely challenging to predict its developments. A problem that has been defined as complex does not present a unique solution, but needs to be considered globally, analysing all the elements that make it up and their interactions. The most famous definition of a complex system dates back to Aristotle who wrote in the work *Metaphysic "The whole is more than the sum of its parts*". Indeed, complex systems are intertwined networks, working in out-of-equilibrium conditions, which exhibit emergent properties, such as self-organization phenomena. Examples of complex systems are both the unicellular and multicellular living organisms, the brain network, immune system, ecosystems, human society, global economy, climate, cells and the biomolecules that compose them [1]. The ability to self-organize and spontaneously form dynamic and spatially variable structures is among the most intriguing features of living systems. The ability to form organized temporal and spatial architectures is peculiar of the whole organisms and tissues, but even occurs in the biomolecules that constitute them [2], like nucleic acids [3], carbohydrates [4], lipids [5], peptides and proteins [6]. This means that self-organization plays a fundamental role for the spatial and temporal organization of molecules inside cells [7]. Sadly, many of the mechanisms leading to biological pattern formation are not directly testable in a living system because the number of functional elements is enormous and it is impossible to reduce them without interfering with cell functionality. Therefore, the investigation of the single biomolecules that compose the cell and in vitro reconstitution approaches have become increasingly important. The idea is to reduce the system under investigation to the smallest possible combination of

molecules that is still able to reproduce a specific process or function, rigorously studying this system in order to highlight molecular mechanisms and recurring structuring paths. The purpose is to progressively increase the system complexity [7]. At this end, peptides and proteins are excellent models in order to approach at the complexity of biological systems. Peptides and proteins are dynamic systems and they must have a great structural flexibility to perform motions necessary to execute their functions. Motions are only possible if these biomolecules can assume a large number of different conformations, involving both the atoms composing the biomolecules and those of the solvation shell [8]. Structural dynamics and thus the activity of biomolecules are strongly influenced by the hydration shell, making the water molecules an active partner of all the biomolecules functions. The most relevant interactions are hydrogen bonds, a mainly local type of weak bonding among water molecules and between water and the polar or ionic groups of the biomolecule, long-range Coulomb forces, and hydrophobic forces. The hydrophobic contribution is less understood but still relevant for the aggregation properties of peptides and proteins. In recent years, the necessity to describe the properties of water next to biomolecules is increased, and the concept of hydration shell has been developed. Qualitatively, the hydration shell consists of the first or the first few water layers that surround the biomolecule influenced by and interacting with it. Moving away from the surface of the biomolecule, the water molecules increasingly display properties of bulk-like water. From the viewpoint of both structure and dynamics, the distinction of the hydration shell from bulk water poses major challenges and requires the combination of structure-sensitive and time-resolved spectroscopic technique [9] with computational methods to gain quantitative insight [10]. The hydration water plays a crucial role in protein folding, in their activity and even in determining the propensity toward aggregation of peptides and proteins [11]. Indeed the affinity of proteins for the solvent is quantified through the statistical thermodynamics by the solvation free energy (the change in free energy from gas to aqueous phases). The solvation free energy of the protein monomer quantifies the overall strength of the interactions between the protein and the water molecules that surround it, taking account for hydrogen bond, charged groups and hydrophobicity [12]. Hydrophobicity is often invoked to explain biomolecular self-assembly in aqueous media. Biomolecules with larger values of solvation free energy are more hydrophobic and the hydrophobic interaction between them is thus more effective promoting the aggregation phenomena [13]. Among the huge number of aggregation products, the most relevant are β-sheet oligomers and amyloid fibrils. Both

these products perform a key role for the onset of important degenerative diseases and/or for the development of smart biomaterials like hydrogels [6]. Amyloid fibrils and β-sheet oligomers are β-sheet rich and share a cross-β architecture. Fibres consist of β-strands that run perpendicular to the fibre axis and elongate in a preferential direction mainly via hydrogen bonding interactions between the main chain, but the association of the β-sheet is even stabilized by interactions between the side chains. The cross-β structure represents the core of the protofilaments, and several protofilaments associate laterally to form the mature fibril. Changes in the sequence of amyloidogenic fragments and in the solvation environment result in different morphologies arising from different packing arrangements [14]. Thanks to this structural tuneability the self-assembling peptides and proteins are increasingly used for the production of polymeric materials and hydrogels with applications spanning from tissue engineering [15] to agriculture [16]. Understanding the molecular basis of peptides and proteins organized aggregation lead to the possibility to exploit their self-assembling ability for the production of new functionalised biomaterials including hydrogel networks [14]. The aim of the present thesis is to achieve a deep comprehension of the effects that the presence of ions in solution, the different surface charge and temperature variation have on the distribution of water molecules around the molecular skeleton and on the structure of biomolecules and its aggregates. In addition I want to exploit the capability of linear and some non-linear spectroscopic techniques and compare their results to those obtained with different techniques like neutron and x-ray scattering techniques. After this introductory chapter, the thesis is organized as follows.

Chapter 2 deals with the basic theory of UV resonance Raman (UVRR) and heterodyne transient grating (HD-TG) techniques. The experimental set-ups used during this PhD period are described. As already mention the characterization of these complex biological systems are achieved by combining several experimental techniques and the specific topics are briefly described in the specific chapters.

Chapter 3 reports the outputs obtained about the tripeptide glutathione dissolved in pure water and salts/water mixture investigated by means of the UVRR spectroscopy and the computational method of molecular dynamics (MD). The UVRR measures are performed in the *IUVS* beamline of *Elettra Synchrotron* in Trieste headed by Dr. Claudio Masciovecchio, and the MD simulations are carried out by the group of Prof. Babak Minofar at the *Institute of Nanobiology and Structural Biology* in the Czech Republic.

Chapter 4 focuses on a lysozyme self-crowded solution in acidic conditions to investigate

globular protein unfolding, aggregation and gelation through a multi-technical approach. In particular using Fourier transform infrared (FTIR) and circular dichroism (CD) spectroscopies to have molecular information on these processes. The differential scanning calorimetry (DSC) technique to investigate the thermodynamics of the unfolding process. Small angle x-ray scattering (SAXS) and small angle neutron scattering (SANS) techniques are used to approach the problem from a structural point of view. Rheology and HD-TG spectroscopy to investigate the viscoelastic behaviour of self-crowded protein solution and protein hydrogels. The FTIR spectra are performed in the *Department of Chemistry, Biology and Biotechnology* of the university of Perugia, in the research group of Prof. Assunta Morresi and Prof. Paolo Foggi. Rheology and DSC measurements are performed in the *School of Pharmacy* at the university of Camerino in the research group of Prof. Giovanni F. Palmieri. SAXS and CD measures are made at the *ETH* of Zurich in the *Laboratory of Food and Soft Materials* of Prof. Raffaele Mezzenga. SANS experiments are carried out at the *Budapest Neutron Center*. HD-TG experiments are performed in the *Soft Matter Physics Group* of Prof. Renato Torre at *LENS*.

Chapter 2

A survey of Resonance Raman and Transient Grating techniques

This chapter describes the UV resonance Raman and the transient grating spectroscopic techniques. Section 2.1 presents conventional and resonance Raman scattering. Section 2.2 describes the non-linear transient grating spectroscopy. Spontaneous light scattering means light scattering under conditions such that the optical properties of the material system are unmodified by the presence of the incident beam, while the character of the light scattering is profoundly modified whenever the incident light is sufficiently intense to modify the optical properties of the material system. Figure 2.1 shows the general scheme of the scattered light spectrum, in which Raman, Brillouin, Rayleigh and Rayleigh-wing spectral features appear [17].

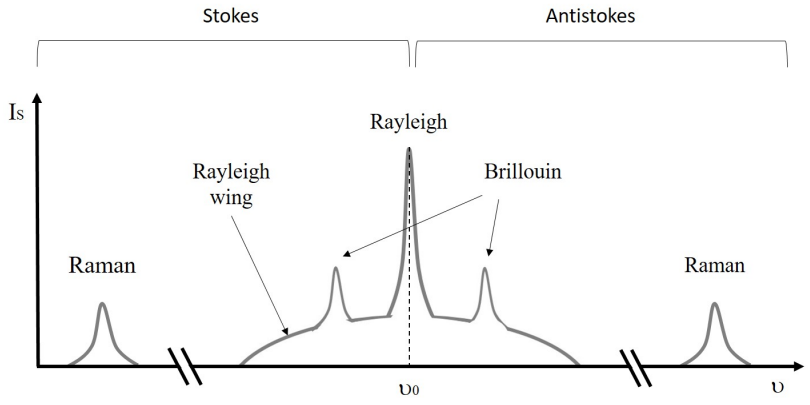

FIGURE 2.1: Typical observed spectrum of the scattered light.

Rayleigh scattering is the scattering of light from non propagating density fluctuations, described as scattering from entropy fluctuations. It is known as quasi-elastic scattering because it induces a slight frequency broadness.

Rayleigh-wing scattering is scattering from fluctuations in the orientational of anisotropic

molecules; this phenomenon does not occur for molecules with an isotropic polarizability tensor.

By definition the components of the scattered light that are shifted to lower frequencies with respect to the central Rayleigh component are named Stokes components and those that are shifted to higher frequencies are known as Antistokes components.

One of these scattering process is the *Raman scattering*, that results from the interaction of light with the vibrational modes of the molecule constituting the scattering medium. Raman scattering can be described as the scattering of light by optical phonons [17].

Brillouin scattering is the scattering of light from sound waves, which is from propagating pressure (and thus density) waves. Brillouin scattering can also be considered to be the scattering of light from acoustic phonons.

In spontaneous Raman and Brillouin scattering the applied optical fields are sufficiently weak that they do not alter the optical and the acoustic properties of the material system. Whereas in the framework of the impulsive stimulated scattering experiment, depending on the molecular modes which are excited, the experiments have different name. In particular, if the acoustic modes are excited through the electrostrictive effect, it is possible to talk about *impulsive stimulated Brillouin scattering*, while, if the excitation involve optical phonons and molecules vibrational modes, the experiment is called *impulsive stimulated Raman scattering* [18].

2.1 Ultraviolet Resonance Raman Spectroscopy

In conventional Raman scattering, the incident photons have a frequency lower than electronic transitions, and the inelastically scattered photons, leave the molecule in an excited vibrational level of the electronic ground state. The same mechanism takes place in resonance condition, but in this case the incident photon frequency matches electronic transitions, and the molecular vibrations couple to the electronic motion occurring during the transition. In resonance Raman scattering, only the vibrations localized around the chromophoric group are enhanced, making a simplification in the number of signals present in the spectrum. Appropriately tuning the excitation wavelength, it is possible to increases the signal intensity of the vibrational bands, originated from a particular region of the molecule.

This section is aimed to provide the theoretical basis of the Raman scattering, and to highlight the differences and the advantages in using excitation beams with sufficient energy to generate the resonance condition.
Subsections 2.1.1 and 2.1.2 formally introduce the Raman scattering process, using classical and quantum theory, respectively. Subsection 2.1.3 mathematically describes the intensity increases in the resonance Raman compared to the off-resonance one, specifying the advantages and limitations of the resonance condition. Section 2.1.4 highlights the importance to use sources that allows the fine tuning of the excitation wavelength, and therefore the use of a synchrotron source [19].

2.1.1 Classical description of Raman scattering

Light scattering phenomenon refers to the process in which the incident photons with characteristic energy and momentum are diffused by matter. In the scattering process the oscillating electric vector of the electromagnetic field interacts with matter and induces on the molecules an oscillating electric dipole moment $(\bar{\mu})$ that becomes a new emitting source of electromagnetic field that is the scattered light [20]. The induced electric dipole momentum is proportional to the incident electric vector $(\bar{E})$ and to the capacity of the molecules to deform its electronic cloud; this quantity is a tensor called polarizability (α). We can define the *elastic scattering* when the incident photon energy is the same of the diffused one, while we refer to *inelastic scattering* when there is an energy variation.

$$\bar{\mu} = \hat{\alpha}\bar{E} \tag{2.1}$$

Each component of the induced dipole can be expressed as:

$$\mu_\rho = \sum_{\sigma=x}^{z} \alpha_{\sigma\rho} E_\sigma \tag{2.2}$$

Each component of $\bar{E}$ can be related to the ν_0 frequency of the incident electromagnetic wave by the relation:

$$E_\sigma = E(0)_\sigma \cos(2\pi\nu_0 t) \tag{2.3}$$

Consequently, the induced dipole is an oscillating vector and each of its components can be obtained combining equations 2.2 and 2.3 by the relation:

$$\mu_\rho = \sum_{\sigma=x}^{z} \alpha_{\sigma\rho} E(0)_\sigma \cos(2\pi\nu_0 t) \tag{2.4}$$

To make the explanation easier, it is useful to ignore the molecular rotation but just consider the vibrational part, and it is to be expected that the polarizability will be a function of the nuclear coordinates. Therefore, the 3N-6 (3N-5) vibrational modes are supposed to induce a variation in this quantity. For a diatomic molecule with the single normal coordinate (Q_k), the position of the nuclei is time dependent because the molecule is vibrating with frequency (ν), and the motion can be expressed as:

$$Q_k = Q(0)_k \cos(2\pi\nu t) \tag{2.5}$$

The variation of components in polarizability tensor $(\alpha_{\rho\sigma})$ with vibrational coordinates (Q_k) is expressed in a Taylor series expansion:

$$\alpha_{\rho\sigma} = \alpha(0)_{\rho\sigma} + \sum_k \left(\frac{\partial\alpha_{\rho\sigma}}{\partial Q_k}\right)_0 Q_k + \frac{1}{2}\sum_{k,l}\left(\frac{\partial^2\alpha_{\rho\sigma}}{\partial Q_k \partial Q_l}\right)_0 Q_k Q_l + ... \tag{2.6}$$

By keeping only the first two terms of the Taylor series, the components of the induced dipole of relation 2.4 can be redefined as:

$$\begin{aligned} \mu_\rho(Q_k) &= \sum_{\sigma=x}^{z} \alpha(0)_{\sigma\rho} E(0)_\sigma \cos(2\pi\nu_0 t) \\ +\frac{1}{2}\sum_{\sigma=x}^{z} E(0)_\sigma Q(0)_k &\left(\frac{\partial\alpha_{\rho\sigma}}{\partial Q_k}\right)_0 [\cos 2\pi t(\nu_0+\nu) + \cos 2\pi t(\nu_0-\nu)] \end{aligned} \tag{2.7}$$

By looking to the expression above, the radiation emitted by the oscillating dipole induced by the incident electromagnetic field on the molecule have three different components:

1. $\sum_{\sigma=x}^{z} \alpha(0)_{\sigma\rho} E(0)_\sigma \cos(2\pi\nu_0 t)$ that accounts for Rayleigh or elastic scattering;
2. $+\frac{1}{2}\sum_{\sigma=x}^{z} E(0)_\sigma Q(0)_k \left(\frac{\partial\alpha_{\rho\sigma}}{\partial Q_k}\right)_0 [\cos 2\pi t(\nu_0+\nu)]$ that accounts for Anti-Stokes Raman scattering;
3. $+\frac{1}{2}\sum_{\sigma=x}^{z} E(0)_\sigma Q(0)_k \left(\frac{\partial\alpha_{\rho\sigma}}{\partial Q_k}\right)_0 [\cos 2\pi t(\nu_0-\nu)]$ that accounts for Stokes Raman scattering.

For a given vibrational mode (i. e. at a fixed frequency of detection) the Raman scattering total intensity will be defined as [19, 21]:

$$I(\Theta) = B(\nu_0 \pm \nu)^4 I_0 \left(\frac{\partial \alpha_{\rho\sigma}}{\partial Q_k}\right)_0^2 \sin^2 \Theta \tag{2.8}$$

The Raman scattering intensity is dependent on:

1. The kind of vibrational motion and on its impact on the molecular electron cloud by mean of $\left(\frac{\partial \alpha_{\rho\sigma}}{\partial Q_k}\right)_0^2$
2. The incident radiation energy by means of $(\nu_0 \pm \nu)^4$

From the classic theory, the intensity of the scattered radiation is proportional to the fourth power of the frequency and to the square of the maximum oscillation amplitude, hence the intensity of the Rayleigh radiation is proportional to λ_0^2 and the intensity of the Raman radiation at $\left(\frac{\partial \alpha_{\rho\sigma}}{\partial Q_k}\right)_0^2$. Therefore, it is immediately visible how the Rayleigh scattering is more intense than the Raman one. However, the classical approach to the Raman effect fails in the prediction of the Stokes and Anti-Stokes intensities ratio, and we need to the quantum mechanical approach to explain that.

2.1.2 Quantum mechanical description of Raman scattering

According to the quantum theory, a radiation is emitted or absorbed as a result of the energy transfer between the electromagnetic field and the molecule due to their interaction. The quantum-mechanical description of the scattering process of the electromagnetic wave with energy $E = h\nu_0$ induced by the molecule can be schematized as follows:

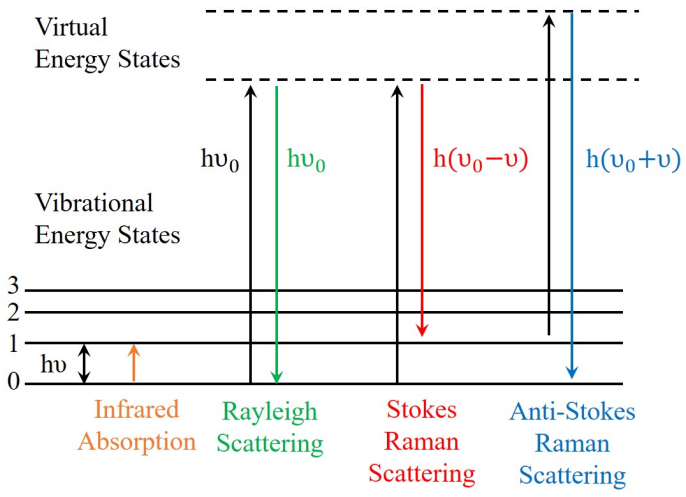

FIGURE 2.2: virtual energy diagram to compare the elastic and the two inelastic scattering processes.

Figure 2.2 shows a virtual energy diagram that evidences the difference between Rayleigh scattering, Stokes Raman scattering and Anti-Stokes Raman scattering.

1. Rayleigh scattering $E = h\nu_0$: is the term that describes the quasi-elastic scattering of light by molecules and is the most dominant scattering process. The interaction light-matter does not change the energy state of the molecule and therefore the scattered photons have the same energy as the incident ones. In a Raman experiment, the Rayleigh scattered light must be removed from the collected light otherwise it would cover the Raman signals.

2. Stokes Raman scattering $E = h(\nu_0 - \nu)$: is the inelastic scattering process where there is an energy transfer from the electromagnetic wave to a molecule's vibrational degree of freedom. Hence, the scattered photons have a lower energy (red shifted) compared to the incident ones. The amount of transferred energy is equal to the amount necessary to excite one of the molecule's vibration. The composition of the scattered light is therefore like a fingerprint of the molecules. The Stokes component is the most commonly acquired in a Raman experiment because, although its intensity is about 10^{-10} times lower than the excitation light, it remain the most intense component containing molecular information.

3. Anti-Stokes Raman scattering $E = h(\nu_0 + \nu)$: is another inelastic scattering process, where a specific amount of energy is transferred from a molecular vibration to the photon. Hence, the scattered photons have higher energy (blue shifted) compared to the incident ones. This component contains the same molecular information of the Stokes component, but is less intense; in fact, it is generally unused.

The virtual energy diagram points out that the Stokes Raman scattering is more probable than the Anti-Stokes one, because at room temperature most molecules are in their ground state. However, with increasing temperature, more of the molecules can access to the vibrational excited state, in accordance with the Boltzmann distribution. In quantum mechanics any direct transition between two energy levels is accompanied by emission or absorption of radiation if the dipole moment of the transition is $\neq 0$. Hence, a transition from an initial state described by the wave function Ψ_i to a final state Ψ_f must induce a variation of the molecular dipole moment during the transition i.e. [19]:

$$\mu_{fi} = \langle \Psi_f | \hat{\mu} | \Psi_i \rangle \neq 0. \tag{2.9}$$

$\hat{\mu}$ is the dipole moment operator and for absorption or emission phenomena corresponds to the permanent electric dipole operator, while for the scattering process is the induced dipole moment operator. For scattering process using the relations 2.1 and 2.9 the dipole moment of the transition becomes:

$$\mu_{fi} = \langle \Psi_f | \hat{\alpha} | \Psi_i \rangle \bar{E} \tag{2.10}$$

In the quantum mechanical approach the term $\left(\frac{\partial \alpha_{\rho\sigma}}{\partial Q_k}\right)_0$ in the intensity equation 2.8 must be replaced by the Raman scattering tensor $[\alpha_{\rho\sigma}]_{fi}$ in order to have a rigorous description of $I(\Theta)$.

The expression of the Raman scattering tensor is obtained accordingly to the Kramers, Heisenberg and Dirac theory [22, 23]:

$$[\alpha_{\rho\sigma}]_{fi} = \frac{1}{hc} \sum_v \frac{\langle \Psi_f | \hat{\mu_\rho} | \Psi_v \rangle \langle \Psi_v | \hat{\mu_\sigma} | \Psi_i \rangle}{\nu_v - \nu_0 - \nu_{exc} + i\Gamma_v} + \frac{\langle \Psi_f | \hat{\mu_\sigma} | \Psi_v \rangle \langle \Psi_v | \hat{\mu_\rho} | \Psi_i \rangle}{\nu_v - \nu_0 + \nu_{exc} + i\Gamma_v} \tag{2.11}$$

Ψ_i and Ψ_f are the vibrational wave functions of the ground electronic level of a starting (i) vibrational level and a final (f) one.

Ψ_v is the vibrational wave function describing the virtual state, the summation operates on all the vibrational states of the system.

Γ_v is the width of the band associated with the $|\Psi_v\rangle$ vibrational state.

Usually in a conventional Raman experiment the energy of the excitation beam ν_{exc} does not coincide with any transition frequency and in these conditions the Raman associated signal to a given normal mode is weak.

2.1.3 Resonance Raman scattering

Talking about Raman intensity it is necessary to distinguish between conventional and resonance Raman scattering. In both cases, Raman spectroscopy is a fundamental state spectroscopy since the transition occurs between vibrational states of the electronic ground state. The difference is that in conventional Raman the electronic excited states take part to the process as virtual intermediate states, while in resonance Raman as real intermediate states. In this latter the frequency of the exciting beam falls into an electronic absorption band, therefore the Raman intensities become a very specific and sensitive probe of the structure and dynamic of the electronic resonant states.

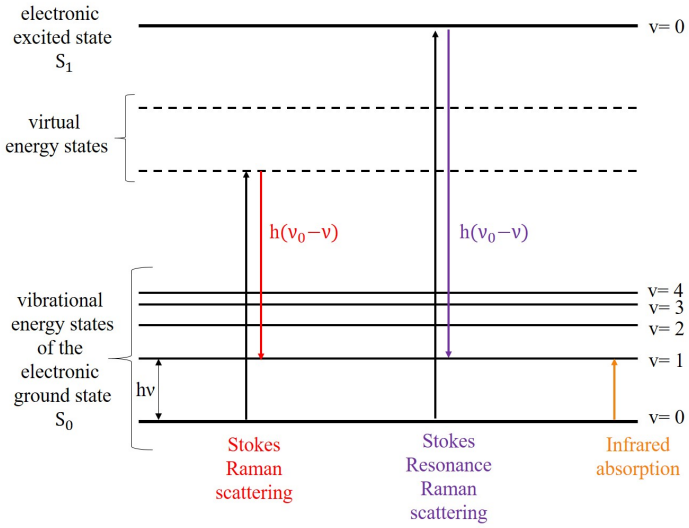

FIGURE 2.3: virtual energy diagram to compare the conventional and the resonance Raman scattering.

In the equation 2.11 the summation operates on all the vibrational states of the system, and the summation on (v) is required to describe an intermedium state that is not a system eigenstate.

In non-resonant condition, the molecular polarizability is the result of the linear combination between all the system states, and the interaction with the exciting photon will originate only a slight perturbation on the equilibrium condition. Instead, in resonance condition, the energy difference on the denominator of the first term of the equation 2.11 tends to zero, and the condition of slight perturbation is not valid anymore, therefore it is necessary to consider the incident photon degeneration with the excited state that acts as intermediate state. Because $(\nu_v - \nu_0 - \nu_{exc}) \rightarrow 0$ the first term of the equation 2.11 in resonance condition become dominant and the relation can be simplified to [19, 21]:

$$[\alpha_{\rho\sigma}]_{fi} = \frac{1}{hc} \sum_v \frac{\langle \Psi_f | \hat{\mu_\rho} | \Psi_v \rangle \langle \Psi_v | \hat{\mu_\sigma} | \Psi_i \rangle}{\nu_v - \nu_0 - \nu_{exc} + i\Gamma_v} \tag{2.12}$$

Notice that in the resonance Raman condition $[\alpha_{\rho\sigma}]_{fi}$ should become greater than in conventional Raman condition, due to the smallness of the denominator. In this condition I(q) of the associated normal mode should be enhanced. The imaginary part that appears in the denominator of the expression 2.12 considers that in resonance condition the effect of the electromagnetic perturbation is related also to the life time of the excited state, hence Γ is a quantity inversely proportional to the life time of the vibrational excited states v. Exciting an electronic transition of a specific chromophore, some normal modes result intensified more than others. Therefore, in resonance condition the spectrum of a sample can be very

different compared to those out of resonance. The resonant active Raman signals can result orders of magnitude higher (from 3 to 8 order of magnitude) than those in out of resonance. Indeed, in resonant condition, the sensibility of the technique increases a lot and this is very useful to analyse heterogeneous sample. Using the resonance condition, it is possible to record in a selective manner the signals of a molecular portion of the sample or a specific component in a complex mixture [20, 24]. The terms at the numerator of equations 2.11 and 2.12 can be explicated depending on the validity of the following approximations:

1. *Born-Oppenheimer approximation*

   This approximation allows separating the nuclear motion from electronic one, considering the nuclei in a fixed position during the electronic motion. Therefore, the vibrionic terms can be factorized in the product between electronic and vibrational states $\langle \Psi_v | \hat{\mu_\rho} | \Psi_i \rangle = \langle \varphi_v | \langle \phi_v | \hat{\mu_\rho} | \phi_i \rangle | \varphi_i \rangle$.

   ϕ_i and ϕ_v are the electronic wave functions of the ground and excited states respectively, while φ_i and φ_v are the respective vibrational functions.

2. *Condon approximation*

The validity of the Born-Oppenheimer approximation implies the possibility to assume that the electronic transition occurs instantaneously into the temporal scale of the nuclear vibration, hence for constant inter-nuclear distance. The transition probability is proportional to the superposition integral between the vibrational wave functions of the two different electronic states. Therefore, the transition moment considering the electronic part is much higher compared to its variations due to the vibrational mode, hence it is possible to approximate it with the pure electronic transition moment $(\bar{R}_e)$. Only the vibrational levels of the resonant electronic state give an important contribute at the sum on the intermedia states. If these approximations are valid, it is possible to write the following equation (A Albrecht term) [19, 21]:

$$[\alpha_{\rho\sigma}]_{fi}(\lambda_{exc}) = (\bar{R}_e)^2 \frac{1}{hc} \sum_v \frac{\langle \varphi_f | \varphi_v \rangle \langle \varphi_v | \varphi_i \rangle}{\nu_v - \nu_i + \nu_0 - \nu_{exc} + i\Gamma_v} \tag{2.13}$$

The absorption cross section has the following expression:

$$\sigma_A(E_{exc}) = CE_L(\bar{R}_e)^2 \sum_v \frac{\Gamma}{(hc)^2\pi} \frac{|\langle \Psi_f | \Psi_v \rangle|^2}{(\nu_v - \nu_i + \nu_0 - \nu_{exc})^2 + \Gamma^2} \tag{2.14}$$

The absorption cross section depends on the same exciting state parameters of the Raman cross section, but in equation 2.13 the initial and final states of the transition are defined, while equation 2.14 reports the transition probability at some indefinite final state. Based on the analogies between equations 2.13 and 2.14 it is easy to state that the active modes on the electronic transition $f \leftarrow i$ have comparable activity in the absorption spectra and in the correspondent resonance Raman spectra. Some modes that are inactive in absorption or in emission can show resonance Raman activity.

Resonance condition

To understand when the superposition integrals are non-zero, it is sufficient to consider the harmonic oscillator and the symmetry of the normal modes. The resonance Raman process is represented describing the ground and excited electronic states as an harmonic potential, as shown in figure 2.4.

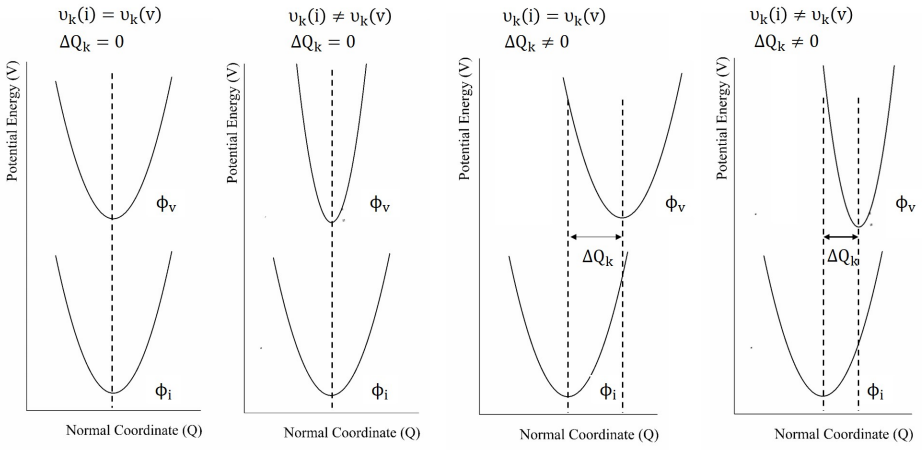

FIGURE 2.4: diagrams of the potential energy (V) as a function of the normal coordinate (Q) of the ground Φ_i and excited Φ_v electronic states.

In correspondence of a fundamental band of the Raman spectra, the transitions from the ground state i=0 at the intermediate states and from the intermediate states to the final state f=1, is non-zero if:

1. the potential curves of the involved electronic states are shifted with each other $\Delta Q_k \neq 0$
2. the mode frequency of the two states changes $\nu_k(i) \neq \nu_k(v)$
3. both the above conditions are satisfied

Totalsymmetric modes

Considering the validity of the Condon approximation, only the totalsymmetric modes

show Raman activity and the resonance Raman spectra are mainly due to the terms described in equation 2.13, the A Albrecht term.

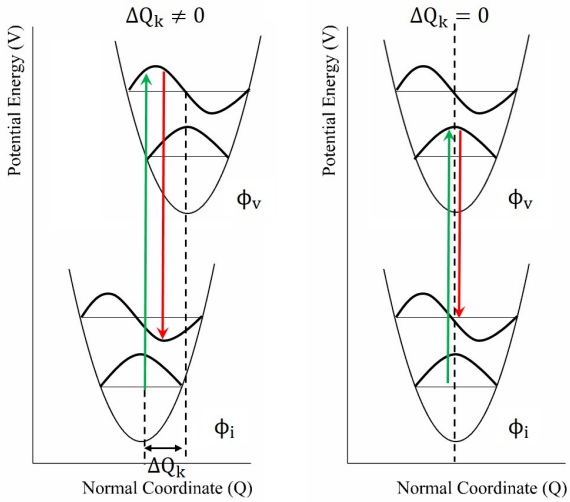

FIGURE 2.5: potential curves (V) that highlights the dependence of the integral superposition as a function of the normal coordinate (Q), in the validity of the Frank-Condon approximation.

As regards the totalsymmetric modes, the inter-nuclear distance changes $\Delta Q_k \neq 0$ during the vibration, and the electronic ground and excited state curves are shifted with each other, hence there is always a case where both superposition integrals are non-zero, as shown in the left graph of figure 2.5. Concerning the non-totalsymmetric modes, the inter-nuclear distance does not change $\Delta Q_k = 0$ during the vibration and the curves have the same equilibrium position, therefore a condition that simultaneously makes the integral superposition non-zero doesn't exist, as shown in the right graph of figure 2.5. Therefore, considering the A Albrecht term, only the totalsymmetric modes are active in the resonance Raman spectra, but the Condon approximation is not always valid. Indeed considering the vibronic coupling it is necessary to take account also of the B and C Albrecht terms that are the responsible of the non-totalsymmetric modes activity.

Non-Totalsymmetric modes

The Non-totalsymmetric modes activity is due to the vibronic coupling phenomenon between the electronic excited states by means of the normal coordinate (Q). The normal coordinate must be non-totalsymmetric. This coupling between the electronic excited states is explicated in the electronic component of the transition momentum:

$$R_{vi} = R_{vi}^{0} + \left(\frac{\partial R_{vi}}{\partial Q_k}\right) Q_k + ... \tag{2.15}$$

It is possible to write the forward and backward transitions in the following formalism:

$$\begin{aligned}\langle \Psi_v|\hat{\mu}_\sigma|\Psi_i\rangle &= R^0_{vi}\langle\varphi_v|\varphi_i\rangle + R^I_{vi}\langle\phi_v|\phi_i\rangle \\ \langle \Psi_f|\hat{\mu}_\sigma|\Psi_v\rangle &= R^0_{vi}\langle\varphi_f|\varphi_v\rangle + R^I_{vi}\langle\phi_f|\phi_v\rangle\end{aligned} \tag{2.16}$$

Considering the relations 2.15 and 2.16 it is possible to write the Albrecht terms:

$$\begin{aligned}A &= (R^0_{vi})^2\langle\phi_v|\phi_i\rangle + \langle\phi_f|\phi_v\rangle \\ B &= R^0_{vi}\langle\phi_v|\phi_i\rangle R^I_{vi}\langle\phi_f|Q|\phi_v\rangle \\ C &= R^0_{vi}\langle\phi_f|\phi_v\rangle R^I_{vi}\langle\phi_v|Q|\phi_i\rangle\end{aligned} \tag{2.17}$$

The B and C Albrecht terms reproduce a non-vertical transition (in absorption or in emission). This is possible because there is a vibronic coupling that acts. A non-totalsymmetric normal coordinate couples the two electronic excited states. This describes a phenomenon of equilibrium geometry distortion in concomitance of the absorption or emission processes as shown in the figure 2.5.

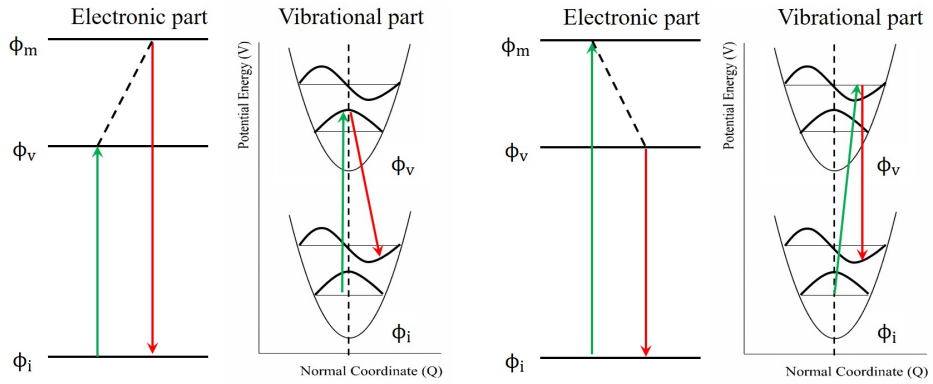

FIGURE 2.6: diagrams that illustrate the vibronic coupling in emission mathematically described by the B Albrecht term (left part) and in absorption mathematically described by the C Albrecht term (right part).

Advantages and limitations

The main problem to exploit the resonance condition is related to the possibility to observe the scattering phenomena and the emission process together. Usually the intensity of the emitted light is higher than the diffused one, hence it is possible that the resonance Raman spectra is completely covered by the emission signal. The *fluorescence emission* can be reduced changing the excitation wavelength, and realizing a pre-resonance condition. In

some cases, it is also possible to record the Anti-Stokes part of the Raman spectra because the emission process occurs at lower frequencies than the excitation, therefore the emission intensity is reduced in the Anti-Stokes branch. In a resonance Raman experiment it is possible that a portion of the scattered light is reabsorbed by the sample. This phenomenon reduces the total scattered light because it is self-absorbed by the molecules in the scattering volume. Due to *self-absorption*, it is even possible to have a change of the peaks relative intensity. Another problem of the resonance Raman experiment is the possibility of the sample *photo degradation*, due to the focalization of the beam in a small volume. To avoid the sample damage it is better to maintain an adequate excitation power of the beam and continually renewing the sample's illuminated volume, using a flow cell or oscillating/rotating the sample holder.

On the other hand, the vibrational spectroscopic techniques are powerful tool to study the molecular structural changes induced by chemical reactions or by external stimuli. This kind of analysis are useful to take out *qualitative* and *quantitative information* of the investigated sample. Indeed, it is possible to apply them in a lot of research fields spanning from analytical to biological ones. Compared to infrared absorption, both conventional and resonance Raman are considered powerful techniques to study *water-containing sample* due to water's low polarizability. In fact, to study biologic molecules in physiologic condition, it is recommended to use water as a solvent and to collect the measurement directly in the natural environment with the minimum sample preparation, in order to avoid the human interference. Unfortunately water has a great infrared absorption and the OH banding signal covers a spectral region where the main signals of peptides and proteins [25] [26] fall. To avoid this problem scientists use deuterium oxide instead of light water because the OD bending signal falls at different frequency. Using Raman techniques it is possible to analyse aqueous solution without the necessity of isotopic substitution due to the very low intensity of the OH banding signal in Raman spectra. Using Raman technique it is possible to investigate samples in the gaseous, liquid and solid state, and due to its *non-destructive* nature, it is a great candidate to investigate delicate materials. Resonance Raman spectroscopy has greater *sensitivity* with respect to its non-resonance counterpart. It is capable of analysing samples with concentrations lower than 10^{-8} M, while conventional Raman can detect samples with concentrations not lower than 0.1 M. Resonance Raman technique produces simplified spectra compared to non-resonance one (relatively few signals). The reason is that exploiting the resonance condition the enhanced signals are only those affiliated with the

chromophores of the sample, giving to this technique a unique *selectivity*. This is very useful to analyze samples with a very complex composition and follow only a precise species, or to investigate molecules with large structures like biomolecules. Monochromatic radiation in the ultraviolet region is generally used for resonance Raman spectroscopy, and a tuneable source like a synchrotron is preferable. Indeed, only one laser is not sufficient to investigate multiples samples in which each one requires a different excitation wavelength. Synchrotron sources allows the user to switch the excitation wavelength as near as possible to the chromophore's electronic transition. By means of resonance Raman spectroscopy, it is also possible to record the excitation profile of a particular Raman active mode. In fact, for each Raman active mode, it is possible to follow the signal intensity variation as a function of the excitation frequency into the absorption band. The result, called excitation profile, reproduces the vibronic transition associated with the particular normal mode, before that the system relaxes from the electronic excited state levels. To perform this kind of experiment a tuneable and highly monochromatic source, like synchrotron one, is requested.

2.1.4 Synchrotron set-up

UV Resonance Raman (UVRR) spectroscopy is a very valuable tool for collecting chemically specific information about a large variety of systems, due to the fact that organic molecules exhibit many and strong absorption transitions in the UV range. However, the full exploitation of UVRR spectroscopy would require to overcome some critical issues, manly related to the need of UV sources with appropriate characteristics.

1. Until now, little is known about the electronic transitions that occur in the UV region below 7 eV ($\approx$ 180 nm) due also to the difficulty of vacuum-UV spectral measurements required for exploring this range. The importance of extending the UV domain lies in the possibility to cover the whole range of outer electronic transitions in matter (i.e. up to $\approx 10 - 15$ eV) by selectively exploring specific orbitals and bands.

2. By using a continuously tunable excitation source it is possible to map the whole resonances range of the sample in order to achieve a fine matching between the exciting radiation energy and the resonance conditions of specific chromophores. This allows to perform, for examples, accurate UVRR measurements not biased by self-absorption effects.

The optical set-up developed at the BL10.2-IUVS beamline (Elettra synchrotron facility, Trieste, Italy) exploits a tunable UV synchrotron radiation (SR) source for exciting and collecting UVRR spectra from different kinds of samples, i.e. solids, liquids and gels.
Figure 2.6 shows the technical layout of the instrument [27].

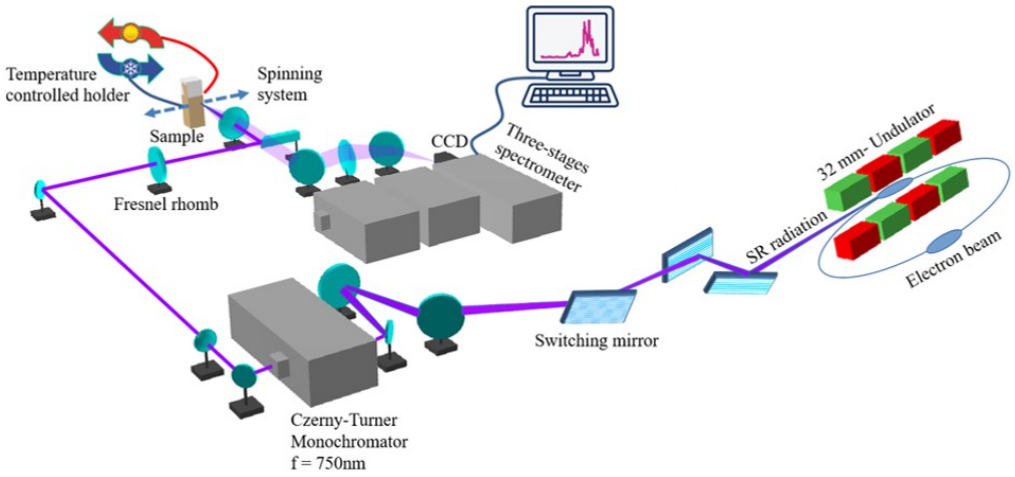

FIGURE 2.7: Technical layout of the SR-based set-up for UVRR measurements at BL10.2-IUVS beamline (Elettra synchrotron facility, Trieste, Italy).

The 32 mm undulator inserted in the radiation source of the beamline generates linear polarized SR with energy ranging from 4.4 to 11 eV (corresponding to wavelengths between about 113 and 280 nm) [28]. The main advantage of this undulator design is the strong reduction of the total on-axis power density that is achieved with no penalty on the useful photon flux in the first harmonic of the emission spectrum. The beam coming from the SR source is cleaned from the higher order harmonics of the undulator through two mirrors. A first gold coated GLIDCOP, internally water-cooled, deviates the photons in the vertical plane with an angle of 60° and a second externally water-cooled silicon mirror is used to bring back the beam parallel to the floor. Finally, a silicon switching mirror is used to guide the SR to the UVRR stage instead of the conventional high resolution inelastic UV scattering (Brillouin) spectrometer. Suitable UV-enhanced coating mirrors (with reflectivity of 90% in the whole range 250–185 nm) are used to route and focus the SR radiation into the entrance slits of the monochromator (see figure 2.7). Overall the transport system delivers to the monochromator UV radiation with power of $\approx$ 10 mW (at $\lambda = 270$ nm of wavelength) with a typical bandwidth of $\frac{\Delta\lambda}{\lambda} \approx 0.01$, corresponding to $\approx 350\ cm^{-1}$. The SR radiation is monochromatized trough a Czerny-Turner monochromator (Acton SP2750 produced by Princeton instruments) operating with three exchangeable flat holographic gratings with

1800, 2400 and 3600 groves/mm. The maximum wavelength resolution at 270 nm provided by the monochromator is $\approx$ 0.012 nm which corresponds to a half-width of $\approx$ 1.6 cm^{-1}. After the monochromatization, the UV beam is collimated by a lens and transported to the Raman analyzer system and the incident beam is focused on the sample and collected in back-scattering configuration trough plan-convex lens and mirrors. In this configuration the typical size of the beam spot on the sample is of few mm^2. The Raman signal is analyzed by a three-stages spectrometer (TriVista 557, Princeton Instruments) where each stage is equipped with a selection of flat holographic gratings (1800 and 3600 groves/mm) optimized for both UV and visible radiation. Finally, the scattered photons are detected by a peltier-cooled UV-enhanced CCD camera. The calibration of the spectrometer is standardized using cyclohexane. Polarized parallel (VV) and depolarized orthogonal (HV) UV Raman spectra can be collected by inserting in the optical path a Fresnel Rhomb Retarders (Half-Wave Retardance with broader wavelength range) and polarizers (see Figure 2.7).

2.2 Heterodyne Transient Grating Spectroscopy

In spontaneous Brillouin scattering the applied optical fields are sufficiently weak that they do not alter the acoustic properties of the material system, and the incident radiation is scattered by the sound waves that are thermally excited. Whereas in impulsive stimulated Brillouin scattering the excitation laser fields are sufficiently intense that they are able to give rise to density and pressure variations by means of the electrostrictive effect. The probe laser field is then scattered by the refractive index variation that accompanies these density variations [17]. The Tranisient Grating experiment can be complexly described as an impulsive stimulated Brillounin scattering event.

In this section the Transient Grating experiment is described giving some theoretical background, and describing the problem in the context of Four-Wave Mixing (FWM). More specifically, the subsection 2.2.1 introduces the Transient Grating experiment, which is theoretically described in the subsection 2.2.2. The last two parts, 2.2.3 and 2.2.4, describe the experimental details in terms of the used optical set-up, the data collection and the fitting procedure [18].

2.2.1 Description of Transient Grating experiment

At the end of the 1970s it has been discovered that it was possible to take access to important information on the dynamical properties of a material [29, 30], probing the relaxation of the spatial periodic modulation of its optical properties, previously induced by the interference field of two pump beams [31]. This kind of experiment takes the name of Transient Grating (TG) Spectroscopy.

In a TG experiment a single high power laser beam is divided in two pulses. These two excitation pulses, E_{exc1} and E_{exc2}, interfere and produce into the sample an impulsive spatial modulation of the material optical properties (i.e. index of refraction and absorption coefficient). The induced modulation of the optical properties of the material, is probed through a continuous-wave (CW) third beam, where the whole temporal response is recorded in a single laser shot. This peculiarity enlarges the temporal window of the experiment from nanoseconds to milliseconds, allowing to cover a wide range of scale times, over which the polymers and gels relaxation dynamics occur.

The pump beams produce two acoustic pressure waves (i.e., two longitudinal bulk ultrasonic waves), which counter-propagate in the q-direction; their superposition creates a stationary wave. The probe beam is scattered by the standing wave, which produces the oscillations in the acoustic signal. A schematic drawing of the TG experiment is reported in figure 2.8.

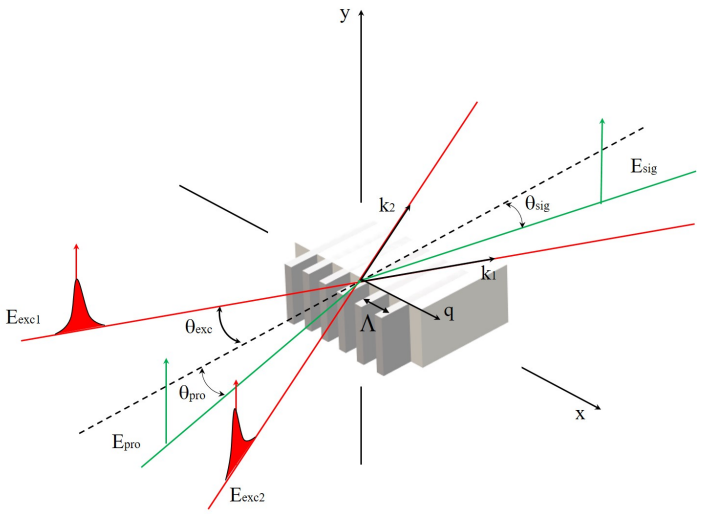

FIGURE 2.8: Schematic drawing of a transient grating experiment. Two excitation pulses, E_{exc1} and E_{exc2} induce an impulsive spatial modulation of the dielectric constant with step Λ. The relaxation of the induced transient modulation is probed by the Bragg scattering of a third beam, E_{pro}.

The spatial modulation (Λ) of the optical properties within the sample is characterized by the wave vector (q), which is given by the difference in the wave vectors ($k_1 - k_2$) of the pump pulses (see figure 2.8). The modulus of q is given by:

$$q = \frac{4\pi \sin\theta_{ex}}{\lambda_{ex}} \tag{2.18}$$

where λ_{ex} and θ_{ex} are the wavelength and the incidence angle of the exciting pulses, respectively. It is possible to have the modification of the optical properties of the material in the *real part* of the index of refraction, building up a *birefringence* and/or *phase* grating; or in the *imaginary part*, giving a *dichroic* and/or *amplitude* grating. Which is the type of grating that is built up, depends on the energy of the pump pulses. If the energy matches some absorption of the sample, then a dichroic-amplitude grating is formed, otherwise only a birefringence-phase grating is present. Several interactions between the excitation pulses and the material could take place, inducing a variation of the optical properties of the system, and thus building up the grating. One important effect is the weak *absorption*, in the

near infrared spectral region, due to the presence in the sample of harmonic/combination vibrational bands. The excess energy due to the pump absorption builds up a density grating via thermal expansion, giving rise to a pressure grating. The pressure launches two counter-propagating acoustic waves whose superposition makes a standing wave. This wave oscillates with a period defined by the material sound velocity and by the used experimental conditions (q value). Generally, this acoustic oscillations decays in time with an exponential law, whose decay time is determined by the sound damping rate. Besides acoustic waves, the temperature grating, supports a constant density grating, that relaxes by thermal diffusion, with a different exponential law, much longer than the acoustic oscillations damping time.

Another important interaction channel, able to give rise to a density grating, is represented by the *electrostrictive* effect. The interference field induces an electric dipole in every molecule, giving rise to a migration of the induced dipoles in the regions of the maximum of the electric field gradient. Contrary to the absorption effect, this grating produces the same acoustic standing wave but with a phase difference of $\pi/2$ with respect to the grating produced by the weak absorption. Through the electrostrictive effect it is only possible to produce acoustic waves.

In anisotropic materials, other possible effects could take place: the *rotation-translation coupling* effect and the *induced birefringence* directly by the electric field. The rotation-translation coupling is generated by the alignment of the molecules due to the molecular velocity grating or strain grating, which is created by thermal and electrostrictive effects. The pump induced birefringence is related to the molecular distortion and partial alignment due directly to the pump electric field. Both these effects produce a birefringence grating.

Therefore, the exciting fields produce three excitation forcing terms that drive the material modes: a *heat deposition* that drives directly the temperature, an *electrostriction* that drives the velocity and an *electric-torque* that drives the local orientational distribution of the molecules. All of these forcing terms are normally present but, depending on the radiation–material interaction nature, some of them may not be effective. The excitation modifies the dielectric constant of the material, whose relaxation is directly connected with the relaxation functions of the material modes (i.e. temperature, velocity and orientation). Which mode is really effective in defining the dielectric relaxation depends on which one of the forcing components is active and on the equations governing the mode dynamics [17].

It is possible to insert the diffraction process generated by a transient grating, in a more

general context concerning the light-matter interaction. Indeed, several approaches, with different level of complexity, can used to describe this phenomenon.
The simplest approach is the one described above, i.e. to consider the excitation and the probing as separate processes and to use a *complex refractive index* to account for dichroic-amplitude grating or a birefringence-phase grating.
The most complex approach is to consider TG experiment as an *impulsive stimulated scattering* event. In this description, the two pulses excite coherently the molecular modes, and the probe measures the relaxation of the induced coherence. The description of the experiment in this terms needs a totally quantistic approach.
Another rigorous approach is to consider the problem in the framework of *nonlinear optics*, in particular in the *Four-Wave Mixing* (FWM) context [32, 33].

2.2.2 Four-wave mixing description

Non-linear optics is the study of phenomena that occur as a consequence of the modification of the optical properties of a material system by the presence of light. Non-linear optical phenomena are "non-linear" in the sense that they occur when the response of a material system to an applied optical field depends in a non-linear manner on the strength of the optical field [34]. In the case of conventional (i.e. linear) optics, the induced polarization depends linearly on the electric field strength by the relationship:

$$\bar{P}(t) = \epsilon_0 \chi^{(1)} \bar{E}(t) \tag{2.19}$$

where the constant of proportionality $\chi^{(1)}$ is the linear susceptibility and ϵ_0 is the permittivity in the free space.
In non-linear optics, the optical response can be described by generalized equation 2.19 by expressing the polarization $\bar{P}(t)$ as a power series in the field strength $\bar{E}(t)$ as:

$$\begin{aligned} \bar{P}(t) = \epsilon_0[\chi^{(1)}\bar{E}(t) + \chi^{(2)}\bar{E}^2(t) + \chi^{(3)}\bar{E}^3(t) + ...] \\ = \bar{P}^1(t) + \bar{P}^2(t) + \bar{P}^3(t) \end{aligned} \tag{2.20}$$

the terms $\chi^{(2)}$ and $\chi^{(3)}$ are known as the second- and third-order non-linear optical susceptibilities, respectively.
The TG experiment is a time-resolved optical technique, based on the third-order non-linear

optical response (i.e. those described by a $\chi^{(3)}$ susceptibility). Therefore, it is useful to define theoretically the non-linear polarization in condensed matter using a perturbative approach. In the perturbative approach, the third-order polarization $P_i^3(r,t)$ at the point r and at the time t for homogenous media can be written as spatial and temporal convolution of the electric field with a response function:

$$\begin{aligned} P_i^{(3)}(r,t) = \int dr_1 dr_2 dr_3 \int dt_1 dt_2 dt_3 \\ R_{ijkl}^{(3)}(r-r_1, r-r_2, r-r_3, t-t_1, t-t_2, t-t_3)\cdot \\ E_j(r_1,t_1)E_k(r_2,t_2)E_l(r_3,t_3) \end{aligned} \tag{2.21}$$

E_i is the total classical electric field, which is the sum of the three incoming fields (the two pumps and the probe) and the indices *i, j, k, l* refer to the *x, y, z* component of $P^{(3)}$ and E.

The function $R_{ijkl}^{(3)}$ is the *third-order response function*, that contains the complete microscopic information about the system and hence about all its equilibrium dynamic properties.

Assuming the validity of the *Born-Oppenheimer* approximation (i.e. the incident electromagnetic energy is much lower than any electronic transition) it is possible to express the third-order polarization as the sum of an electronic and a nuclear contribution. The electronic part, for a given nuclear equilibrium position, takes account of the material's instantaneous response that arises from the non-linear distortion of the electronic clouds. This response is temperature independent at fixed density. The second term, instead, describes the polarization due to changes in the nuclear configurations induced by electronic distortions and generally is strongly temperature dependent.

Assuming that the energy of the fields is lower than any nuclear resonance it is possible to separate the excitation and probing processes. Furthermore, considering the probe beam intensity weaker than the pump one, and the excitation pulses much shorter than the relaxation time, it is possible to neglected the probe field in $E_k(r,t')$ and $E_l(r,t')$, and consider it in $E_j(r,t)$ outside the integral:

$$\begin{aligned} P_i^{(3)}(r,t) = E_j^{(pro)}(r,t) \\ \int dr' \int dt' R_{ijkl}^{(nucl)}(r-r', t-t') E_k^{(exc)}(r',t') E_l^{(exc)}(r',t') \end{aligned} \tag{2.22}$$

$E_i^{(exc)}(r^{'}, t^{'})$ is the field sum of the two pump fields and $E_j^{(pro)}(r, t)$ the probe one.
The excitation pulses produce through the third-order susceptiblity a linear dielectric constant change (ϵ_{ij}):

$$\delta\epsilon_{ij} = 4\pi \int dr^{'} \int dt^{'} R_{ijkl}^{(nucl)}(r - r^{'}, t - t^{'}) E_k^{(exc)}(r^{'}, t^{'}) E_l^{(exc)}(r^{'}, t^{'}) \tag{2.23}$$

Then the probe field interacts linearly with the medium giving a polarization $P^{(3)}$. Therefore it is possible to rewrite the equation 2.22 as:

$$P_i^{(3)}(r, t) = E_j^{(pro)}(r, t) \frac{1}{4\pi} \delta\epsilon_{ij}(r, t) \tag{2.24}$$

This polarization $P^{(3)}$ become the source of the scattered field [18].

Excitation Process

The excitation process produces a dielectric constant change, as expressed by the relation 2.23, that is convenient to express in the q-space. Indeed in a TG experiment the interesting quantity is a q-component of the spatial Fourier transform of ϵ_{ij}.

$$\delta\epsilon_{ij}(q, t) = 4\pi \int dt^{'} R_{ijkl}^{(nucl)}(q, t - t^{'}) F_{kl}(q, t^{'}) \tag{2.25}$$

where $F_{kl}(q, t^{'})$ is the spatial Fourier transform of:

$$F_{kl}(r, t^{'}) = E_k^{(exc)}(r^{'}, t^{'}) E_l^{(exc)}(r^{'}, t^{'}) \tag{2.26}$$

Considering that the spot sizes of the excitation pulses (mm) are much larger than the induced grating spacing (μm), we can approximate the excitation fields as plane waves, expressing it as:

$$\begin{aligned} E_n^{(exc)}(r, t) = \hat{e}_n E_{exc}(t) exp[i(k_n \cdot r - w_{exc} t)] + c.c.; \\ n = 1, 2, ... \end{aligned} \tag{2.27}$$

$E_{exc}(t)$ is the pulse time profile. The two excitation pulses are time coincident, and have the same frequency and intensity. Furthermore, the induced grating is instantaneous because the excitation pulses are much shorter than the oscillation period of the excited material modes. All this considerations allow to consider an ideal excitation state.

If we consider the equation 2.27 it is possible to rewrite the expression 2.26, and the excitation terms become:

$$F_{kl}(r,t) = 2E^2_{(exc)}(t)[(\hat{e}_{1k}\hat{e}_{1l} + \hat{e}_{2k}\hat{e}_{2l}) + \cos(q_0 \cdot r)U_{kl}] \tag{2.28}$$

It has been defined the tensor $U_{kl} = (\hat{e}_{1k}\hat{e}_{1l} + \hat{e}_{2k}\hat{e}_{2l})$, and $q_0 = k_1 - k_2$.
It is convenient to express the equation 2.28 in the q-space, obtaining:

$$\begin{aligned} F_{kl}(q,t) = (2\pi)^3\varepsilon^2_{(exc)}\delta(t)\{2\delta(q)(\hat{e}_{1k}\hat{e}_{1l} + \hat{e}_{2k}\hat{e}_{2l}) \\ +[\delta(q-q_0) + \delta(q+q_0)]U_{kl}\} \end{aligned} \tag{2.29}$$

The term $\varepsilon^2_{(exc)}$ is proportional to the pump field energy. The $\delta(q)$ term represents a spatially uniform excitation that does not contribute to the induced grating. While the other two terms $[\delta(q-q_0) + \delta(q+q_0)]$ contribute to build up the induced grating [18].

Scattered Field

As shown by the relation 2.24, the polarization $P^{(3)}$ becomes the source of the scattered field. In this section the relation that describes the scattered field by the induced $P^{(3)}$ will be expressed. As a first approximation we can consider that $P^{(3)}$ is entirely generated by the pumps and probe beams and that their propagation is unaffected by the scattered beam. According to this approximation, the excitation and probe beams propagate in the medium with negligible modification. Using the Green's function approach and the equation 2.24 to express $P^{(3)}$, the following result for the scattered field is obtained:

$$\begin{aligned} E_{sig}(r,t) \propto -\frac{1}{c^2}\int dt' d^3r' \frac{I}{|r-r'|}\delta(t - t' - \frac{|r-r'|}{c_m}) \\ \cdot\frac{\partial^2}{\partial t'^2}[\delta\epsilon(r',t') \cdot E_{pro}(r',t')] \end{aligned} \tag{2.30}$$

c_m is the speed of light in the medium.
Then considering the probe as CW field $E_{pro}(r,t) = E'_{pro}(r)exp[i(k_{pro} \cdot r - \omega_{pro} \cdot t)] + c.c.$, introducing the slowly varying amplitude approximation for $\delta\epsilon$, and performing the integral in dt', the scattered field equation becomes:

$$E_{sig}(r,t) \propto \frac{\omega_{pro}^2}{c^2}\int d^3r^{'}\frac{1}{|r-r^{'}|}\delta\epsilon(r^{'},t^{'}-\frac{|r-r^{'}|}{c_m})\cdot E_{pro}^{'}(r^{'}) \times exp[i(k_{pro}\cdot r^{'}-\omega_{pro}(t-\frac{|r-r^{'}|}{c_m}))]+c.c. \tag{2.31}$$

To further simplify the scattered field expression, it is reasonable to assume that the size of sample is small compared to the distance r, and to center the coordinate system at $r_0 = 0$. Taking account for these approximations, the terms of the equation 2.31 are simplified to, $|r-r^{'}| = r$ and $|r-r^{'}| = r-\hat{r}\cdot r^{'}$ in the denominator and in the argument of exponential, respectively. In addition it is possible to suppose that the frequency change between probe and diffracted beams is negligible. Therefore, the equation 2.31 becomes:

$$E_{sig}(r,t) \propto \frac{\omega_{pro}^2}{c^2 r}\int d^3r^{'}\delta\epsilon(r^{'},t_{pro})exp(i\omega_{pro}t_{pro}-iqr^{'})E_{pro}^{'}(r^{'})+c.c. \tag{2.32}$$

Considering the spot size of probe much larger than $2\pi/q$, the integral is the spatial Fourier transform of $\delta\epsilon(r,t)$

$$E_{sig}(r,t) \propto \frac{\omega_{pro}^2}{c^2 r}\delta\epsilon(q,t_{pro})\cdot E_{pro}^{'}exp[i(k_{sig}\cdot r-\omega_{pro}t)]+c.c. \tag{2.33}$$

Taking account of all the introduced approximations, the equation 2.33 shows how in a TG experiment, the scattered field has the same probe frequency ω_{pro} and an amplitude directly proportional to the dielectric tensor change $\delta\epsilon(q,t_{pro})$, and thus to the response function R through the relation 2.25 [18].

Measured Signal

The effective signal measured in a TG experiment can be introduced using some of the approximations used above to describe the pump and the probe fields. The expression of the forcing term, 2.29, that induces the variation of the material's optical properties, and that of the field scattered by the grating, 2.33, are introduced in the relation that expresses the response of the material to the perturbation induced by the pump fields, 2.25.
Obtaining the following relation for the dielectric constant:

$$\delta\epsilon(q,t) \propto R(q_0,t)[\delta(q-q_0)+\delta(q+q_0)]\cdot U \tag{2.34}$$

where R and U are the response function tensor and the tensor described in the expression 2.26, respectively.

Therefore, the scattered field becomes:

$$E_{sig}(r,t) \propto \frac{\omega_{pro}^2 \varepsilon_{exc}^2}{c^2 r}[\delta(q-q_0)+\delta(q+q_0)] \cdot U \cdot E'_{pro} \times exp[i(k_{sig} \cdot r - \omega_{pro} t)] + c.c. \quad (2.35)$$

The two q-space δ functions express the Bragg condition for a thick grating delineated in section 2.2.1 and they fix unambiguously the propagating direction of E_{sig} : $k_{sig} = \pm q_0 + k_{pro}$. Assuming that the probe beam is a CW field incident at the Bragg angle and omitting the temporal delay, we get:

$$E_{sig}(r,t) \propto \frac{\omega_{pro}^2 \varepsilon_{exc}^2 \varepsilon_{pro}^2}{c^2 r}[R(q,t) \cdot U \cdot \hat{e}_{pro}] \times exp[i(k_{sig} \cdot r - \omega_{pro} t)] + c.c. \quad (2.36)$$

where $E'_{pro} = \varepsilon_{pro} \hat{e}_{pro}$; thus the scattered field is directly proportional to a projection of the response function, R.

Using the heterodyne detection (HD), it is measured:

$$S^{HD}(q,t) = 4\langle E_{loc} \cdot E_{sig} \rangle_{op.c.} \propto \varepsilon_{exc}^2 \varepsilon_{pro} \varepsilon_{loc} (\hat{d} \cdot R(q,t) \cdot U \cdot \hat{e}_{pro}) \quad (2.37)$$

where $E_{loc} = \varepsilon_{loc} \hat{d}$ is the local field, obtained by taking a part of the probe beam. Indeed, E_{loc} is a CW field with the same frequency of the probe one and is collinear to the signal field.

$$S^{HD}(q,t) \propto \varepsilon_{exc}^2 \varepsilon_{pro} R(q,t) \quad (2.38)$$

where $R(q,t)$ is the projection of response function tensor on the pumps, probe, and detection field polarization directions. The expression 2.38 shows the relevance of the heterodyne detection, that allows to directly access the dynamics of the response function [18].

Response Function

The response function can be described thought models based on hydrodynamic description of the sample. This approach has been particularly successful for the interpretation of TG results on complex liquids. According to these models, two contributions in the response function can be identified.

$$R_{ijkl}^{(nucl)} = R_{ijkl}^{(ISBS)} + R_{ijkl}^{(ISTS)} \quad (2.39)$$

ISBS stays for impulsive stimulated Brillouin scattering and ISTS for impulsive stimulated thermal scattering. The first contribution is always present, while the second is present only if a thermalized light absorption takes place. The ISBS response describes all the signal contributions generated by the excitation laser interaction with the fully nonresonant part of the liquid dielectric constant (i.e., the electrostriction and electric-torque forcing terms). The ISTS response is that induced by laser heat deposition in the sample (i.e., by the thermalization of molecular states excited by the laser absorption).
The ISBS response can be directly connected with the correlation functions of the dielectric constant, because verifies the fluctuation–dissipation theorem.

$$R_{ijkl}^{(ISBS)}(q,t) \propto -\frac{\theta(t)}{k_B T}\frac{\partial}{\partial t}\langle \delta\epsilon_{ij}(q,t)\delta\epsilon_{kl}(-q,t)\rangle \tag{2.40}$$

$\theta(t)$ is the Heaviside step function, k_B is the Boltzmann constant, and T is the temperature. Equation 2.40 expresses and connects the nonequilibrium response function to equilibrium properties, in particular to the correlation function of the dielectric constant fluctuations ordinarily measured in a light scattering experiment.
The response functions, both of ISBS and ISTS type, can be expressed as a sum of elementary response functions, which are strictly related to the Green's functions of the hydrodynamic equations. Each elementary response functions describes a single excitation–propagation–detection process taking place in a TG experiment.

2.2.3 Optical set-up

The scheme of the lasers and the optical set-up, built up in the LENS laboratory to perform HD-TG experiments, is shown in figure 2.9.

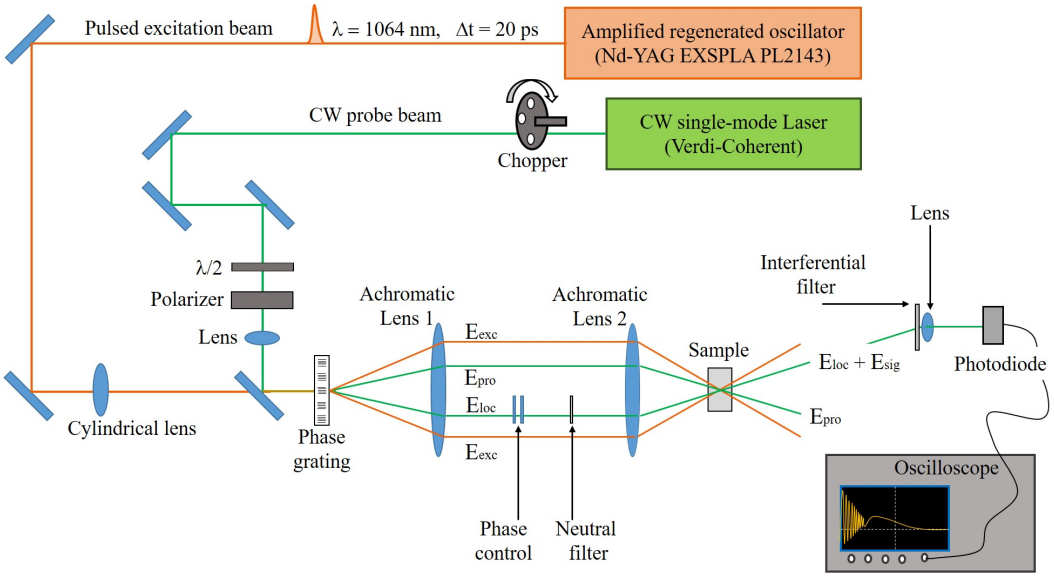

FIGURE 2.9: Laser system and optical set-up in a HD-TG experiment.

Infrared pump pulses at 1064 nm wavelength with temporal length of 20 ps are produced by an amplified regenerated oscillator (Nd-YAG EKSPLA PL2143). The probe beam, at 532 nm wavelength, is produced by a Nd-YVO (Verdi-Coherent), that is a CW single-mode laser. To avoid any undesirable thermal effects on the sample and to not burn the photodiode, the Nd-YVO (Verdi-Coherent) laser energy has been reduced. To do that the CW beam is limited in a time window of about 1 ms every 10 ms, by using a mechanical chopper that is synchronized with the excitation pulses (see figure 2.9).

To properly measure the natural damping of the induced acoustic oscillations, as shown in figure 2.10, the pump beam is focused with a cylindrical shape to have on the sample an excitation grating extended in the q-direction (about 5 mm), while the probe beam is focused to a circular spot in order to have a probe area with smaller dimensions in q-direction (about 0.5 mm). Without this geometry of the beams, an acoustic damping due to geometrical reasons could be probed, affecting the detection of the natural damping time of the sample [35, 36]. This latter is properly extracted if it is shorter, compared to the geometrical damping time. Since in our samples the natural damping time is quite long (tens and hundreds of ns), a very precise alignment of the pump and the probe beams is required in order to measure the natural damping. Therefore, the alignment is done through a camera, which permits a micrometric control of the centering and of the spatial superposition of the beams.

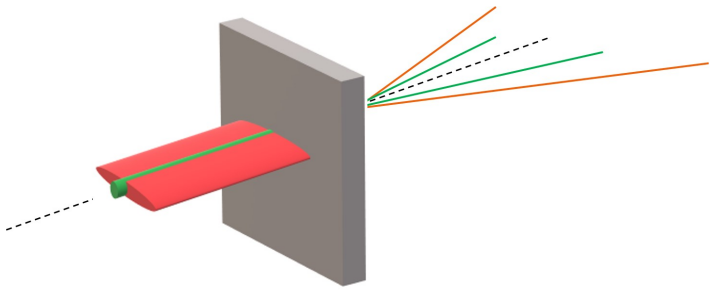

FIGURE 2.10: Picture of the spatial superposition of the pump beam (red beam with cylindrical focus) and the probe beam (green beam with circular focus).

Then, the two beams are collinearly coupled by the dichroic mirror and are sent on the grating phase. By choosing different spacing of grooves of the grating phase, it is possible to easily change the angle between the exciting beams and consequently the q-vector induced in the sample. For the latter reason, we use a phase mask composed of six phase gratings characterized by different spacing, able to produce on the sample the following q-vector values: 0.63, 1.00, 1.39, 1.79, 2.09 and 2.51 μm^{-1} (if the achromatic doublet lenses have the same focal length) [37, 38].

The grating diffracts the beams, and the zero order is stopped, while the first order beams are used to produces the two excitation pulses (E_{exc}), the probe beam (E_{pro}), and the local field (E_{loc}). These beams pass through a doublet of achromatic lenses both with focal length 160 mm. The second lens of the achromatic doublet recombines and focuses the beams on the sample, in order to reproduce the same spatial modulation of the phase mask. The reference beam (E_{loc}) is attenuated by a neutral density filter, and adjusted in phase by passing through a pair of quartz prisms, to produce a heterodyne detection. The HD-TG signal is optically filtered and measured by a fast avalanche silicon photodiode with a bandwidth of 1 GHz (APD, Hamamatsu). The signal is then amplified by a DC-800 MHz AVTECH amplifier and recorded by a digital oscilloscope with a 7 GHz bandwidth (Tektronix). The temporal resolution of the experiment does not depend on the pump pulse width, but only on the bandwidth of the detection system.

2.2.4 Data collection and fitting procedure

The data are recorded using the heterodyne detection, characterized by the superimposition of the signal and the reference fields to the detector, which records their interference. The scattered field can be written as:

$$E_{sig}(t) = \hat{e}\varepsilon_{sig}(t)exp[i(k_{sig} \cdot r - \omega t)] + c.c. \tag{2.41}$$

since $\varepsilon_{sig}(t)$ is a complex function, it has been chosen a reference field with the same wave-vector, direction and frequency of $E_{sig}(t)$ and with a constant amplitude $E_{loc}(t) = \hat{e}\varepsilon_{loc}exp[i(k_{sig} \cdot r - \omega t + \varphi)] + c.c.$, ($\varphi$ is the optical phase between the signal and the reference field). As a consequence, ε_{loc} is a real amplitude and the heterodyne signal is:

$$\begin{aligned} S(t) &= \langle |E_{sig} + E_{loc}|^2 \rangle_{op.c.} \\ &= I_{sig}(t) + I_{loc} + 2\{Re[\varepsilon_{sig}(t)]\varepsilon_{loc}cos(\varphi) + Im[\varepsilon_{sig}(t)]\varepsilon_{loc}sin(\varphi)\} \end{aligned} \tag{2.42}$$

the first two terms of the equation 2.42 are the homodyne contribution and the local field intensities respectively. The third term represents the heterodyne contribution. High local field intensities make the homodyne contribution negligible and the temporal variation of the signal is dominated by the heterodyne contribution. This latter is directly proportional to the signal field, and not to its intensity as for the homodyne contribution. The heterodyne term (between curly braces) can be experimentally isolated by subtracting two signals characterized by different phases. In addition, the heterodyne detection enables the cancelling of eventual spurious contributions present in the signal. We recorded two HD-TG signals with different phases of the local field, the first signal S_+ with $\varphi_+ = \varphi_0$ and a second one S_- with $\varphi_+ = \varphi_0 + \pi$, we then subtracted S_- from S_+. This procedure extracted the pure HD signal from the not phase sensitive contributions, including the homodyne and local field ones:

$$\begin{aligned} S^{HD}(t) &= [S_+ - S_-] \\ &= 4\{Re[\varepsilon_{sig}(t)]\varepsilon_{loc}cos(\varphi_0) + Im[\varepsilon_{sig}(t)]\varepsilon_{loc}sin(\varphi_0)\} \end{aligned} \tag{2.43}$$

In a TG experiment, the dynamic birefringence-phase and dichroic-amplitude gratings are linked to $Re[\varepsilon_{sig}(t)]$ and $Im[\varepsilon_{sig}(t)]$, respectively. It is evident that choosing $\varphi_0 = 0$ or

$\varphi_0 = \pi/2$, and substituting the values in the relation 2.43 it is possible to extract only the real or the imaginary part of $[\varepsilon_{sig}(t)]$, selectively measuring the dichroic-amplitude or the birefringence-phase contribution.

When the dichroic-amplitude grating is negligible, $[\varepsilon_{sig}(t)]$ is real and the heterodyne term is $\varepsilon_{sig}(t)\varepsilon_{loc}cos(\varphi)$, then choosing $\varphi_+ = 2n\pi$ and $\varphi_- = (2n+1)\pi$, with n integer, we obtain:

$$S^{HD}(t) = [S_+ - S_-] = 4\varepsilon_{sig}(t)\varepsilon_{loc} \tag{2.44}$$

In a HD-TG experiment the pump fields interacted with the material, inducing into the sample a density grating; this is build up by both a weak absorption of the laser pulses and the electrostriction effects. The absorption was due to the presence in the sample of harmonic/combination vibrational bands having frequencies resonant with the laser wavelength, 1064 nm. The electrostriction was due to the migration of the induced dipole in the regions of the maximum of the electric field gradient. These mentioned effects produced two standing acoustic waves characterized by a phase difference of $\pi/2$. Both the standing waves decayed in time with the exponential law, $e^{-\Gamma_A t}$. The laser absorption phenomena induced in the sample a third interaction effect, the thermal grating. This is static grating that decays through the heat diffusion processes; represented by the exponential law, $e^{-\Gamma_H t}$. The thermal diffusion time constant, $\tau_H = \frac{1}{\Gamma_H}$, was typically much longer than the damping time of the acoustic oscillation, $\tau_A = \frac{1}{\Gamma_A}$.

The generalized hydrodynamic equations are used to express the transient grating signal, taking account of the complex aspects of the relaxation dynamics of the soft materials, such as the viscoelasticity. In the present thesis the hydrodynamic models and all the mathematical steps leading to the S^{HD} are not reported, but only the expression that has been utilized to perform the fitting of the measured HD-TG signal is indicated [18].

$$S^{HD} = Ae^{-\Gamma_A t}\cos(\omega_A t) + Be^{-\Gamma_A t}\sin(\omega_A t) + Ce^{-\Gamma_H t} \tag{2.45}$$

The fitting parameters are: the acoustic angular frequency, ω_A, the acoustic damping rate, Γ_A, the thermal decay rate, Γ_H, and the corresponding amplitude constants, A, B and C. In this thesis, the attention is focused on the speed of sound, $C_S = \omega_A/q$, and the acoustic damping rate, Γ_A. The relative uncertainties associated with these values are those related to the fitting procedure, which are $\Delta\omega_A/\omega_A \leq 0.1\%$ and $\Delta\Gamma_A/\Gamma_A \leq 1\%$, respectively.

The measured signal expands over a very wide time range, therefore, in order to have a good

sampling of all the dynamic processes, it is necessary to acquire two time scales. We record the data using a fast time window (0-80 ns range with a 50 ps time step of sampling) and a long one (0-2 μs range with 800 ps time step). The measurements are merged in a single data file. Each track is the average of 1000 records, this procedure produces an excellent signal to noise ratio.

Chapter 3

Glutathione hydration in pure water and in water/salts mixtures

Environmental conditions such as pressure, temperature and all properties related to the solvent such as pH and ionic strength play a fundamental role in the correct structuring and functioning of biomolecules. Water is the most common solvent in living systems, and water molecules surround and interact with biomolecules, exerting a strong influence on their structure, flexibility, and functionality. Biological molecules like nucleic acids, proteins and peptides play their role in aqueous environment and often in presence of high salt concentrations. Understanding the function that salts perform in affecting the biomolecules behavior is not a scientific trivial problem and is crucial to the correct comprehension of their mechanism of action. Indeed ions have a key task in a huge number of biochemical processes, and can interact directly with the surface of the biomolecule or can modify its solvation shell by acting on the water hydrogen-bonding network [39]. The parameters that influence the interactions between ions and biomolecules are manifold i.e. the ions steric encumbrance, the charge density, the possibility to establish hydrogen bonds and the tendency to exist in solution as ionic pair. The effect of salts on biomolecules has been studied for the first time by Hofmeister and summarized in the so-called "Hofmeister series", that reflects the capacity of ions to stabilize or destabilize the proteins native structure by influencing the surrounding water network [40, 41, 42]. Based on this ability it is possible to divide ions into kosmotropic and chaotropic. The first have high charge density, therefore ion-water interactions are stronger compared to water-water ones. This phenomenon increases the water structure, shifting the equilibrium to low-density water. Instead, the chaotropic ions have the opposite effect [43]. The understanding of ions effect on proteins and peptides stability [44] based on the Hofmaister series is not always correct because ions can interact with the

molecule surrounding water or can directly penetrate into the water layer and interact with the peptide surface [45]. Moreover the Hofmeister ions effect become important when the electrostatic forces are screened by high salt concentrations, while at low salt concentration, ions affect peptides mainly via electrostatic interactions [39]. Recently the scientific world has gained great interest in a new category of salts namely ionic liquids (ILs). They are a wide class of molecules able to stay as molten salts at room temperature [46]. In order to deeply understand and fining tune the solvation environment of biomolecules, it is possible to use ILs as co-solvents or as pure solvents. ILs are formed by an organic cation linked with an anion. By tuning the typology of ILs i.e. changing the cation and the anion, or regulating the molar fraction between ILs and water, it is possible to control and improve different properties of the systems like reaction reactivity, aging and thermal stability of biomolecules in solution [47]. The structure of the solvation network created by ILs could be complex due to the complexity of ILs molecules and the possibility to participate with different types of interactions. The ability of ILs to solvate biomolecules mainly arises from the directional short-range hydrogen bond interactions and the unidirectional long-range electrostatic forces [48].

In this chapter, the solvation and the thermal behavior of the reduced glutathione (GSH) in pure water [49], in a binary mixtures of water/inorganic salts and water/ionic liquids have systematically been studied. It has been decided GSH as a case study for its relevance in living systems. Indeed, GSH is a tripeptide present as a sub-major constituent in the intracellular space of plants, animals and microorganisms, composed by three amino acid residues, i.e. glutamic acid (Glu), cysteine (Cys) and glycine (Gly). It is the smallest thiol existing in mammalian cells, with a concentration higher than mM [50]. As shown in figure 3.1, depending on the concentration of H_3O^+ ions in solution, glutathione coexists with different percentages of its forms, namely $GSH_{-\alpha 1}$ and $GSH_{-\alpha 12}$ that differ for a protonated ($GSH_{-\alpha 1}$) and deprotonated ($GSH_{-\alpha 12}$) glycine residue, respectively. In particular, in acid condition (pH= 3) the tripeptide is present as $GSH_{-\alpha 1}$ (about 60%) and $GSH_{-\alpha 12}$ (about 30%) [51].

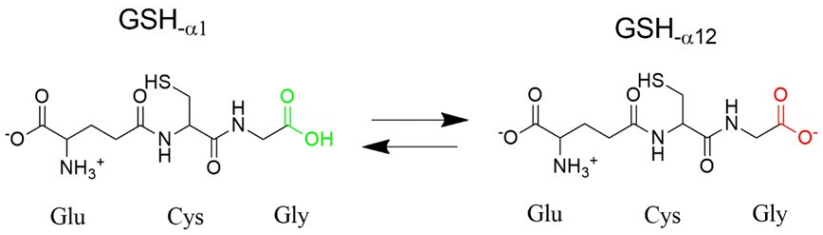

FIGURE 3.1: Structure of glutathione in its protonated ($GSH_{-\alpha 1}$) and deprotonated ($GSH_{-\alpha 12}$) forms; this two forms are in equilibrium with each other. In acid condition (pH= 3) the tripeptide is present as $GSH_{-\alpha 1}$ (about 60%) and $GSH_{-\alpha 12}$ (about 30%).

The major role of glutathione is in the enzymatic reduction of hydrogen peroxide and other peroxides, and in general in the protection of cell components against oxidation for maintaining a reducing cellular environment. Indeed, the thiol group of GSH is a powerful reducing agent that has, as a target, the Reactive Oxygen Species (ROS). The tripeptide exists in the organisms in its reduced (GSH) and oxidized (GSSG) states, and maintaining an appropriate ratio between these two forms is fundamental to prevent cellular oxidative stress. If there is a deficiency of GSH in the cell environment, there is the risk of membrane oxidation, which is related with the onset of a great amount of pathologies [52, 53, 54].
The different hydration condition in terms of temperature, pH, GSH concentration and different ions has been investigated, with the aim of correlating some of the Raman spectral features to specific peptide structures and to the description of interaction of water molecules on the peptide bond. In addition, short peptides as GSH, even though lacking many features of the longer amino acid chains, can be considered as a model systems for examining peptide-water interactions that are crucial to biological activity and for water accessibility. The investigation of peptides behaviour in aqueous environment is key to understand how proteins are able to perform and maintain at different conditions their functions within the human body [55]. Thus, a description, at the atomic scale, of peptide hydration in different environmental conditions can provide insights on still open and important issues, like protein folding and association as well as protein-ligand binding processes [56].
The vibrational spectroscopic techniques, such as infrared absorption and Raman scattering, are extremely sensitive to the intra- and inter-molecular interactions, and therefore they are very useful for providing insights on possible correlations existing between conformational changes in peptides and proteins and the molecular properties of the hydration water. In order to study GSH in aqueous environment, Raman scattering is certainly one of the most

suitable techniques. Compared to infrared absorption, Raman spectroscopy have the advantage to be particular sensitive to the amide signals even in diluted conditions (i.e. few mg of peptide for ml of solution), because of the weak interference of the small Raman cross section of the OH bending mode of water. Moreover, both selectivity and sensitivity of the technique can be dramatically improved, by resonance effect, by exploiting UVRR spectroscopy that greatly enhances specific vibrational signals of targeted molecular groups, through an appropriate tuning of the excitation wavelength [57, 58, 59].

Thanks to the analysis of UVRR spectra of water-GSH solutions in a wide wavenumber range between 1000 and 4000 cm^{-1}, it is possible to simultaneously follow, as a function of the investigated parameters, the changes of the signals arising from peptide backbone (Amide vibrations, 1200-1800 cm^{-1}) [60, 61], and from water molecules (OH stretching bands, 2800-3800 cm^{-1}). The bands that fall in these vibrational ranges can be used as sensitive spectroscopic markers of the GSH structure and of the hydrogen-bonding environment of backbone and side-chain groups of the tripeptide [49]. The experimental results are compared with theoretical ones in order to obtain a detailed view of the solvation environment around GSH molecules which is responsible for its conformational changes. Among the various computational techniques, molecular dynamics (MD) simulation is the most powerful tool to understand the details of solvation processes at molecular level. For performing the MD simulations and quantifying the interaction of GSH with the ionic liquids and the inorganic salts in the aqueous solutions the General Amber Force Field (GAFF) [62] is used. It is worthy to mention that the general accuracy of GAFF in the case of ILs solvents has been tested and GAFF is widely used in ILs simulations [63, 64, 65]. For analyzing MD simulations, a radial distribution function (RDF), g(r), is used to describe the distribution of solvent molecules around specific molecule or atom.

3.1 Experimental methods

3.1.1 Samples preparation

Glutathione GSH (C10H17N3O6S, γ-L-Glutamyl-L-cysteinyl-glycine) is purchased from Sigma Aldrich ($\geq$ 98.0 %) and used without further purification. Aqueous solutions of GSH are prepared by dissolving GSH in doubly distilled deionized water at different concentration, ranging from 160 to 20 mg/ml. The pH of these solutions is measured by using a standard pH meter. By dissolving the tripeptide in water without the addition of other substances, the pH of the solution reaches the value of 3.0. Instead, small amounts of KOH were added to the solution of GSH to regulate the pH to 8.0 up to a final concentration of KOH corresponding to 1 μM (three order of magnitude less than the concentration of peptide). Deuterated GSH solution at concentration of 20 mg/ml is prepared by dissolving the tripeptide in deuterium oxide (99.9 atom % D, Sigma Aldrich).
GSH-water/salts solutions has been prepared dissolving 20 mg/mL of the tripeptide in doubly distilled deionize water, reaching a concentration of 0.07 M and pH 3.0. The used salts are dissolved in different quantity based on the respective molecular weight, in order to have an equimolar condition with GSH molecules. All solutions are freshly prepared and placed into a 1 cm path quartz for UV Raman measurements.

3.1.2 UVRR spectra

UV resonance Raman (UVRR) experiments using synchrotron radiation (SR) are carried out at the BL10.2-IUVS beamline of Elettra Sincrotrone Trieste (Italy) [27], described in detail in chapter 2 in the subsection 2.1.4.
The exciting wavelength of Raman spectra has been selected in the range between 210 and 270 nm by varying the range of the undulator gap between 25 and 19 mm. A Czerny-Turner monochromator (Acton SP2750, Princeton Instruments) is used to monochromatize the incoming SR. The UVRR spectra are collected in a back-scattered geometry by using a triple stage spectrometer (Trivista, Princeton Instruments). The spectral resolution is set to about 15 cm^{-1} for SR experiments in order to have a sufficiently high signal to noise ratio. The calibration of the spectrometer is standardized using cyclohexane (spectroscopic grade, Sigma Aldrich), which does not absorb UV within the wavelength range of interest. The UVRR spectra of solutions collected in the OH stretching region (2000-4000 cm^{-1}) are excited with the wavelength of 266 nm provided by a Q-switched DPSS laser. In this configuration,

the experimental resolution is set to about 5 cm^{-1}. During all the experiments, the measured power radiation on the solutions is kept sufficiently low (a few μW) to avoid possible photo-damage effects or heating of the sample. The Raman spectra of solutions are acquired at different values of temperature ranging from 5 to 50 °C. Visible Raman spectra recorded on dry powders and aqueous solutions of GSH are collected at room temperature, by means of a micro-Raman setup (Horiba-JobinYvon, LabRam Aramis) with a spectral resolution of about 1 cm^{-1}. The exciting radiation at 632.8 nm is provided by a He-Ne laser.

3.1.3 MD simulations

The MD simulations are carried out by the group of Prof. Babak Minofar at the *Institute of Nanobiology and Structural Biology* in the Czech Republic.

For performing the MD simulations the General Amber Force Field has been used. The starting structure for the salts has assembled in a simulation box containing an equivalent amount of cation and anion. A total amount of 100 molecules cation and 100 molecules anion are added randomly to reach the desired ILs concentration, in a cubic box with dimension 6.0 × 6.0 ×6.0 nm^3 where the box later solvated by water molecules. For random distribution of GSH in the simulation boxes Packmol package is applied [66, 67]. Even ions and water molecules are randomly added to the simulations boxes, some unfavorable interactions may occur in the systems therefore, minimization is required. For minimization of the systems, steepest descent minimization procedure is used to remove all unfavorable interactions. After minimization, all systems are equilibrated by performing 500 ps NVT (Canonical ensemble) restrained simulations followed by 500 ps NPT (isothermal–isobaric ensemble). Equilibration proceed with the production runs where the linear constraint solver (LINCS) algorithm [68] is employed for all bonds involving hydrogen atoms and short range non-bonded interactions are cut off by 1.2 nm. Long-range electrostatic interactions are treated by the particle mesh Ewald method [69] procedure. For production of initial velocities Maxwell–Boltzmann distribution is used for all simulations at 27, 47 and 67°C. V-rescale coupling algorithm is used [70] with the coupling constant of 0.1 ps to ensure constant temperature and pressure during the simulations. MD production runs are performed in NPT ensemble for 100 ns at 27, 47 and 67°C where 2 fs time step is used. Data for further analysis is stored in every 5 ps for all simulation. Gromacs 4.6.5 program package is used for performing MD simulations [71, 72, 73] whereas Visual Molecular Dynamics

(VMD) is used for visualizations and preparation of snapshots [74]. For analyzing MD simulations, a radial distribution function (RDF), g(r), is used to describe the distribution of solvent molecules around specific molecule or atom. RDF can be calculated according to equation:

$$g(r) = \frac{1}{\rho N} \langle \sum_i \sum_j \delta[r - r_{ij}] \rangle \tag{3.1}$$

N is the total number of atoms, $\rho = N/V$ is the number density, r_{ij} is the distance between atoms i and j, and the brackets indicate the ensemble average.

3.2 Results and discussion

3.2.1 Influence of GSH on the water H-bond network

In aqueous solution, the hydrophilic sites of peptides interact with water molecules, which change their locations and orientations in the hydration shell around the solutes. As a result, depending on the entity of this destructuring effect due to the solute, changes in the OH stretching band shape of water are observed. These changes, have been related to modifications of the water hydrogen bond network [75, 76]. Figure 3.2 shows the Raman OH stretching band collected on GSH solutions at two concentrations (20 and 160 mg/ml) and at two pH values, 3 and 8. Since it is known that the presence of ions affects the hydrogen bond network of water [77, 78], the spectra of GSH are compared in figure 3.2(a) and (b) with those of pure solvent at the same values of pH, 3 and 8 respectively. In this way, the different effect of the two forms $GSH_{-\alpha 1}$ and $GSH_{-\alpha 12}$ on the H-bond network of water can be more reliably evidenced.

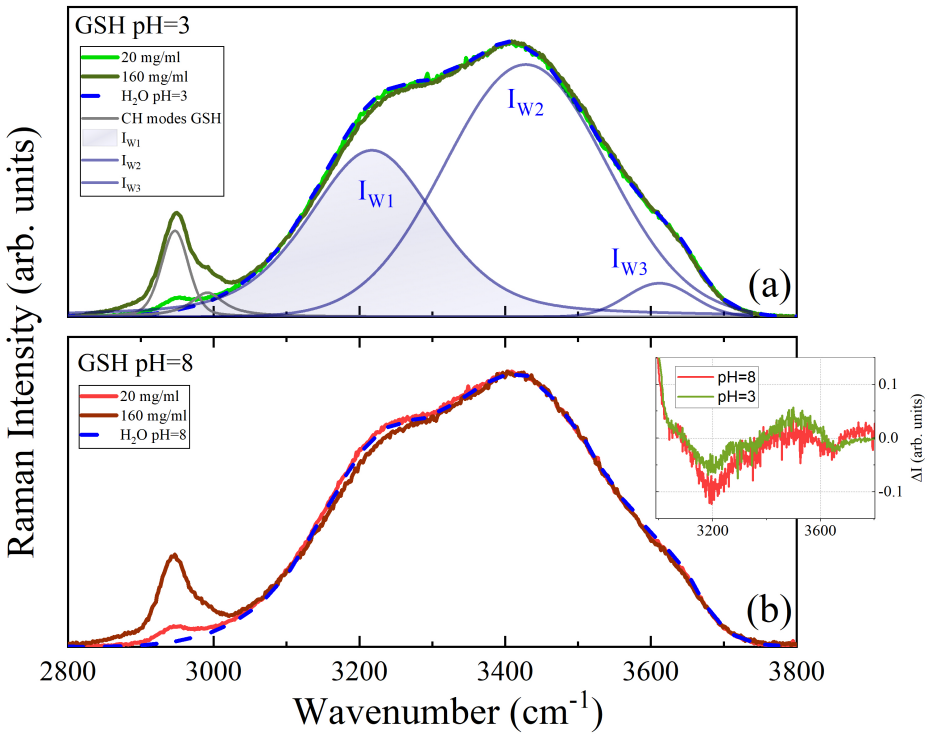

FIGURE 3.2: UV Raman spectra (λ_{exc}= 266 nm) collected at room temperature for diluted and concentrated solutions of GSH at pH= 3 (panel a) and pH=8 (panel b). The Raman profile of acid (pH= 3) and basic (pH= 8) water is shown in the same graph for comparison. The spectra are normalized to their maximum intensity. The results of the fitting procedure carried out for the spectra of GSH/water at pH= 3 and concentration of 160 mg/ml are reported in panel (a). Inset: difference spectra $\Delta I = I(GSH) - I(water)$ calculated for both pH conditions.

Figure 3.2 points out that the OH stretching signal results in a Raman broad band, due to the sum of several components. The component at 3200 cm^{-1} has been attributed to the contribution of the more ordered water structures [79, 80] and it decreases as a function of GSH concentration (figure 3.2(a) and (b)). The same trend is found for both GSH solutions at pH= 3 and pH= 8. However, it is visible that the effect of GSH at basic conditions on the ordered water H-bond environments is greater compared with that of the tripeptide in acid solution, as evidenced by the difference spectra reported in the inset of figure 2. This finding can be rationalized by considering that at pH= 8 glutamic acid is in its zwitterionic form and cysteine remains with the same protonation state that has at pH= 3, while is significantly greater the number of COO^- groups, due to the glycine deprotonation at basic condition, that can perturb the H-bond of surrounding water.

To quantify the spectral changes described above, a curve-fitting procedure has been employed [81, 82, 83] to reproduce the whole OH profile by considering three distinct components: a mixed Gaussian-Lorentzian function for the contribution arising from the more ordered water structure ($\omega_1 \simeq 3200$ cm^{-1}), and two Gaussian profiles for the contributions assigned to the "closed" water structure where H-bonds are partially distorted and to the OH groups weakly stabilized by H-bonds interactions ($\omega_2 \simeq 3450$ cm^{-1} and $\omega_3 \simeq 3600$ cm^{-1}, respectively). It is noteworthy that all these species have to be considered as formed transiently during the H-bond reorganization of the water network [84]. In order to isolate the ordered water component from the Raman spectra of GSH solutions a simplified approach, with respect to the many other decomposition methods introduced for the analysis of OH stretching band of water, it has been chosen. As recently shown in the case of sugar-water solutions [85], the data handling used in this thesis represents a simple and convenient tool for a comparative evaluation of the different extent of tetrahedral order in aqueous systems. Figure 3.2(a) displays an example of the fitting results obtained for the GSH solution at pH= 3 and concentration of 160 mg/ml. The relative amount of OH groups involved in the more ordered water structure can be estimated by the quantity C(c), defined as the relative area of the ω_1 component, $I_{\omega_1}(C)$, with respect of the whole OH band, $I_{tot}(c) = I_{\omega_1}(c) + I_{\omega_2}(c) + I_{\omega_3}(c)$:

$$C(C) = \frac{I_{\omega_1}(C)}{I_{tot}(C)} \tag{3.2}$$

Figure 3.3 shows the concentration dependence of C(c) at room temperature, obtained

for GSH in protonated and deprotonated form, compared with that of corresponding acid and basic water. The value of C(c) decreases with increasing GSH concentration, both at pH 3 and 8, suggesting that the interactions with the chemical groups of peptide affect the tetrahedral ordering of a large fraction of water in the hydration shell of the tripeptide.

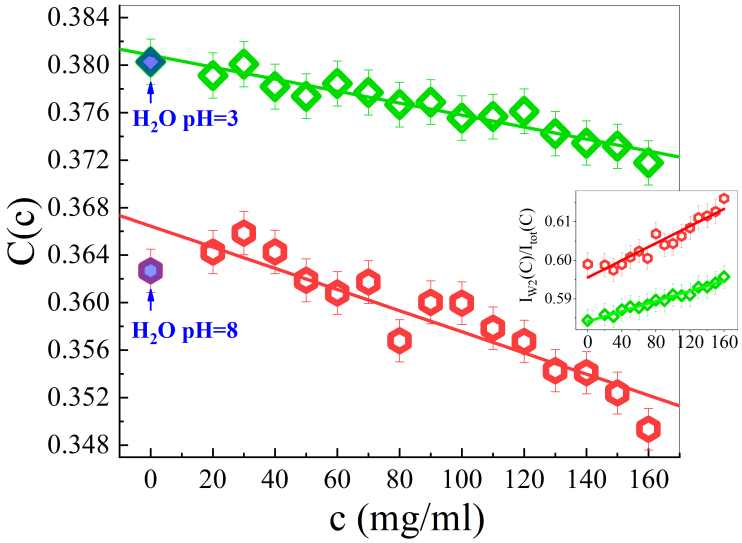

FIGURE 3.3: Concentration dependence of the quantity C(c) calculated by equation 3.2, for GSH aqueous solutions at pH= 3 and pH= 8. Dashed lines are linear fit of the experimental data. The values of C ($c = 0$) obtained for acid and basic water solutions are reported for comparison. The inset shows the concentration-dependence of the relative area of the component $I_{\omega_2}(c)$ for GSH at pH= 3 and pH= 8.

As discussed above, the linear decrease of C(c) with concentration of GSH reflects a progressive disruption of the ordered H-bond structures of water induced by the increasing number of peptide molecules, at both acid and basic conditions. In the case of the sample at pH=8, larger statistical fluctuations are visible in figure 3 due to the worst signal to noise ratio shown by the Raman spectra of GSH basic solutions with respect to acid ones. Nevertheless, it is clearly recognizable, within the experimental error a linear trend of the quantity C(c) as a function of peptide concentration, for both pH= 3 and 8. Interestingly, a more marked effect on the H-bonds of water is brought by GSH in its deprotonated form with respect to the protonated one, at the same concentration. This finding is also confirmed by the trend found for the relative area of $I_{\omega_2}(c)$ component as a function of concentration (see figure 3.3 inset). In a recent work [56] based on the combination of neutron diffraction experiments and computer simulations, a structural study of the hydration of GSH was carried out. The authors found a noticeable difference between the number of water

molecules in the first hydration shell around the different carboxylate groups, with less than five water molecules hydrating the COO^- site of the glutamic acid, and more than seven water molecules hydrating the COO^- on the glycine with a sensibly different spatial distribution. Instead, in acid environment, glycine is also present in its protonated form and the carboxylic group has a relatively smaller coordination number so leading to less than four water molecules hydrating this specific peptide site [56]. Therefore, it is reasonable to state that water molecules are less tightly bound to the COOH group in comparison with the carboxylate group. These structural data are in agreement with the present outcomes on the effect induced by the two different species of GSH on the water H-bond network [49].

3.2.2 Dependence of Amide bands on pH and concentration

The analysis of UVRR spectra of glutathione solutions in the 1000-2000 cm^{-1} frequency range gains insights on the intermolecular interactions that can exist between the tripeptide backbone and the water molecules. It is well known, that the UVRR spectra of proteins and peptides contain more specific information in comparison to IR and conventional visible Raman spectra [24, 86, 87, 26, 88, 89, 90]. This is due to the enhancement of the Raman cross section of the amide modes, obtained by irradiating the sample with the ultraviolet radiation [26, 91, 92, 93]. This makes UVRR technique particularly informative by considering the unique response exhibited by amide bands to the backbone conformational changes of peptides and to the hydrogen-bonding environment [87, 94, 95]. In order to monitor the selectivity of UVRR to the Amide vibrations, the excitation wavelength dependence of the Raman spectra of GSH aqueous solution, has been investigated. Figure 3.4(a) shows UVRR spectra collected at different exciting wavelengths ranging from 266 to 210 nm compared with a spectra registered with an excitation wavelength of 633 nm.

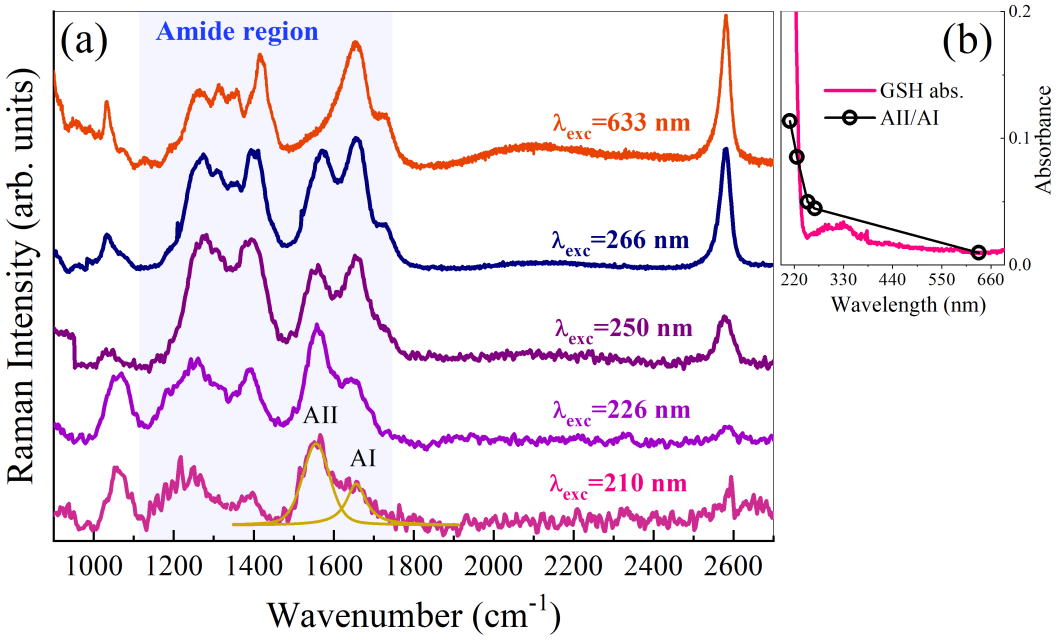

FIGURE 3.4: (a) Raman spectra of GSH aqueous solution (100 mg/ml, pH= 3) excited at 633, 266, 250, 226 and 210 nm of excitation wavelength. An example of the spectral decomposition of the spectral profiles into AI and AII bands is also reported (yellow lines). (b) UV-VIS absorption spectra of GSH aqueous solution (purple line) and intensity ratio, observed in UVRR spectra, between the AII and AI bands at the corresponding excitation wavelengths (empty circles).

The comparison between the different UVRR spectra in figure 3.4 evidences the progressive increasing, at low excitation wavelengths, of the Raman cross section for all the Amide signals, falling in the wavenumber range 1100-1800 cm^{-1}, with respect to that of SH stretching (2600 cm^{-1}). This trend is expected on the basis of the pre-resonance condition of the UV excitation with the amide $\pi \rightarrow \pi^*$ transition occurring at 190 nm and it is in agreement with what observed also for other simple peptides [92, 93]. More interestingly, figure 3.4(a) shows that the signal associated to the Amide II mode (1560 cm^{-1}, AII), completely absent in the spontaneous Raman spectrum excited at 633 nm, becomes dominant with respect to the band of Amide I (1660 cm^{-1}, AI) in the UVRR spectra of GSH excited at the lowest wavelengths, i.e. 210 and 226 nm. This specific selectivity on the AII mode has to be ascribed to the nature of the electronic transition of amide groups of GSH [92, 93], as evident from the inspection of figure 4(b). Here the intensity of the ratio between the area of AII and AI modes is superimposed to the absorption spectrum of GSH recorded in aqueous solution. As expected, the strong upturn of the absorbance spectrum of GSH observed at

low wavelengths is followed by a rapid increment of the ratio between the Raman intensities of AII and AI band detected in the corresponding UVRR spectra. By looking at the UVRR spectra of GSH excited at 266 and 250 nm, it appears that both the Amide bands and the SH stretching mode (2580 cm^{-1}) arise in the spectra with a relative comparable intensity (fig.3.4(a)). In particular, the excitation at 266 nm, although quite far from the Amide resonance condition, offers the opportunity to operate in the best experimental conditions needed to simultaneously probing different chromophores, i.e. the signals of GSH arising from the peptide backbone and from the side-chain groups (COOH and SH modes). Figure 3.5(a) and (b) shows respectively the spectra of dry GSH powders and those of GSH aqueous solution, at the two investigated pH values, 3 and 8.

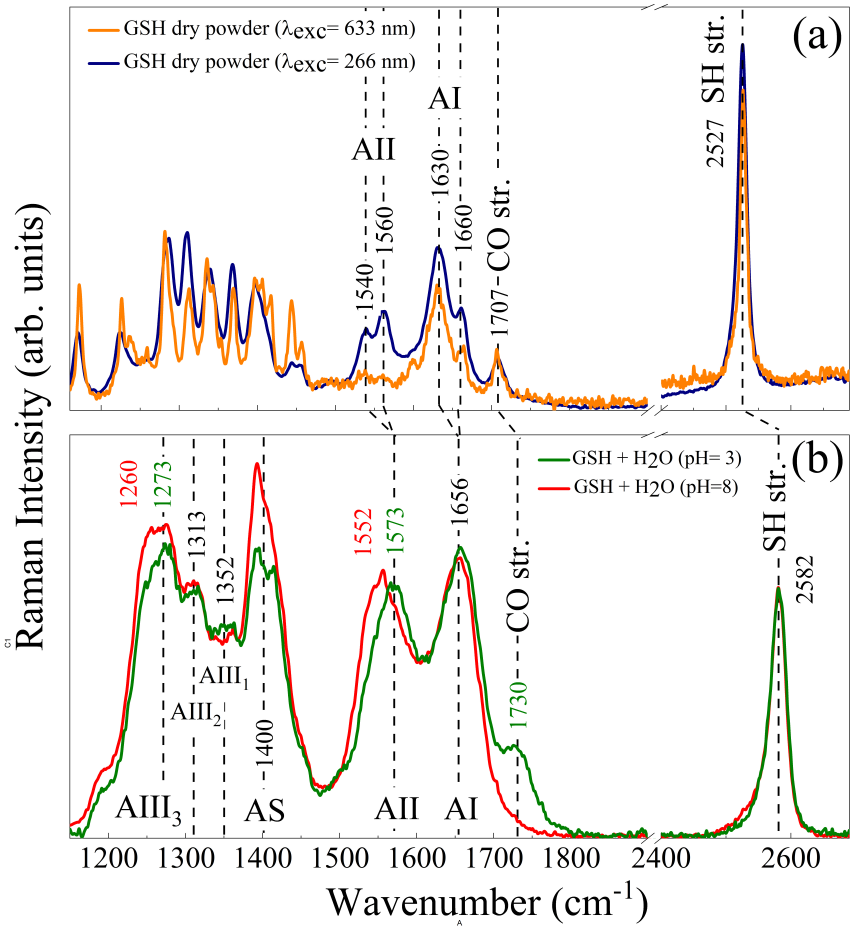

FIGURE 3.5: (a) Non-resonance and UV resonance Raman spectra of dry GSH powders; (b) UVRR spectra (λ_{exc} = 266 nm) of GSH aqueous solutions (100 mg/ml) at pH= 3 and pH= 8 at 20 °C; the spectra have been arbitrarily normalized on the intensity of the SH stretching mode.

The main components that dominate the spectrum of the dry GSH powder are also visible in that of the peptide water solution, although in the latter profile the bands are broader and fall at slightly different frequencies. The frequencies blue shift of the Amide and SH

bands, that occur passing from the dry sample to the hydrated one, is related to the involvement of the Amide and SH sites in stronger hydrogen bonds in the dry sample compared to the hydrated one, due to the higher packing of the tripeptide in the dry form. In the 1100-1800 cm^{-1} spectral region, we recognize the AI band that is mostly due to C$=$O stretching vibration and the AII that results by the out-of-phase combination of N$-$H in-plane bending and C$-$N stretching [91, 96]. Both AI and AII appear as two distinct sub-components, spaced by 20-30 cm^{-1} in the spectra of GSH dry powder. The AI and AII signal splitting denotes that in the crystalline form the two peptide bonds present in the structure of glutathione are differently involved in inter-molecular H-bonds [97, 98]. The different entity of the splitting observed for AI band ($\Delta\nu_{AI}$= 30 cm^{-1}) with respect to that of the AII ($\Delta\nu_{AII}$= 20 cm^{-1}) is ascribed to the different normal mode composition of these two amide bands that leads to give a major sensitivity to the H-bond on the C$=$O site for AI signal, whereas the AII band is mainly affected by the interactions involving the N$-$H site [99].

Amide III (AIII) is a very complex band arising from the in-phase combination of N$-$H bending and C$-$N stretching. In figure 3.5(b) the component at 1260 cm^{-1} labeled as $AIII_3$ arises from the mechanical coupling between the N$-$H and $C_\alpha - H$ in plane bending, therefore it exhibits a great sensitivity to the Ψ dihedral angle in peptide and proteins and to the number and types of amide hydrogen bonds [60, 87, 94, 95, 96, 100]. The UVRR spectra of GSH solutions at both pH conditions exhibit a strongly resonance-enhanced band at 1400 cm^{-1}, which was identified by Spiro and co-workers as "Amide S" (AS) for its sensibility to the peptide structure [101]. This band is related to the $C_\alpha - H$ bending mode and its resonance enhancement derives from the mixing of the $C_\alpha - H$ bending coordinates with those of AIII [102, 103, 104]. Fig. 3.5(a) evidences the existence in the spectra of dry GSH of a Raman peak at 1707 cm^{-1} that is assigned to the carboxylic (COOH) stretching vibration of GSH. This band is clearly visible at 1730 cm^{-1} in the UVRR spectrum of hydrated GSH at pH= 3 where the tripeptide is mainly present in its $GSH_{-\alpha 1}$ form, while the peak disappears in the spectrum at pH= 8 where the most abundant form of glutathione is the $GSH_{-\alpha 12}$. Accordingly, this is accompanied by an increment in the spectrum of GSH at pH= 8 of the signal at 1400 cm^{-1} where the stretching vibration of carboxylate group (COO^-) is expected to fall. In the spectrum of the GSH solutions compared to that of its dry form, a blue shift of the COOH signal is observed and this suggests that when the peptide is solvated by water a weakening of the hydrogen bonds involving the C$=$O groups takes place. This

effect is consistent with the upshift of the signal associated to the stretching of SH from 2527 cm^{-1} (dry GSH) to 2582 cm^{-1} (solutions of GSH) due to solvation effect. The occurrence of stronger H-bonds that involve the terminal moieties of GSH, i.e. COOH and SH groups, in dry with respect to solvated tripeptide may be consistent with the close packing of the molecules of GSH in the dry powders.

Figure 3.5(b) points out that the frequency of AI band shows a slight pH-dependence for solution of GSH. Conversely, moving from acid to basic environment a red shift of AII ($\Delta\nu_{AII}$= -21 cm^{-1}) and AIII ($\Delta\nu_{AIII}$= -13 cm^{-1}) bands is found. Because both these two molecular vibrations contain a large C——N stretching contribution, their pH-sensitivity is ascribed to the strict relationship that exists between the C——N oscillator strength and the type of side group bonded to the amide nitrogen. Electron-withdrawing groups linked to the amide nitrogen perturb the C——N oscillator strength in proportion to the magnitude of their inductive effect and their capacity to decrease the electron density on the nitrogen atom. Therefore, the red-shift undergone by AII and AIII bands at pH= 8 where the glycine residue of GSH exists mainly in its deprotonated state can be explained on the basis of the lower electron-withdrawing character of carboxylate anion (COO^-) with respect to the carboxylic group (COOH) [89]. Figure 3.6 shows the comparison between the UVRR spectra collected at room temperature for a diluted and concentrated solution of GSH at pH= 3 and 8.

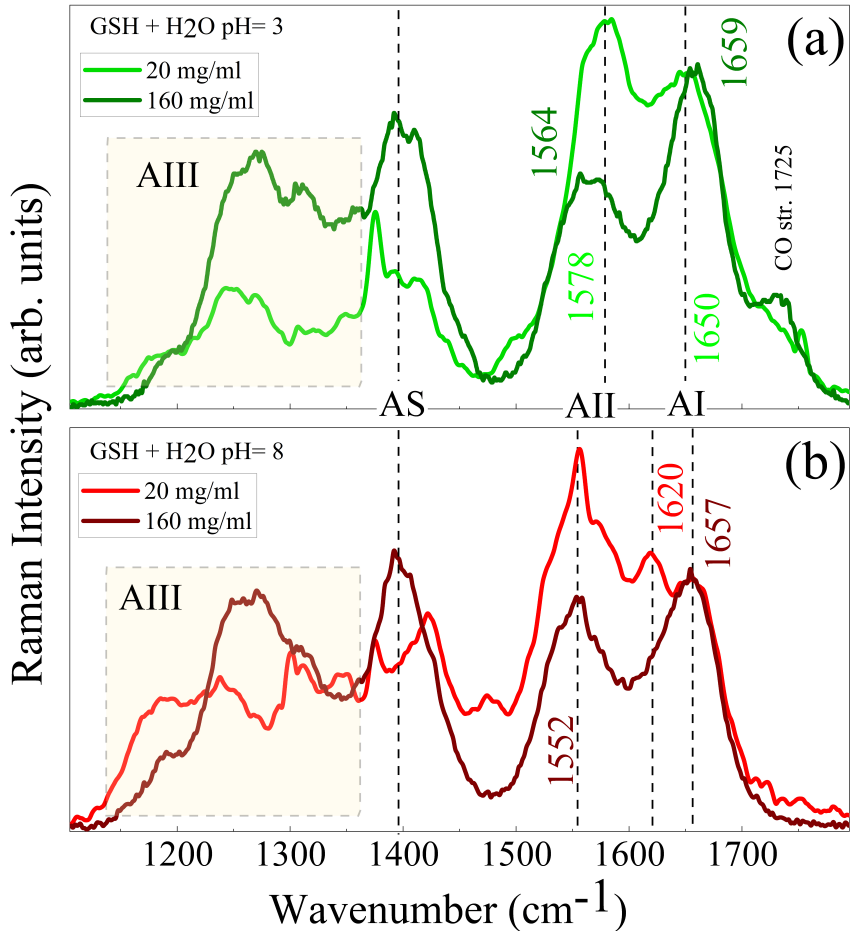

FIGURE 3.6: UVRR spectra ($\lambda_{exc} = 266$ nm) collected at room temperature for diluted (20 mg/ml) and concentrated (160 mg/ml) solutions of GSH at pH= 3 (a) and pH= 8 (b); the spectra are shown in the Amide region and they have been arbitrarily normalized on the intensity of AI for a better visualization.

At the lowest investigated concentration of GSH (20 mg/ml), 870 molecules of water per peptide are available, whereas at the highest concentration (160 mg/ml) the tripeptide is solvated by 106 molecules of solvent. By looking at the concentration dependence of the spectra in the case of the acid solution of GSH (figure 3.6(a)), the AI band appears broader in the diluted conditions with respect to high-concentrated situation. This finding is rationalized considering a picture where in the highly solvated GSH, the C$=$O groups of tripeptide can be involved in more than one H-bond with surrounding water molecules. This is consistent with the presence of C$=$O oscillators with a slight different strength that co-exist in the same system giving rise to a broadening of the AI mode. Increasing the concentration from 20 to 160 mg/ml, the number of water molecules available in the hydration shell for each peptide decreases eight fold, and the C$=$O groups result mainly involved in only one H-bond. This interpretation is confirmed by the upshift (from 1650 to 1659cm^{-1}) observed for the AI band at high concentration of peptide since less strongly

H-bonded C$=$O groups are expected to vibrate at higher frequency. In line with this picture, the downshift observed for AII band from 1578 to 1564 cm^{-1} in the spectra of figure 3.6(a) can likewise be explained by the reduction of the C$-$N bond length in the amide groups upon decreasing of the number of water molecules bonded on C$=$O site [60, 99, 100, 105].

Figure 3.6(b) shows the concentration dependence of the spectra of GSH solution at pH= 8. In this condition the Amide site is more solvated compared to the situation at pH=3, because the COO$-$ group of the glycine (favoured at pH= 8) has a less pronounced electron-withdrawing character with respect the COOH group (favoured at pH= 3). Therefore, the electron density on the Amide nitrogen atom is less perturbed at basic conditions respect to acid ones, making the C$=$O electronic doublets more available to interact via H-bond with hydration water molecules. This situation promotes, in the diluted GSH solution at pH= 8, the splitting of AI band in two components, clearly detected at 1657 cm^{-1} (C$=$O weakly bonded) and 1620 cm^{-1} (C$=$O strongly bonded). The component at 1620 cm^{-1} is more intense than that at 1657 cm^{-1}, suggesting that the carbonyl groups interacts mainly using both electronic doublets. In agreement with the concentration-dependence already observed in figure 3.6(a), also at basic condition, increasing the concentration from 20 to 160 mg/ml only the component of AI mode associated to the C$=$O more weakly bonded remains evident in the UVRR spectrum. Both panels (a) and (b) of figure 3.6 show that solvation of GSH enhances the UVRR cross-section of AII mode, in agreement with what previously observed for other peptides [61]. This effect can be rationalized considering the changes in C$=$O and C$-$N bond lengths with solvation. In particular, the formation of hydrogen bonds between peptide sites and water molecules stabilizes the ground state dipolar resonance ($^{-}$O$-$C$=$$NH_2^+$) structure that becomes more favored with respect to the neutral resonance structure (O$=$C$-$$NH_2$) [61]. The contraction of the C$-$N bond length induces an increment of the displacement between the electronic ground and excited states along the C$-$N coordinate, which results in an enhancement of the Raman cross section of the AII vibrational modes. These solvation effects on the peptide sites of GSH are accompanied by the spectral changes observed in figure 3.6 for the AS and AIII bands that can be correlated with both the changes of the peptide's dihedral angles and the establishment of H-bond links between the water molecules and the Amide site [49, 100].

3.2.3 Deuteration and temperature effect on Amide bands

Figure 3.7(a) and (b) report the UVRR spectra collected at 5 and 50°C of GSH dissolved in aqueous solution at pH= 8 and pH= 3, respectively. In addition, the spectra of GSH dissolved in deuterium oxide at pH= 3 can be inspected in figure 3.7(c). In D_2O environment the hydrogens linked to S, N and O atoms in the molecule of GSH can be replaced by deuterium and this H/D exchange leads to very different spectral features in the UVRR spectra of peptide in D_2O compared to those obtained in H_2O (figure 3.7(b) and (c)). This effect is here exploited in order to better resolve the normal mode composition of the Raman bands of peptide that exhibit the most important temperature variations.

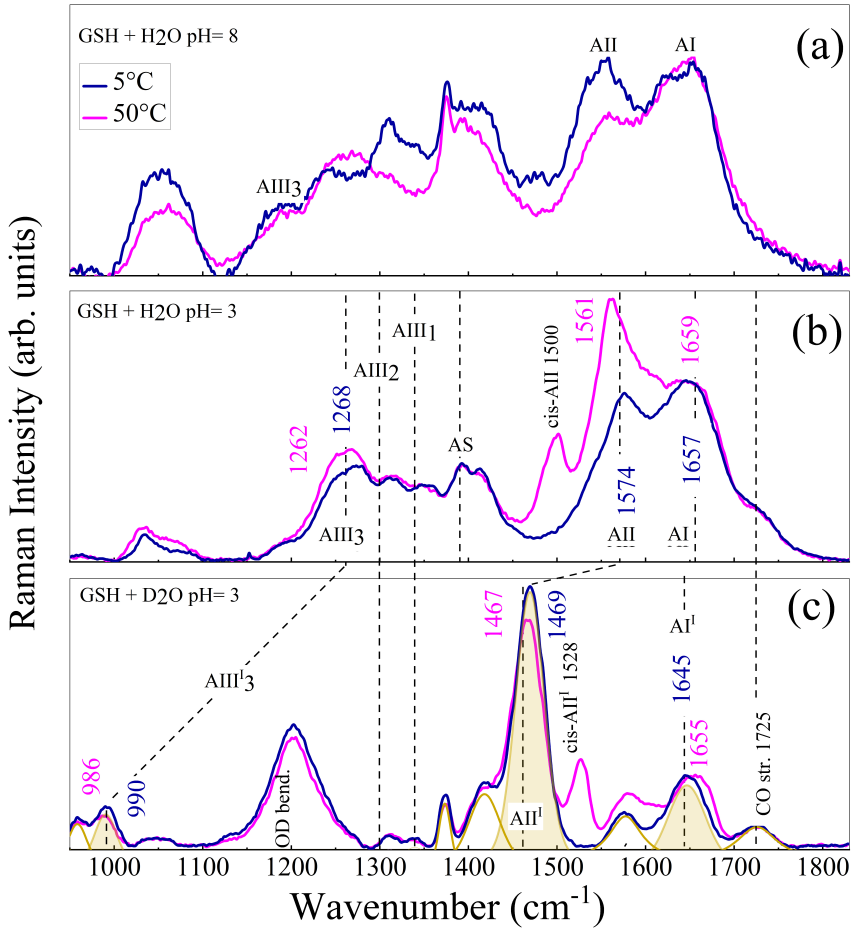

FIGURE 3.7: UVRR spectra (λ_{exc} = 266 nm) collected at 5 and 50°C for GSH (20 mg/ml) in H_2O at pH= 8 (a) and (b) at pH= 3; (c) spectra of GSH dissolved in D_2O (20 mg/ml) at pH=3 at the two temperatures, 5 and 50°C. The spectra are shown in the Amide region and they have been arbitrarily normalized on the intensity of AI (a, b) and AII (c). An example of fitting procedure of the main bands is reported for the UVRR spectrum of GSH in D_2O (yellow lines and shaded areas).

The frequency position of AI^I band is not sensibly affected by the H/D isotopic exchange, probably because of its strong C$=\!=$O stretching character. On the contrary, the downshift

of 106 cm^{-1} observed for AII^{I} band, due to deuterium mass substitution, can be explained with the main character of N—H bending of the Amide II vibrational mode. Similarly, the deuterium substitution on the N sites of GSH leads to a band shifts of $AIII_3$ from 1273 to 992 cm^{-1}. The bands labelled as $AIII_2$ and $AIII_1$ do not fully disappear in the spectra of figure 3.7(c), suggesting that both these signals have an important N—H bending contribution although even CN, CO and $C\alpha C$ molecular movements participate to the $AIII_2$ and $AIII_1$ vibrations. Moreover, to further support these assignments, as it can be noted in the spectra of figure 3.7(c) $AIII_2$ and $AIII_1$ peaks exhibit a poorly temperature dependence [60, 106]. By inspection of figure 3.7 (a) and (b) it appears that the increasing of temperature from 5 to 50°C causes in both the solutions of GSH at pH= 3 and 8 a slight upshift of the AI band along with a more pronounced downshift of the AII and $AIII_3$ signals. Similar changes in the frequency positions of Amide bands have been previously observed in the case of other peptides [107] and these trends have been related to the effect induced by hydrogen-bond on the oscillation strength of Amide modes [99]. In order to extract more quantitative information on the temperature-dependence of the amide bands, the experimental UVRR profiles have been fitted by employing a minimum number of Voight functions. An example of the fitting results is shown in figure 3.7(c) for GSH in D_2O at 5°C. Figure 3.8 reports the temperature-dependent evolution of the wavenumber position of Amide bands for glutathione in H_2O and D_2O obtained by the fitting procedure.

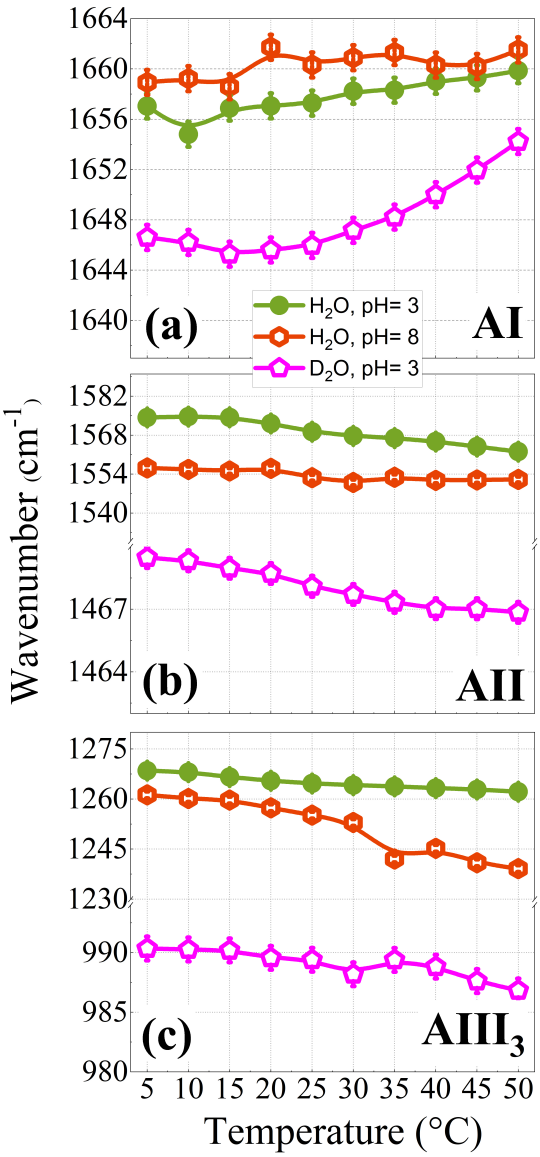

FIGURE 3.8: Temperature-dependence of wavenumber position observed for AI (a), AII (b) and $AIII_3$ (c) bands for GSH dissolved in H_2O at pH=3 and 8 and dissolved in D_2O at pH= 3

Despite the statistical fluctuations affecting some set of data in figure 3.8, the blue shift of AI and the red shift of AII and AIII bands due to the temperature increase are clearly recognizable within the experimental error. These trends observed for the wavenumber positions of Amide bands reflect the progressive weakening of the hydrogen bonds between water molecules and the amide carbonyl and N——H groups of GSH, due to the increasing thermal motion. The opposite temperature behavior, down- or up-shift, reported for AII and AIII with respect to AI in figure 3.8 can be rationalized by considering the different normal mode composition of these bands [99]. In particular, the sensitivity to hydrogen-bonds strength of the AI mode mainly derives from the C═══O group of the peptide, while

the frequency dependence of the AII vibration is primarily due to the H-bond involving the N——H groups of the peptide linkage. Interestingly, the plots in figure 3.8 provide evidence that the pH does not seem to significantly affect the temperature dependence of Amide bands of GSH.

More remarkably, differences in the dependence on temperature is observed for the Amide vibrations of glutathione in D_2O solution. The AI^I band undergoes a more significant up-shifts (+0.22 $cm^{-1}/°C$) with respect to the shift found for AI (+0.04 $cm^{-1}/°C$) signal in H_2O. Conversely, increasing of thermal motion has only a slight effect on AII^I band that down-shifts of about 0.04 $cm^{-1}/°C$ with respect to the change of -0.29 $cm^{-1}/°C$ observed for the frequency position of AII. Finally, the temperature-dependence of $AIII_3^I$ and $AIII_3$ is quite comparable since they move towards lower frequency by 0.09 $cm^{-1}/°C$ and 0.13 $cm^{-1}/°C$, respectively. By looking to the profiles of figure 3.7(b) and (c), it clearly appears that the increase of temperature causes in the spectra collected both in light and heavy water the progressive increment of a signal observed at 1500 cm^{-1} in H_2O and at 1528 cm^{-1} in D_2O. These two signals have been assigned to the cis-amide bands (cis-AII and cis-AII^I, respectively) and they mark the conformational change from trans to cis isomer of the peptide group of GSH [89, 108] promoted by the temperature increase. It has to be noted that the intensity of the cis–AII band increases with the enhancement of thermal motion without any frequency shift, whilst the trans–AII and –AIII bands down-shift of 16 and 5 cm^{-1} respectively (figure 3.7(b)) [109]. This finding suggests that cis–AII signal is mainly due to C——N stretching mode [49, 110].

3.2.4 Ions effect on GSH structure and hydration

Figure 3.9 shows the spectra of aqueous GSH solutions in the presence of different halogenic ILs compared with those of inorganic salts with the same anion, at 20 °C. The spectrum of GSH dissolved in pure water (blue line) is used as a reference.

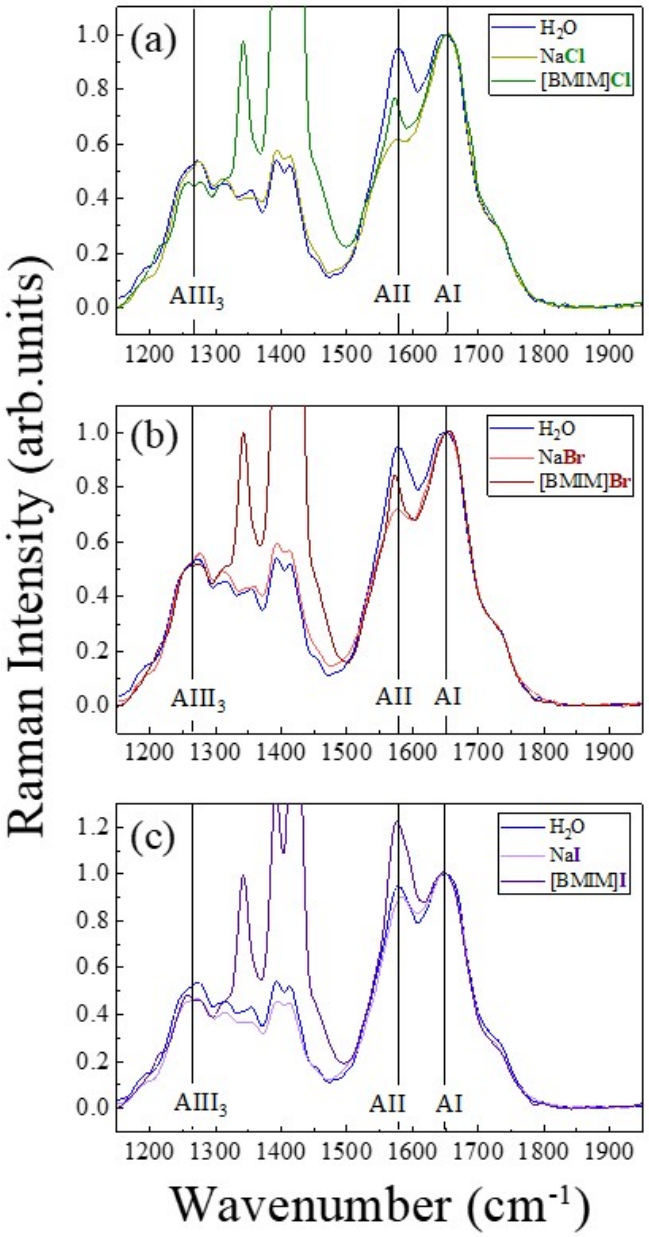

FIGURE 3.9: spectra of GSH in the different solvation environments collected at 20 °C. Panel (a) comparison between IL and inorganic salt with chloride anion, panel (b) comparison between IL and inorganic salt with bromide anion and panel (c) comparison between IL and inorganic salt with iodide anion. The spectrum of GSH solved in pure water is used as a reference (blue line).

From the spectral features of figure 3.9 is evident how the different solvation environments influence both the frequency position and the relative intensities of the Amide signals [99]. The spectra show that with the same anion, the ionic liquids and the inorganic salts act in the same direction but do not differ too much from each other. Despite the great difference of the used cation ($[BMIM]^+$ and Na^+) no marked differences as regards the bands frequency and the spectral shape are found. The biggest difference is on the AII and AI bands relative intensities. The use of a different cation does not seem to have a great influence on the spectral features. Therefore, to deeply investigate the effect of the different cation on the peptide site, molecular dynamic simulations are performed. From UVRR experiments and even in previous literature works, effectively seems that the anion plays a predominant role in influencing the peptides and proteins solvation [46, 39]. Figure 3.10 shows the distribution of ring H-atoms of $[BMIM]^+$ around the carboxylate group of glutamate residue of GSH in aqueous solution of [BMIM]Br. In this study, the hydrogen atoms of $[BMIM]^+$ ring are denoted H1, H2, and H3.

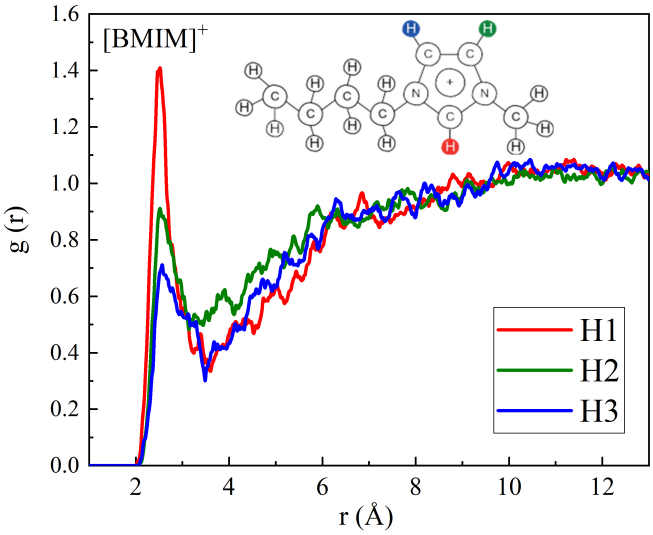

FIGURE 3.10: RDF of the hydrogen atoms of imidazolium-ring around the carboxylate group of glutamate residue of GSH in aqueous solution of [BMIM]Br. In the inset, the chemical structure of 1-butyl-3 methylimidazolium [BMIM] cation is shown. H: Ring H-atom (H1), H: Ring H-atom (H2) and H: Ring H-atom (H3).

Figure 3.10 confirms that the H1 atom of imidazolium-ring is the most affine to the carboxylate group of GSH, due to its highest positive charge density in comparison to the other hydrogen atoms. The kosmotropic carboxyl moiety [111] of GSH is strongly hydrated by water molecules, and the interaction between the H1 of kosmotropic imidazolium cation is

weak than water molecules as evidenced in figure 3.11.

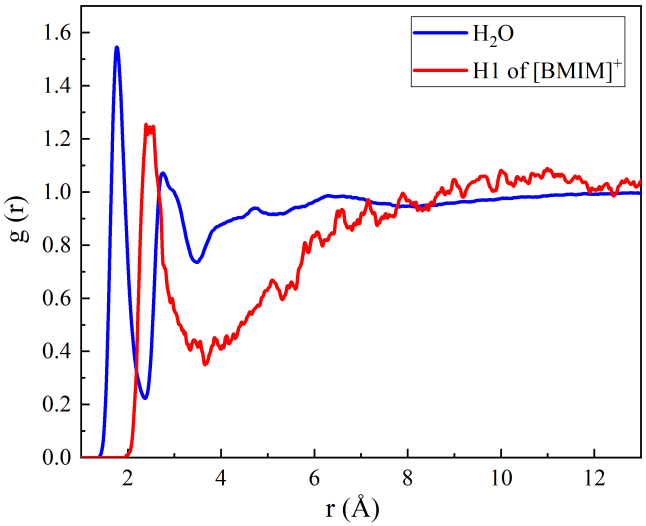

FIGURE 3.11: RDF of water molecules and H1 atom of imidazolium-ring around the carboxylate group of glutamate residue of GSH in the aqueous solutions of [BMIM]I at 27 °C.

In order to understand the effect of ionic pair formation on the solvation structure of GSH, contact ion pair have been derived from MD trajectory by performing RDF of cations and anions.

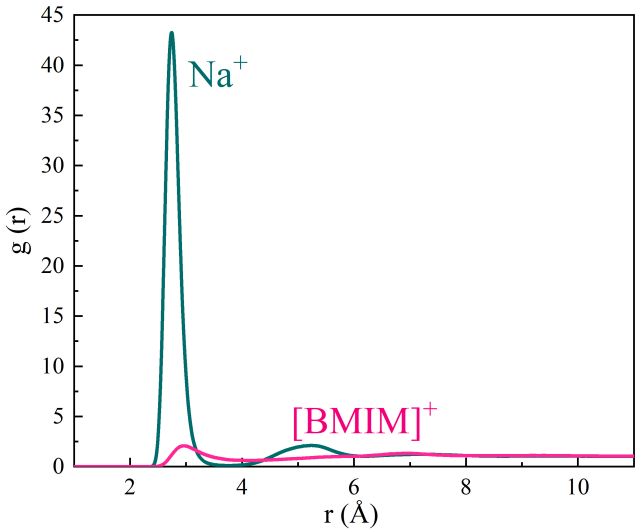

FIGURE 3.12: RDF of chloride anions around the cations in the aqueous solutions of [BMIM]Cl and NaCl at 27 °C.

According to figure 3.12, H1 results the most acidic proton of $[BMIM]^+$ cation, and have small affinity to make contact ion pair with chloride anion in comparison to Na^+ cation.

Contact ion pair occur in solution and the effect of the anion on the solvation structure of GSH is more damped in the inorganic salts in comparison to the solutions of ionic liquids as shown by figure 3.13.

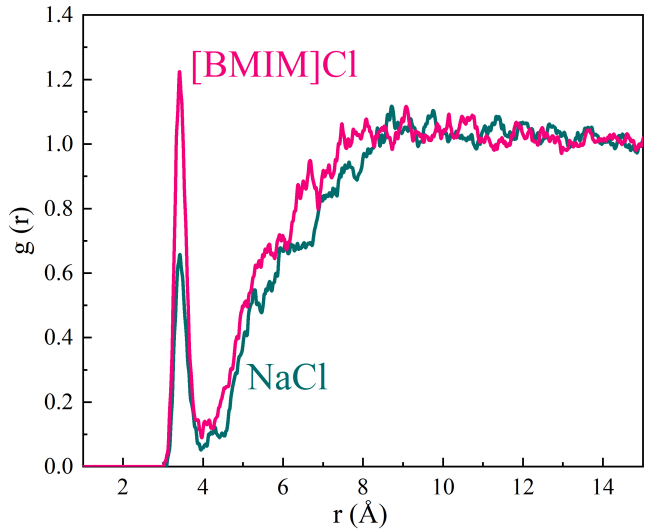

FIGURE 3.13: RDF of chloride anions around the nitrogen atom of cysteine residue of GSH (N2) in the aqueous solutions of [BMIM]Cl and NaCl at 27 °C.

According to the RDF analysis, it can be concluded that the halide anions of ionic liquids have the greatest effect on solvation structure of amide carbonyl groups of GSH in comparison to the inorganic salt, since Na^+ has a greater propensity to form ionic pairs. Evidently, this effect is not so marked to be noticed experimentally. Moreover, according to the MD simulation, the cations do not have significant effect on dihedral angles of GSH therefore no strong conformational changes due to cations occur in the studied solutions. This theoretical result is in total agreement with the experimental findings, indeed the spectral features are similar in all the investigated environments.

According to literature findings, is evident from our experiments that the anion have the main effect on changing the interaction potential of GSH in solution. The presence of chloride in the solvation environment, with both cation ($[BMIM]^+$ and Na^+) generate a slight upshift of AI and a more visible downshift of AII signal (see figure 3.9(a)). This effect could assigned to the direct interaction of the ions with the GSH structure and/or to the alteration of the hydration shell around the peptide link. The behavior of the amide bands in terms of intensity and frequency variation can be rationalized in terms of the resonance equilibrium of the peptide link. Indeed peptides exists in solution in both the neutral form and the zwitterionic one.

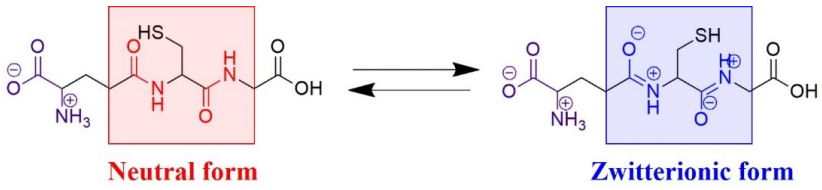

FIGURE 3.14: equilibrium between the neutral and the zwitterionic form of the peptide link in GSH tripeptide.

The equilibrium between these two forms can be shifted toward one of the two, depending on the solvation environment.

The energetic situation that favors the amide dipolar resonance structure ($^{-}O-C=NH_2^{+}$) increase the intensity of the AII vibrational band due to the C—N stretching contribution on generating it. While the amide neutral resonance structure (O=C—NH_2) lead to an increase of the Raman cross section of the AI band [101]. Even the force constant of the oscillators is affected by the greater stabilization of one of the two resonance structures. In fact, the strengthening of the C—N bond with respect to C=O in the dipolar form leads a blue shift of AII and a red shift of AI band. The opposite trend occurs when the C=O double bond character is increased over the C—N one. Analyzing the intensity and the frequency of AI and AII bands in the ions solutions with respect to that of GSH dissolved in pure water, information on the alteration of solvation environment are obtained.

Based on the resonance model, the interaction between peptide link and Cl^{-} increases the C=O bond character, resulting in a frequencies shift of the amide signals than those obtained for pure water, and on the greater intensity of the AI signal than that of AII. The frequencies shift and the intensity relation of the amide bands is due to the highest stabilization of the amide neutral resonance structure (figure 3.14) induced by the Cl^{-} anion. Bromide anion (figure 3.9 (b)) shows the same type of effect on the UVRR spectral features and presumably, the same type of interaction with peptide link observed for the chloride anion. The effect of bromide is lower than that induced by chloride. In agreement to the experimental findings, the MD simulations results are illustrate in figure 3.15, that shows the distribution of the anions around the nitrogen atom of cysteine residue (N2) at 27 °C.

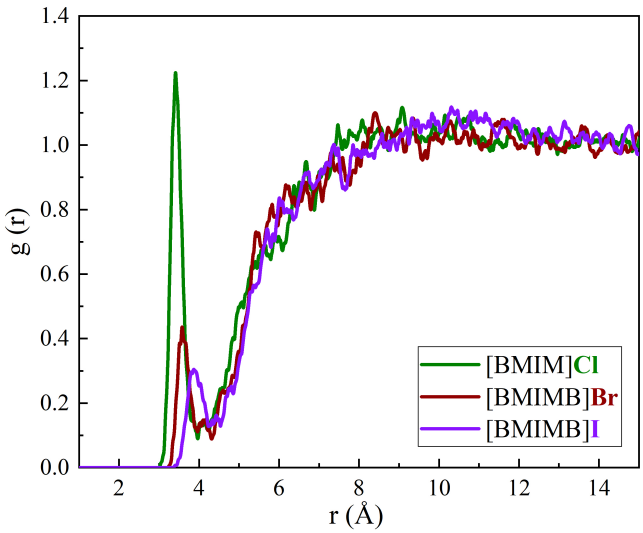

FIGURE 3.15: RDF of anions around the nitrogen atom on cysteine residue of GSH (N2) in the aqueous solutions of [BMIM]Cl, [BMIM]Br and [BMIM]I.

According to figure 3.15, it can be concluded that chloride and bromide ions come closer to the N—H site of the peptide links in GSH. The distribution of chloride ions around the nitrogen atoms of GSH is higher in comparison to bromide ones, due to the higher charge density of chloride. Molecular dinamic simulations have seen no changes on GSH dihedral angles. UVRR and MD simulation outputs highlight that chloride and bromide due to their high charge density, approach the N—H site of the peptide bond at the expense of the water molecules. The number and/or the strength of the hydrogen bonds at the peptide site decreases compared to GSH in pure water. The reduced polar environment stabilizes the GSH neutral resonance structure, resulting in a blue shift of AI, a red shift of AII and a stronger intensity of AI than AII (figure 3.9 (a) and (b)).

The effect of iodide anion compared to those induced by chloride and bromide, acts in the opposite direction as regards both the frequency and the relative intensity of AI and AII bands. Figure 3.9 (c), shows that iodide promote a downshift of AI, an upshift of AII band and an intensity enhancement of the AII signal with respect to AI, especially for the solution with [BMIM]I.

Figure 3.16 shows RDF of water molecules around the amide carbonyl of glutamate residue of GSH (O3) in pure water and in the aqueous solutions of [BMIM]I and NaI at 27 °C.

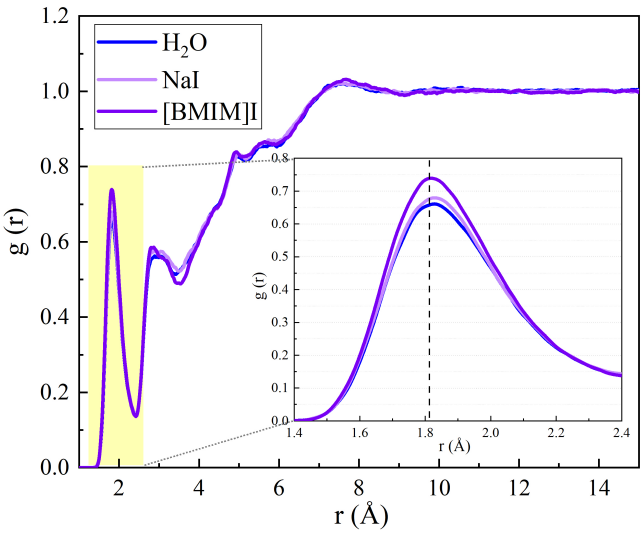

FIGURE 3.16: RDF of water molecules around the amide carbonyl of glutamate residue of GSH (O3) in pure water and aqueous solutions of NaI and [BMIM]I at 27 °C.

The graph shows that there is the highest distribution of water molecules around O3 in aqueous solution of [BMIM]I and NaI in comparison with water solution. According to these results, at a distance of 1.8 Å, water molecules solvate O3 of GSH at 0.66, 0.68 and 0.74 g(r) values for water, NaI and [BMIM]I, respectively. This finding is in good agreement with experimental results i.e. the frequency of AI at 27 °C is red shifted in presence of iodide anion. Accordingly, MD results find more water molecules around O3 in aqueous solutions of NaI and [BMIM]I. The solvation status of GSH shows similar trend for both amide carbonyl groups of GSH. The experimental and theoretical common view suggests that the iodide presence in solution generates an increment of the water molecules around the peptide bond creating a strong polar solvation environment. The increased polarity (hydrogen bonds) results in a stabilization of the GSH dipolar resonance structure with a red shift of AI, a blue shift of AII band and an intensification of the AII signal.

The temperature dependence of the hydrogen bond network of GSH solution in the binary water/salts mixtures has been investigated, using as a reference the temperature dependence of the tripeptide in pure water that are previously discussed in the subsection 3.2.3. It is possible to take a look this effect directly from the spectra at the lowest and the highest temperature shown in figure 3.17 of this chapter. The spectra of GSH in pure water, shown in panel (a) of figure 3.17 is used as a reference. The spectra of GSH with the presence of ILs are shown in the left panels while those with inorganic salts in the right ones.

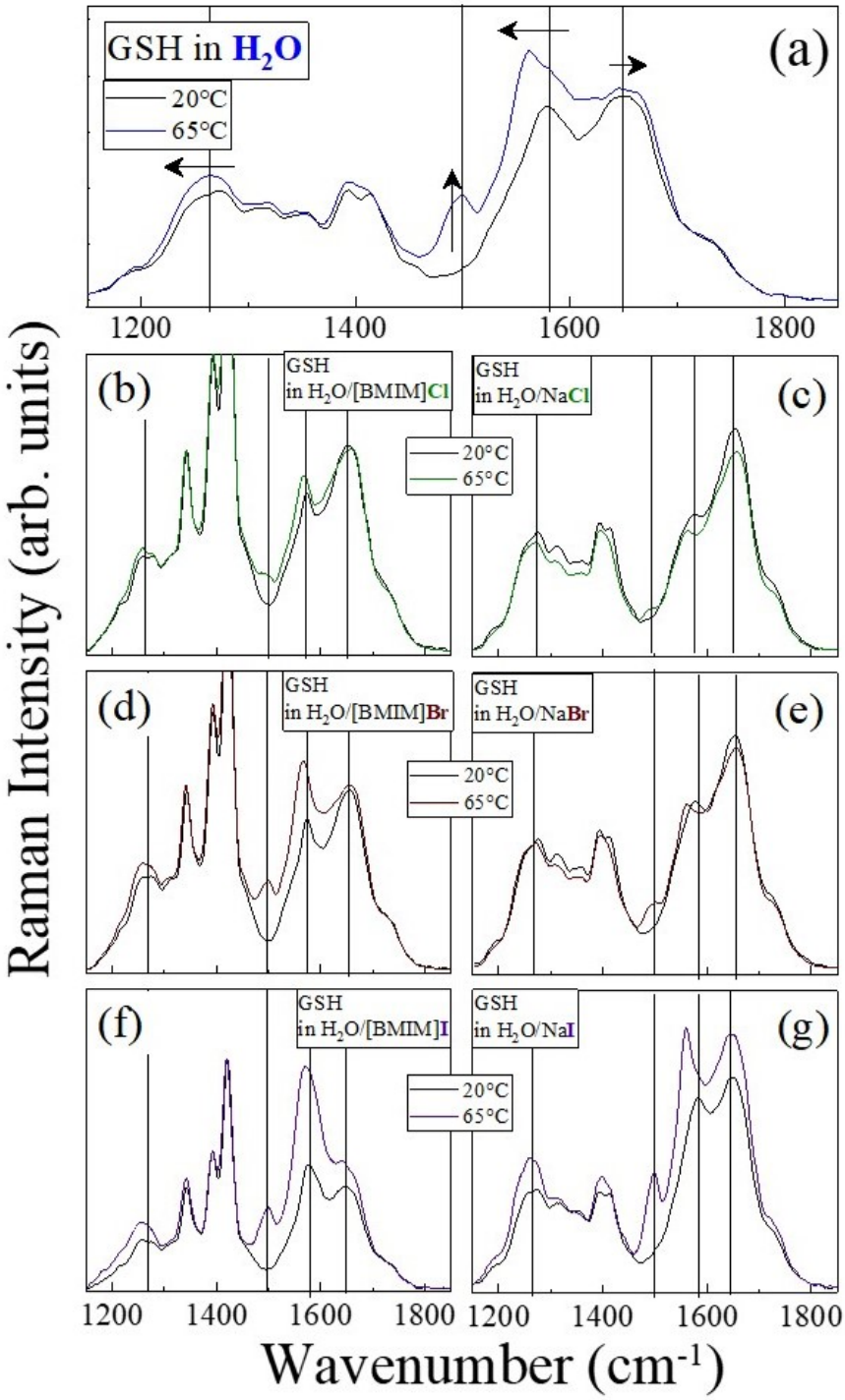

FIGURE 3.17: spectra of GSH in the different solvation environments collected at 20 and 65 °C. The spectrum of GSH dissolved in pure water is used as a reference (panel a), this latter is compared with the samples that contain the salts (right panels c, e and g) and, with those that contain the ionic liquids (left panels b, d and f).

The outputs indicate that the increase of temperature downshifts the AII and $AIII_3$ band frequencies, while the AI band shows a small upshift. This behavior is a direct consequence of the GSH-water hydrogen bonds weaken. As amply discuss in literature the opposite shift of the AI band with respect to AII and $AIII_3$ bands is due to their different normal modes

composition. In fact because of the weakened of the H-bond between GSH and water at the C═O and N—H sites, both bonds get shorter with a consequent lengthens of the C—N bond.

The following figures (from figure 3.18 to figure 3.24) show the radial distribution functions of water molecules around the GSH hydrogen of cysteine residue (H11), the hydrogen of glycine residue (H15), the amide carbonyl of glutamate residue (O3), the amide carbonyl of glutamate residue (O4); and the analysis of the normalized average dihedral angle of GSH (O3-C4-N2-H11) and (O4-C8-N3-H15) at three different temperature value 27, 47 and 67 °C.

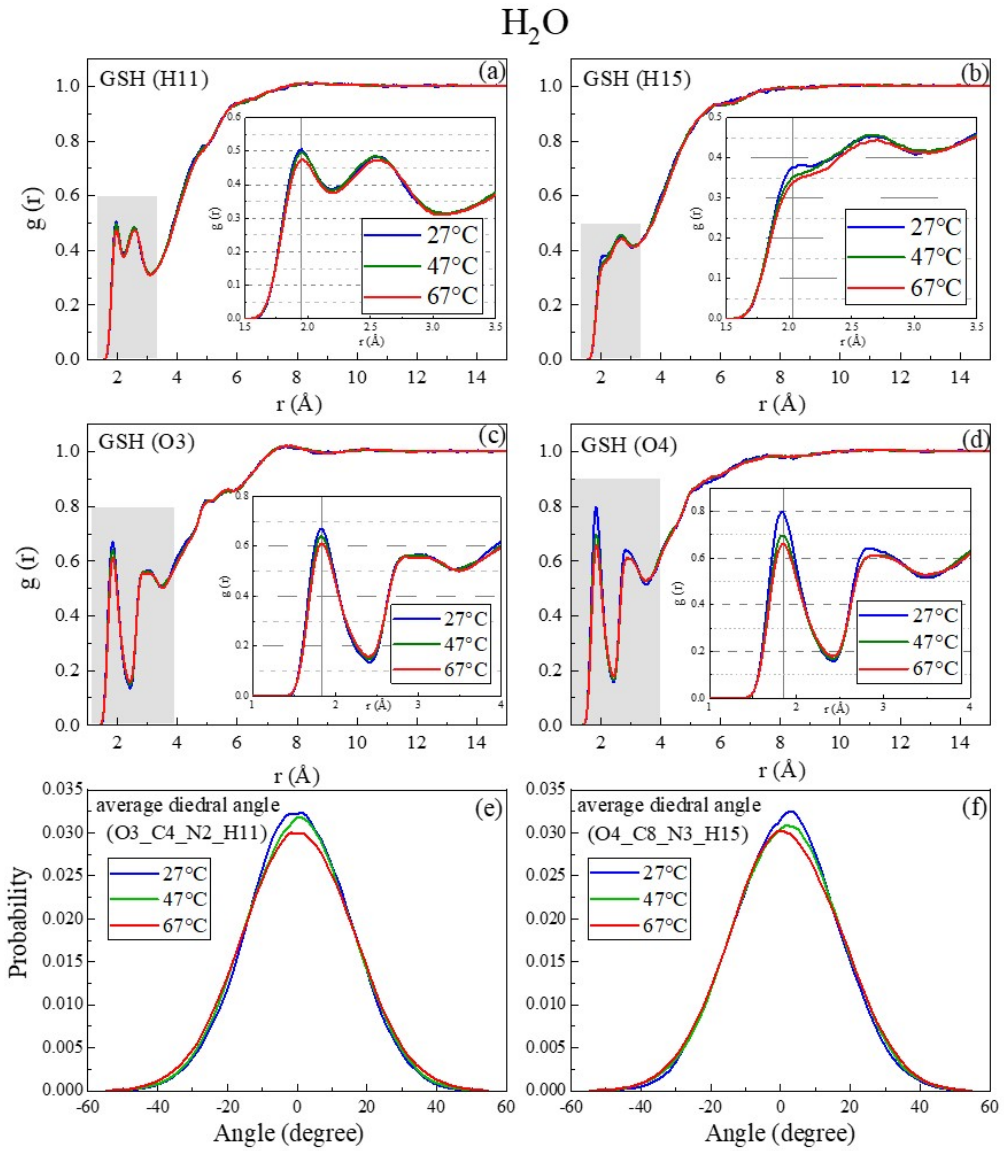

FIGURE 3.18: RDF of water molecules around the GSH (a) hydrogen of cysteine residue (H11), (b) hydrogen of glycine residue (H15), (c) amide carbonyl of glutamate residue (O3) and (d) amide carbonyl of glutamate residue (O4), in pure water at three different temperature value 27, 47 and 67 °C. Analysis of the normalized average dihedral angle of GSH (e) (O3-C4-N2-H11) and (f) (O4-C8-N3-H15), in pure water at three different temperature value 27, 47 and 67 °C.

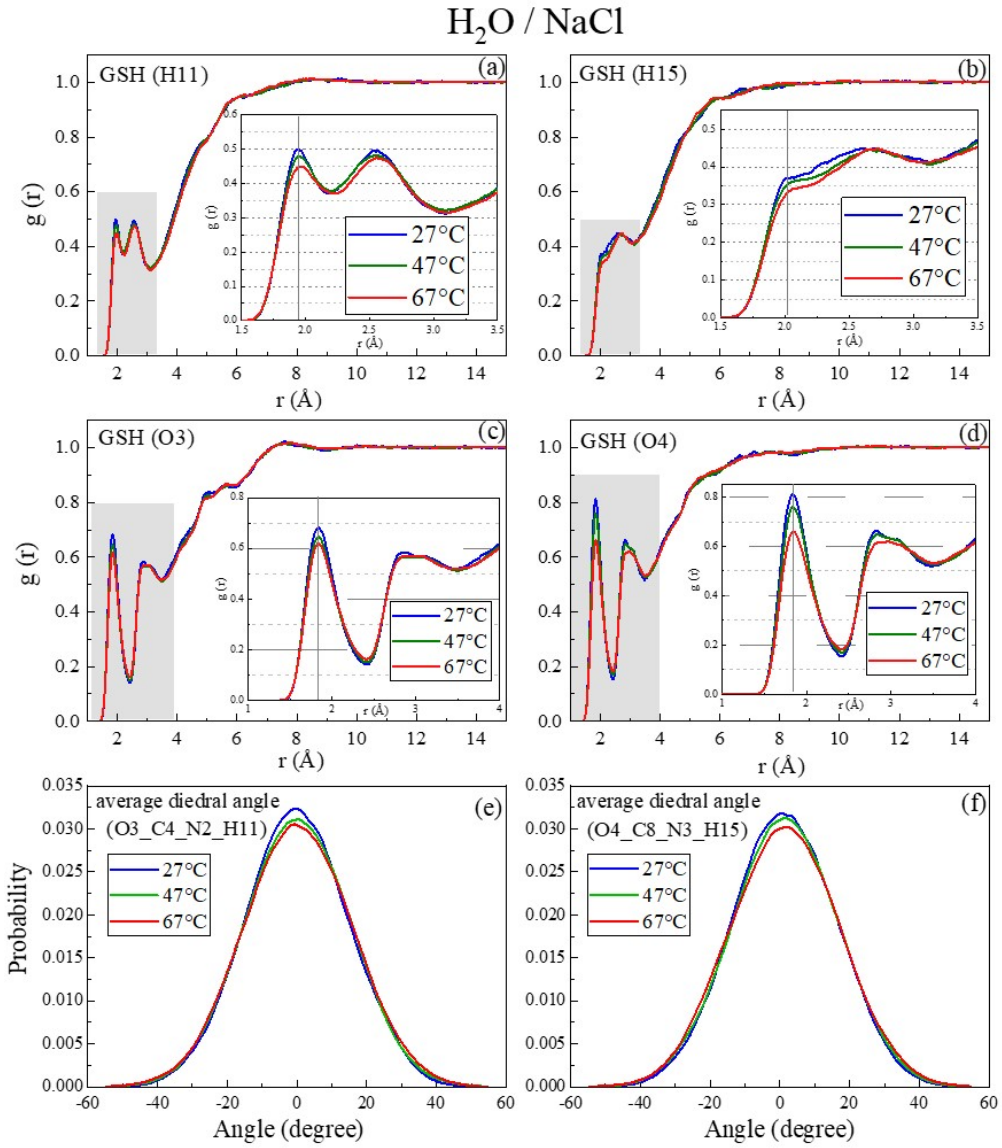

FIGURE 3.19: RDF of water molecules around the GSH (a) hydrogen of cysteine residue (H11), (b) hydrogen of glycine residue (H15), (c) amide carbonyl of glutamate residue (O3) and (d) amide carbonyl of glutamate residue (O4), in water/NaCl mixture at three different temperature value 27, 47 and 67 °C. Analysis of the normalized average dihedral angle of GSH (e) (O3-C4-N2-H11) and (f) (O4-C8-N3-H15), in water/NaCl mixture at three different temperature value 27, 47 and 67 °C.

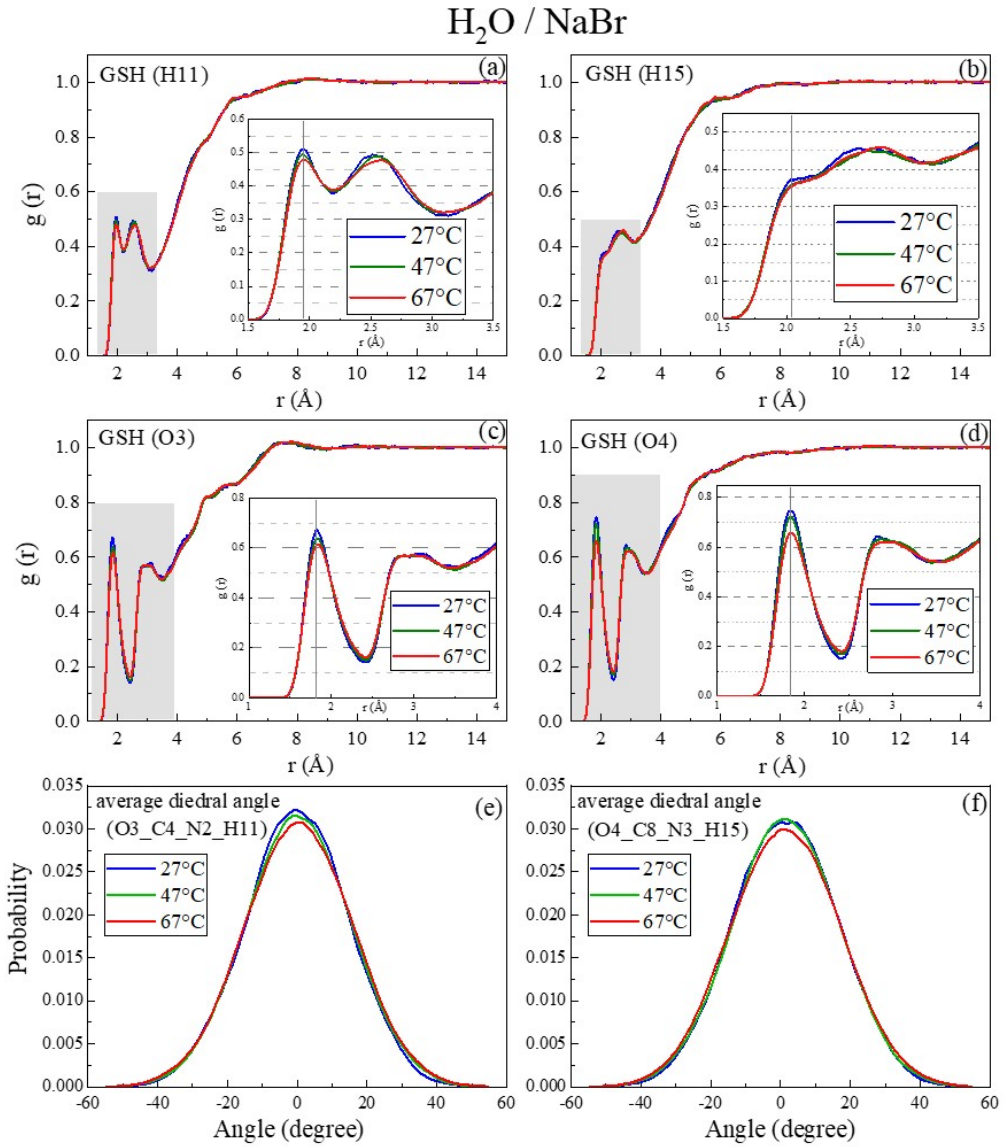

FIGURE 3.20: RDF of water molecules around the GSH (a) hydrogen of cysteine residue (H11), (b) hydrogen of glycine residue (H15), (c) amide carbonyl of glutamate residue (O3) and (d) amide carbonyl of glutamate residue (O4), in water/NaBr mixture at three different temperature value 27, 47 and 67 °C. Analysis of the normalized average dihedral angle of GSH (e) (O3-C4-N2-H11) and (f) (O4-C8-N3-H15), in water/NaBr mixture at three different temperature value 27, 47 and 67 °C.

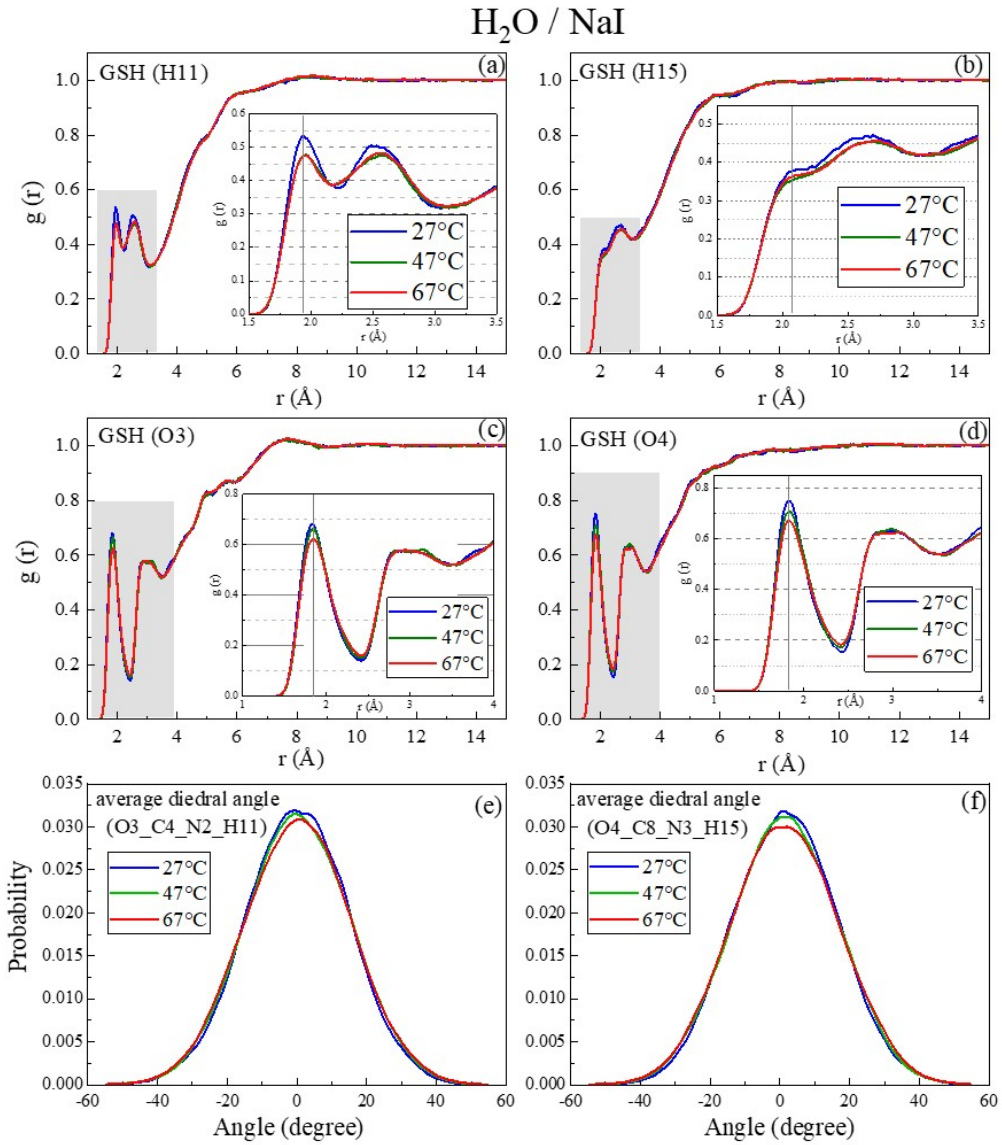

FIGURE 3.21: RDF of water molecules around the GSH (a) hydrogen of cysteine residue (H11), (b) hydrogen of glycine residue (H15), (c) amide carbonyl of glutamate residue (O3) and (d) amide carbonyl of glutamate residue (O4), in water/NaI mixture at three different temperature value 27, 47 and 67 °C. Analysis of the normalized average dihedral angle of GSH (e) (O3-C4-N2-H11) and (f) (O4-C8-N3-H15), in water/NaI mixture at three different temperature value 27, 47 and 67 °C.

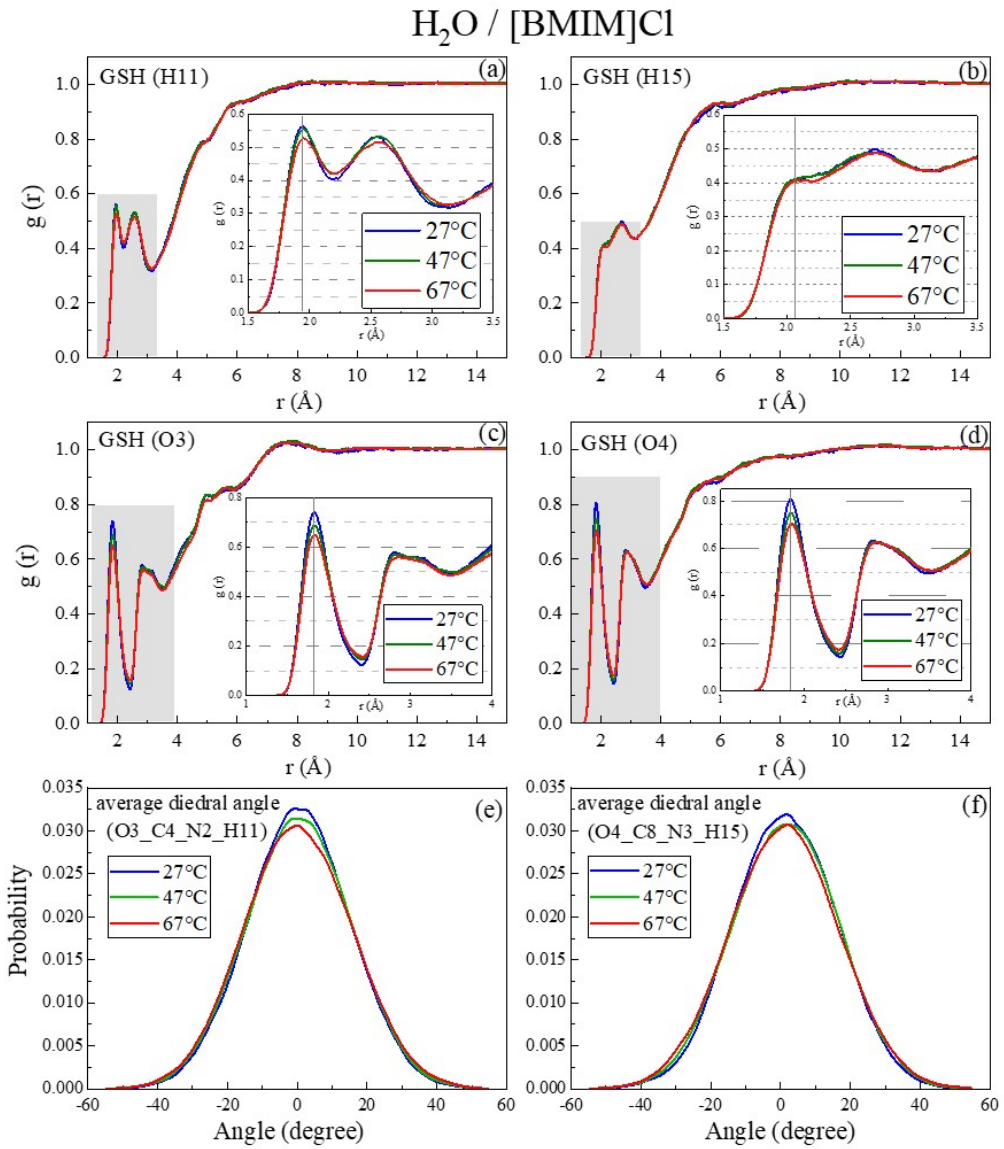

FIGURE 3.22: RDF of water molecules around the GSH (a) hydrogen of cysteine residue (H11), (b) hydrogen of glycine residue (H15), (c) amide carbonyl of glutamate residue (O3) and (d) amide carbonyl of glutamate residue (O4), in water/[BMIM]Cl mixture at three different temperature value 27, 47 and 67 °C. Analysis of the normalized average dihedral angle of GSH (e) (O3-C4-N2-H11) and (f) (O4-C8-N3-H15), in water/[BMIM]Cl mixture at three different temperature value 27, 47 and 67 °C.

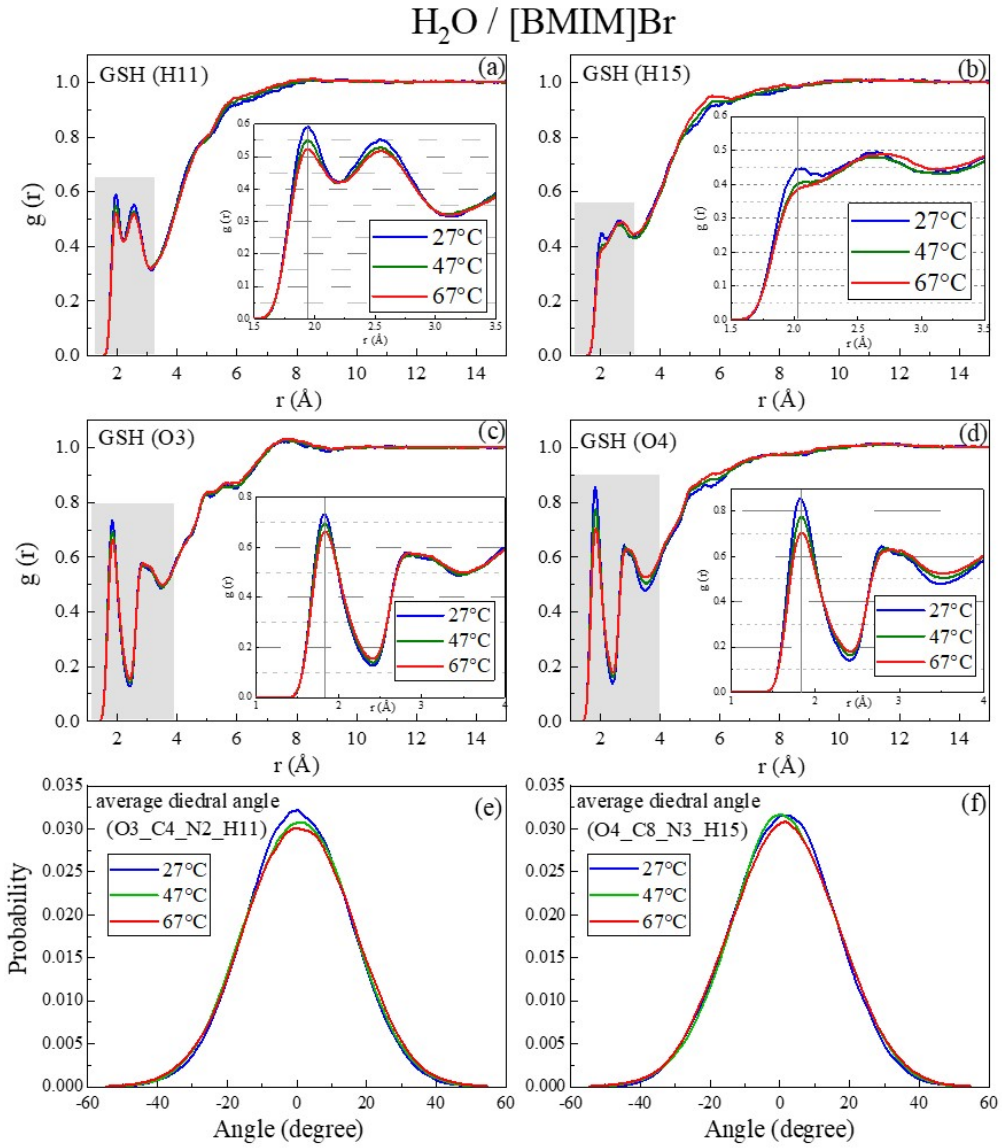

FIGURE 3.23: RDF of water molecules around the GSH (a) hydrogen of cysteine residue (H11), (b) hydrogen of glycine residue (H15), (c) amide carbonyl of glutamate residue (O3) and (d) amide carbonyl of glutamate residue (O4), in water/[BMIM]Br mixture at three different temperature value 27, 47 and 67 °C. Analysis of the normalized average dihedral angle of GSH (e) (O3-C4-N2-H11) and (f) (O4-C8-N3-H15), in water/[BMIM]Br mixture at three different temperature value 27, 47 and 67 °C.

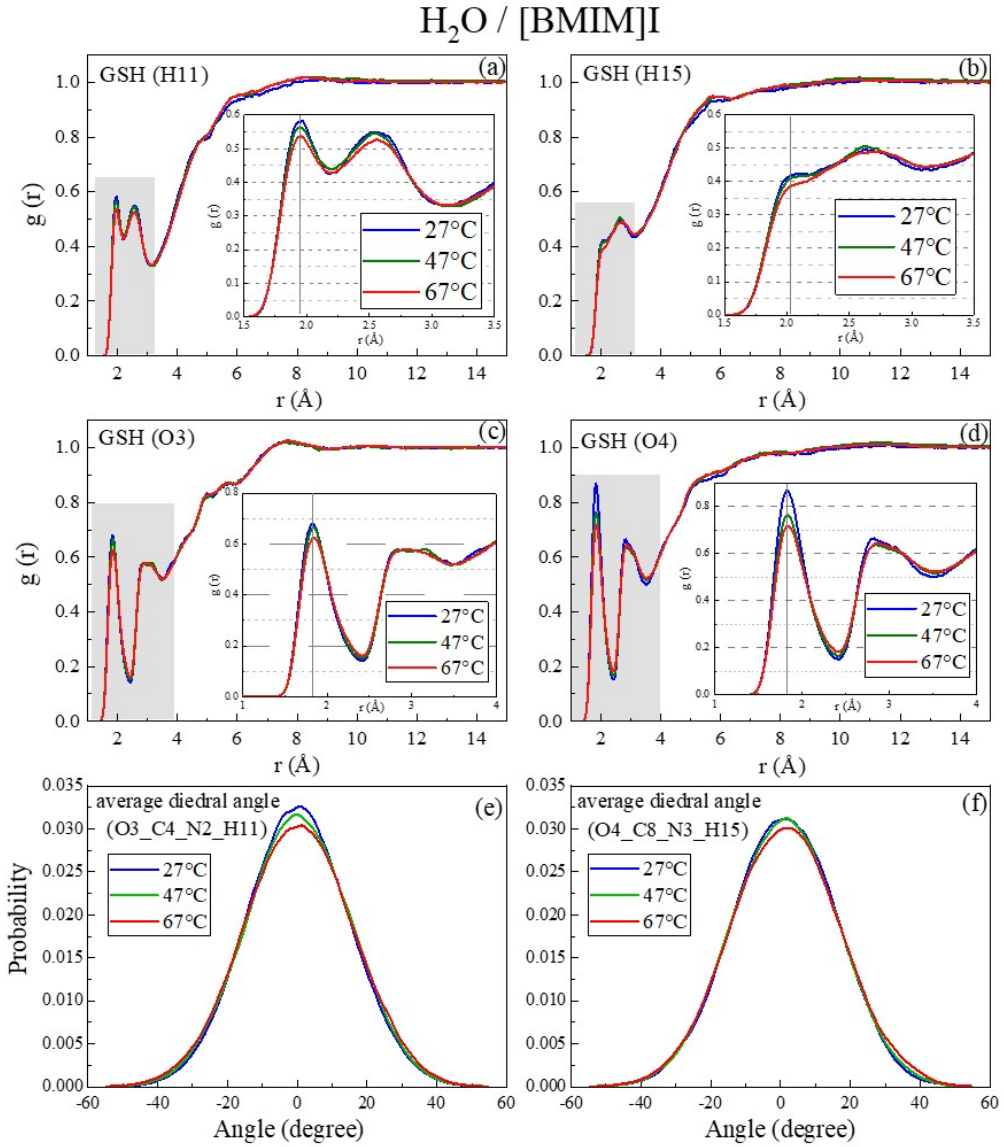

FIGURE 3.24: RDF of water molecules around the GSH (a) hydrogen of cysteine residue (H11), (b) hydrogen of glycine residue (H15), (c) amide carbonyl of glutamate residue (O3) and (d) amide carbonyl of glutamate residue (O4), in water/[BMIM]I mixture at three different temperature value 27, 47 and 67 °C. Analysis of the normalized average dihedral angle of GSH (e) (O3-C4-N2-H11) and (f) (O4-C8-N3-H15), in water/[BMIM]I mixture at three different temperature value 27, 47 and 67 °C.

Figures from 3.18 to 3.24 show that the temperature increases causes a slight decrease in the distribution of water molecules around the amide carbonyl groups, due to the thermal motion. Indeed, increasing of temperature causes the progressive weakening of the hydrogen bonds between water molecules and the amide carbonyl groups. Amide carbonyl groups show the same behavior in both pure water (figure 3.18) and in the binary solutions of salts (figures 3.19, 3.20 and 3.21) and different halogenic ILs (figures 3.22, 3.23 and 3.24).

This finding is in good agreement with experimental results i.e. a blue shift as a function of temperature of the AI signal. Panels (a) and (b) of the figures show the temperature effect on the N——H sites. In particular, panel (a) shows the RDF of water molecules around the hydrogen of cysteine residue (H11) and panel (b) that around the hydrogen of glycine residue (H15) of GSH. Increasing the temperature from 27 to 67 °C the number of water molecules around the hydrogen of both cysteine and glycine residues are reduced. Hence, the H-bond between GSH and water at N——H sites are weakened. These results support the experimental ones where weakening of the H-bond between GSH and water at the carbonyl and the amide sites decreases the length of C═O and N——H bonds, with a consequent lengthens of the C——N bond, causing a red shift of AII and $AIII_3$ signals. The same trend of amide bands shift and RDFs for all the investigated solvation environments is found.

As shown in the spectra of figure 3.17, at elevated temperature a signal in the 1480-1500 cm^{-1} spectral region appears. This band is assigned to the cis-AII mode as previously mentioned in the section 3.2.3. As suggested by Y. Wang et al. [101], the term cis-AII is used by analogy with the presence of the C——N stretching component, even though the N——H in-plane bending component is much smaller. Indeed cis-AII band have a large component of C——N stretching, which make its Raman cross section extraordinarily large as determined by its great increase intensity with temperature. The increased Raman cross section of cis-peptides derives from a large red shift of the $\pi - \pi^*$ electronic transition compared to that in the trans-peptides [109, 108, 112, 110]. The cis-AII signal have not any apparent frequency shift, while the trans-AII and $AIII_3$ bands shift down. The same frequency shift of the AII and $AIII_3$ signals is due to the weakened N——H $\cdots$ O hydrogen bonding at elevated temperatures, which decrease the frequency of the N——H in-plane bending component and thus lower the frequencies of AII and $AIII_3$ modes. Moreover, if the 1500 cm^{-1} band were dominated by C——N stretching with a low contribution of N——H in-plane bending, this would explain its modest frequency dependence upon temperature. Indeed, changes in hydrogen bonding with temperature are expected to affect primarily the N——H in-plane bend component [109, 108, 112].

Panels (e) and (f) of the figures from 3.18 to 3.24 show the normalized average dihedral angle of peptide bonds of GSH at different temperatures. According to MD results, temperature does not have a significant effect on the conformational changes of peptide bonds. The apparent discrepancy between the UV Raman experimental results and the MD simulation is

due to the resonance effect. In fact, to promote the trans-cis isomerization the combined temperature and resonance effects are needed. The UV radiation used as excitation wavelength together with the temperature increases, are able to lead to a cissoids form of GSH. An approach to measures the temperature dependence of the trans-cis population ratio is the uses of the cis-AII and trans-AII Raman bands intensities:

$$\frac{N_{cis}}{N_{trans}} = \frac{(\frac{I_{cis}}{\sigma_{cis}})}{(\frac{I_{trans}}{\sigma_{trans}})} = e^{-(\frac{\Delta G}{RT})} \tag{3.3}$$

Where I_{cis} and I_{trans} are the cis and the trans Raman bands intensities and σ_{cis} and σ_{trans} are the AII Raman cross sections of the cis and the trans conformers, R is the gas constant and T is the temperature.

Using the linearized formulation of the equation, it is possible to determine the Gibbs free energy difference between the ground states of the cis and the trans isomers by examining the temperature dependence of the relative cis-AII and trans-AII Raman bands intensities.

$$ln(\frac{I_{cis}}{I_{trans}}) = ln(\frac{\sigma_{cis}}{\sigma_{trans}}) - \frac{\Delta G}{RT} \tag{3.4}$$

The natural log of the ratio of the cis-AII and trans-AII intensities has been plotted against 1/T. The slope $(\Delta G/R)$ of the linear best fit gives the ΔG value [108, 112]. The resulting plot and the free energy values are shown in figure 3.25.

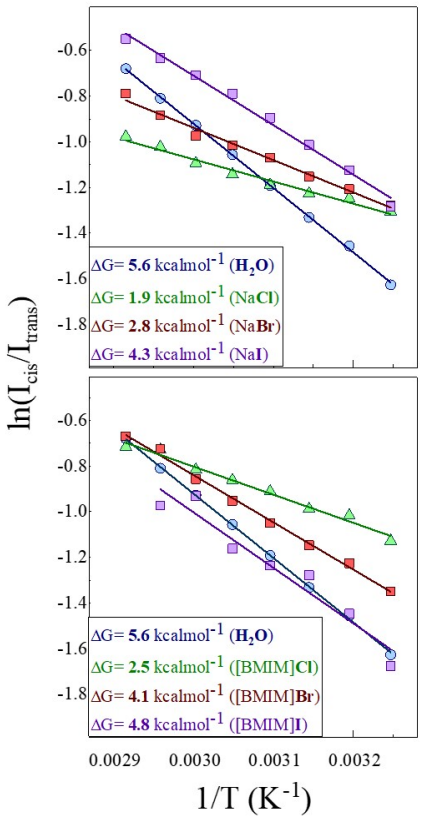

FIGURE 3.25: Natural log of the ratio of the cis-AII to the trans-AII band Raman intensities as functions of 1/T. The solid lines are the best linear least-square fit whose slope give the Gibbs free energy gap between the cis and trans amide forms.

The ions effects on the trans-cis isomerization are explained by the dehydration and hydration of the peptide link mainly induced by anion. Chloride and bromide anions stabilize the neutral resonance structure of the peptide link in the ground state, that is suppressed in the excited state, creating an impediment to rotate around the C —— N bond. The reduction in the trans-cis isomerization yield in presence of chloride and bromide anions compared to that in pure water is highlighted from the lower intensity of the cis-AII band in the Raman spectra of GSH in presence of Cl^- and Br^- than that of GSH in pure water. The estimated ΔG value with chloride and bromide is lower than in pure water, indicating a lower thermodynamic stability of the cis form when the peptide link is partially dehydrated by the anions presence. The GSH trans-cis isomerization yield in presence of iodide anion is higher than that of GSH in pure water; this is visible from the higher intensity of the cis-AII Raman band in the presence of I^- compared to that of GSH dissolved in pure water. Indeed the effect of iodide anion is to stabilize the dipolar resonance form of GSH in the ground state and suppress it in the excited one, allowing the rotation around the C —— N bond.

Chapter 4

Self-assembly of lysozyme in self-crowded conditions

Formation of amyloid aggregates has been subjected to a huge number of investigations due to their implication in relevant diseases [113, 114, 115, 116]. The capability of giving rise to amyloid fibrils is a general property of non-native proteins, and the high temperature represents a simple approach to induce their aggregation [117, 118, 119, 120]. The aggregation is generally an irreversible process [121], even if under native conditions the reversibility has been demonstrated [122]. As a model protein, lysozyme (LYS) received considerable attention due to its propensity to form in vitro amyloid fibrils [123], a preferential route to form them is the incubation of LYS at low pH and high temperature [114, 123, 124, 125, 126, 127, 128, 129], while at neutral or high pH amorphous aggregation is favored [130, 131, 132, 133]. The LYS self-assembly at low pH has deeply investigated, evidencing the formation of pathway-specific products [134, 135, 136]. Two distinct fibril growth pathways are identified: one at high ionic strengths involving the formation of oligomeric aggregates, and another at low ionic strengths in which single filaments grow up by addition of monomers [134, 135]. Both mechanisms are amyloidogenic and lead to structurally differentiable fibrils depending on the early stages of self-assembly [135]. The growth of rigid fibrils and globular oligomers follows independent mechanisms, and oligomers might transform in curvilinear fibrils or amorphous precipitates, but do not convert into stable rigid fibrils [137]. These latter preferentially form at low protein contents, while the globular oligomers become kinetically favored above a critical concentration and inhibit the growth of rigid fibrils [137]. Recently, globular oligomers have been highlighted as off-pathway competitors with rigid fibrils [138], that have been revealed the mainly responsible for cellular toxicity [116, 136, 137, 138], although the study of these species is inherently challenging due to their transient

character [116]. Networks of self-assembled amyloid fibrils constitute suitable biomaterials in different scientific fields [139, 140, 141, 142], despite they could also be formed within the intra- and extra-cellular medium, representing a possible mechanism of cell toxicity [143, 144]. Fibrillary gels are formed through complex multi-stage mechanisms strongly dependent on temperature, time, and protein type [117, 118, 119]. Exploiting its propensity to form fibrillary networks, LYS has been employed to create different functional biomaterials, as biocompatible hydrogels used as scaffold for cell cultures [145, 146, 147], as fibril networks with controllable morphologies [148] and as nontoxic microgels suitable for drug delivery [149]. Aggregation of globular protein is also of great interest in food technology. Indeed, the formation of aggregates with different morphologies and tunable gels network might represent a useful way to improve food properties and preservation [150, 151, 152, 153]. The majority of investigations connected to human diseases or functional materials, have considered the formation of amyloid fibrils at low protein concentrations within 1-4 wt.% [125, 134, 135, 144, 145, 146, 147, 148, 154, 155, 156]. In these conditions, the growth of amyloid fibrils takes place at temporal scales of days, and usually occurs through hydrolytic processes [148, 155, 156]. Relatively less efforts have been devoted to the study of LYS unfolding and aggregation in highly concentrated samples, with protein content larger than 10 wt.% (100 mg/ml) [157, 158, 159, 160, 161, 162]. Nevertheless, understanding the behavior of crowded protein samples is of relevance in cellular biology, industrial and pharmaceutical fields [157, 163, 164, 165, 166, 167, 168]. A broad range of pharmaceutical applications, require formulations with protein concentrations higher than 100 mg/ml, and issues caused by the high viscosity and protein aggregation have been evidenced [160, 163, 164], needing the development of methods for monitoring in situ concentrated protein samples [160, 163, 169]. Studying protein solutions in crowding conditions is also mandatory to explain their behavior within the cellular environment [165, 166, 168], where the total macromolecules concentration is higher than 400 mg/ml [168, 170]. In these macromolecular crowding conditions, excluded volume and viscosity are considered relevant factors in determining protein aggregation features, such as the acceleration of α-synuclein fibrillation [170]. These factors act even for protein self-crowding [171, 172], affecting the stability of the native protein [173] and its aggregation due to thermodynamic and kinetic effects. Significant changes of hydration properties, attributed to protein clustering [174], are expected to occur for LYS solutions with concentrations larger than 100 mg/ml [175, 176, 177]. The melting temperature of LYS is found to significantly increase with concentration in diluted regimes (up to

15 mg/ml) because of excluded volume effects [178]. Instead, at high protein concentration, even if going from 2.5 to 300 mg/ml no changes of the secondary structure is evidenced [158], a thermal destabilization, attributed to an enthalpic effect induced by protein-protein interactions, is revealed [159, 162]. Based on the informations mentioned above, deeper investigations of the amyloid-like association in self-crowded conditions, might reveal novel important insights in several areas, including cellular biology, biotechnology and food sciences. In this work, highly concentrated (18 wt.%) LYS aqueous solutions in acidic conditions have been prepared. The in situ investigation of the thermal aggregation, is made by means of Fourier-transform infrared (FTIR) spectroscopy, able to follows the development of amyloid-like cross β-sheet structures [145, 146, 147, 179]. Protocols are selected leading to the formation of protein hydrogels in reduced temporal scales (few hours), such that the whole process can be monitored. Different protein hydrogels, whose properties can be modulated by changing the curing temperature, are obtained. New molecular insights on self-assembly are related to the results of small angle scattering (SAS), differential scanning calorimetry (DSC), rheological and transient grating experiments, giving a consistent picture of the molecular phenomena responsible for the macroscopic properties of the system. The SAS data are preliminary results. In this thesis are only reported the scattering curves without the application of a model, and the data are discussed qualitatively. However, a consistency with all the results obtained with the other experimental techniques is evidenced. An interesting outcome of this work is the possibility of forming hydrogels constituted by amyloid oligomers instead of fibril structures, as instead is commonly reported in literature [180].

4.1 Experimental methods

4.1.1 Solutions preparation

The lyophilized powder of hen egg-white lysozyme (Sigma Aldrich, L6876) is dissolved without further purification in deuterium oxide (99.9 atom % D, Sigma Aldrich) to obtain solutions with concentrations of 60, 120 and 240 of mg of solute/ml of solvent (here referred as mg/ml), corresponding to 5, 10 and 18 wt.%, and denoted as LYS60, LYS120, LYS240, respectively. The sample is left overnight to ensure total protein dissolution. The pD is then adjusted to 1.8, adding small amounts of 2M deuterium chloride (DCl) to reach a pH meter reading of 1.4; as usually done, since deuterated water is employed, 0.4 units should be added to the pH meter reading.

4.1.2 HD-TG experiments

A single 1064 nm laser beam is divided in two pulses, which interfere and produce into the sample an impulsive spatial modulation of the material optical properties, characterized by the wave vector q. The temporal evolution of the induced modulation is probed through a 532 nm third beam. The angle between the exciting beams and consequently the q-vector induced in the sample, are changed using different spacing of the grooves of the phase mask. In this thesis q-vector value of 2.1 μm^{-1} has been used. The grating diffracts the beams, passes through a doublet of achromatic lenses, and the second lens of the achromatic doublet recombined and focused the beams on the sample, reproducing the same spatial modulation of the phase mask. A reference beam is used to produce the heterodyne detection. The HD-TG signal is optically filtered and measured by a photodiode with a bandwidth of 1 GHz. The signal is then amplified and recorded by a digital oscilloscope with a 7 GHz bandwidth. We record the data using a fast time window (0-80 ns range with a 50 ps time step of sampling) and a long one (0-2 μs range with 800 ps time step). The measurements are merged in a single data file. Each signal are the average of 1000 records, producing an excellent signal to noise ratio. The samples are kept directly in the cuvette, introduced in a copper cell holder, connected to a thermostat and a thermocouple to feedback the temperature control. The temperature is varied from 20 to 80 °C. More information on HD-TG experiment and on the origin of the TG signal are provided in section 2.2 of chapter 2.

4.1.3 FTIR spectra

Infrared absorption measurements are collected using a FTIR Bruker spectrometer model Tensor27, equipped with a DTGS detector. The Opus 5.5 Bruker Optics software allowed the acquisition and the analysis of spectra. Transmission spectra are obtained employing a home-made cell equipped with CaF2 windows; the cell is positioned into a jacket whose temperature is controlled by circulating water through a Haake F6 thermostat. To monitor visually macroscopic changes, parallel thermal treatments are performed on sample aliquots placed into standard cuvettes. The spectra are acquired with a resolution of 2 cm^{-1} by averaging over 20 scans for each spectrum. To track the temperature and time dependence of the amide I peak position located at 1650 cm^{-1}, the center of gravity of the band is determined at 20 % from the maximum intensity with the corresponding Opus 5.5. routine.

4.1.4 CD spectra

Circular dichroism spectroscopy is performed using a CD spectrometer (JASCO, Easton MD, US) equipped with a CD-426S/426L Peltier cell. Protein samples in D_2O are placed in a Hellma quartz glass high-performance cuvette with a 1 cm path length and a magnetic stirrer bar. CD spectra are obtained in the range from 190 to 260 nm at a scanning rate of 50 nm/min averaging 10 accumulations with a data pitch of 0.2 nm, D.I.T of 4 sec, bandwidth of 1 nm and a standard sensitivity.

4.1.5 Micro-DSC thermograms

Micro-calorimetry analyses are performed using a microDSC III (Setaram, France). Firstly, 0.750 g of LYS dispersion at the three different concentrations (60, 120 and 240 mg/ml) are loaded inside a Hallostey calorimetric cell and analyzed using the following thermal program: isotherm at 20 °C for 20 min followed by a consecutive heating and cooling ramp from 20 to 80°C at 1°C/min. The same thermal program is used also to analyze the LYS gel, formed through the thermal treatment involving curing at 50 °C, as described below. The temperature and the enthalpy are calculated from the peak and the area of the transition, using the tangent method.

4.1.6 Rheologcal experiments

Viscoelastic properties of the LYS gel matrix is studied using a rotational rheometer (Kinexus, Malvern) equipped with a 20 mm plate geometry at a gap of 1 mm. The frequency sweep tests are performed at a shear stress of 0.5 Pa in the frequency range 0.01-10 Hz at temperatures of 15, 25, 35 and 50°C. The temperature sweep test is conducted at a frequency of 1 Hz and a stress of 0.5 Pa between 15 and 70°C at a rate of 1°C/min. The time sweep test at 0.5 Pa and 1 Hz at two temperatures (50 and 25°C) for 20 min, is made and repeated for both temperatures two times consecutively.

4.1.7 SAXS measurements

SAXS measurements are performed on a Bruker AXS Micro instrument during the period abroad at the ETH of Zurich in the laboratory of Food and Soft Materials of professor Raffaele Mezzenga. The source is a microfocused X-ray operating at voltage and filament current of 50 kV and 1000 μA, respectively. The Cu Kα radiation (λCu Kα= 1.5418 Å) is collimated by a 2D Kratky-collimator, and the data are collected by a 2D Pilatus 100 K detector. The scattering vector $q = (4\pi/\lambda)sin\theta$, with 2θ is the scattering angle, calibrated using silver behenate. Data are collected and azimuthally averaged using the Saxsgui software to yield onedimensional intensity versus scattering vector q, with a q range from 0.004 to 0.5 Å^{-1}. All the samples are filled into 2 mm diameter quartz capillaries which are sealed with epoxy glue (UHU). Measurements are performed as a function of temperature and the scattered intensity is collected between 2 or 6 h, depending on the sample concentration.

4.1.8 SANS measurements

SANS experiments are carried out using the *Yellow Submarine* diffractometer operating at the Budapest Neutron Center. Samples are placed in 1 mm-thick quartz cells. Temperature is controlled within 0.1 K using a Julabo FP50 water circulation thermostat. The range of scattering vectors q is set to 0.038-0.38 Å^{-1}. The q value is defined as $q = (4\pi/\lambda)sin\theta$, where 2θ is the scattering angle. In order to have access to the whole range of q, two different configurations are used. In particular, the sample-detector distance is set to 5.125 m from the sample and the incident neutron wavelengths are 4.4 and 10.23 Å, for medium and low q range respectively. The raw data have been corrected for sample transmission, scattering from empty cell, and room background.

4.2 Results and discussion

4.2.1 Concentration effect on LYS structure

Figure 4.1 (a) shows the X-ray scattering intensity, I, as a function of the scattering vector, q , of a range of LYS concentrations at pH= 1.8 and 20°C.

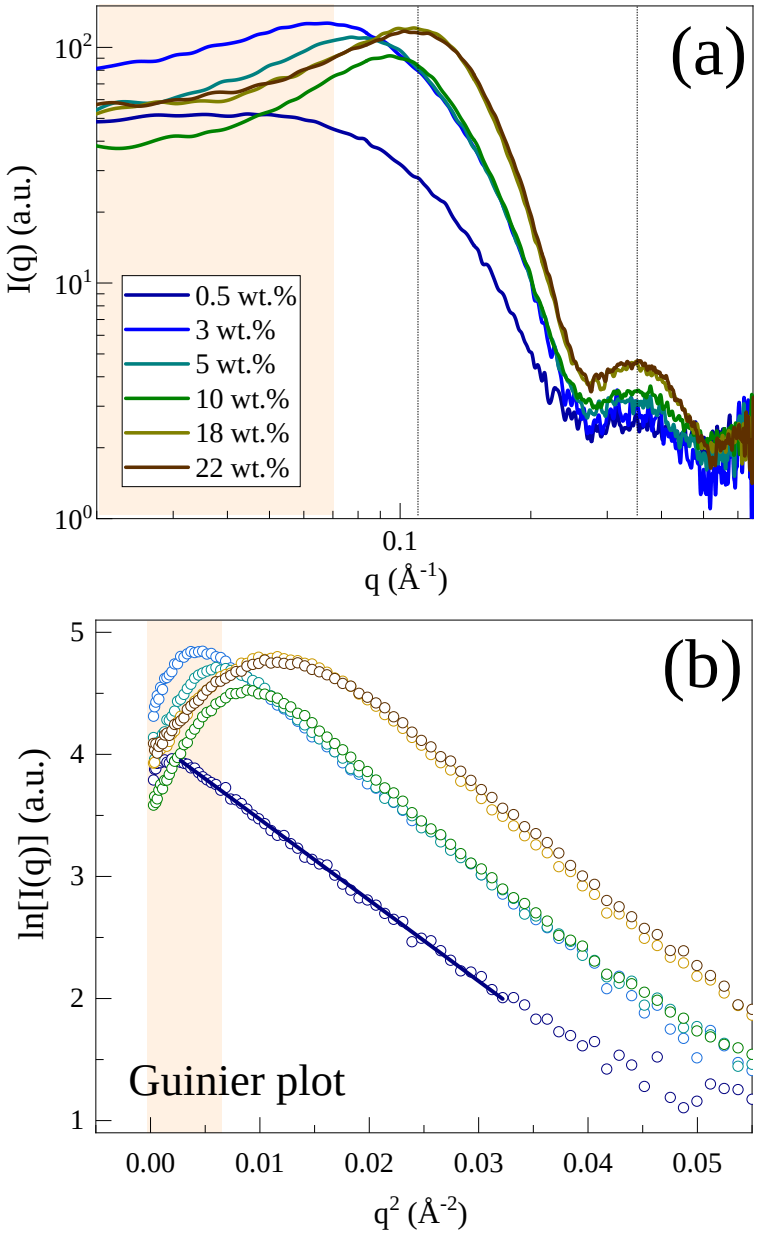

FIGURE 4.1: (a) concentration dependence of the experimental scattering curve I(q) at 20°C, of LYS in D_2O at pH 1.8. The protein concentration was varied from 0.5 to 22 wt.%. (b) Guinier plot to highlight the linear dependence of ln[I(q)] versus q^2 at low q values.

At LYS concentration of 0.5 wt.%, the scattering intensity forms a plateau up to 0.07 Å^{-1}.

Such plateau is characteristic of dilute protein monomers, when they are monodispersed and homogeneously distributed in the solution. In this case, the inter-particle distances remain higher than the intra-particle ones, and the measured scattering curve corresponds to the form factor if S(q)= 1, a brief mention to the SAXS and SANS techniques is provided in the appendix 6.1. Increasing the protein concentration from 3 to 22 wt.%, a broad hump characterizes the shape of the structure in reciprocal space. Inter-particle distance correlations due to charge repulsion give rise to a non unity S(q) that suppresses the lowest angle scattering. Indeed, the descent in intensity at small q-values indicates a repulsive interaction potentials between protein monomers [181, 182]. In concentrated systems, the particles are densely packed, and the distances relative to each other became of the same order of magnitude as the distances inside the particles. In this case, the scattering curve also contains contributions coming from neighbouring proteins. Therefore, for concentrated samples, the experimental scattering curve contains both contributions: the form and structure factors. The high used concentrated solutions enable to obtain high-statistic scattering data in a wide q range, allowing getting internal structural information of the proteins in the real space. Figure 4.1 (b) shows the Guinier plot of the experimental scattering curves [183]. It is possible to notice that in the q^2 interval 0.01-0.05 $Å^{-2}$, the data points of the diluted LYS 0.5 wt. % solution fall onto a straight line.

The q range 0.1-0.2 $Å^{-1}$ in figure 4.1 (a) reflects the tertiary structure of LYS in the real space distance of about 3 nm, such as molecular shape and dimensions, while the scattering curve in the q range of 0.3-0.6 $Å^{-1}$ mostly reflects the intramolecular structure in the real space distance of 1 nm, such as structural domain correlation and polypeptide arrangement [184, 185]. The SAXS data highlight that, as a function of protein concentration, a progressive shift at high q value of the low-q peak occurs, probably related to the excluded volume effect with a greater proximity between the proteins and therefore lower correlation distances.

4.2.2 Thermal unfolding of dilute LYS solution

Figure 4.2 shows the temperature dependence of the X-ray scattering curves I(q) of the diluted (0.5 wt.%) LYS solution, where the temperature is varied starting from 20 until 80°C, each 20°C. After the thermal ramp, the sample is cooled again to 20°C, and the scattering curve is acquired to test the effective thermal reversibility of protein structure.

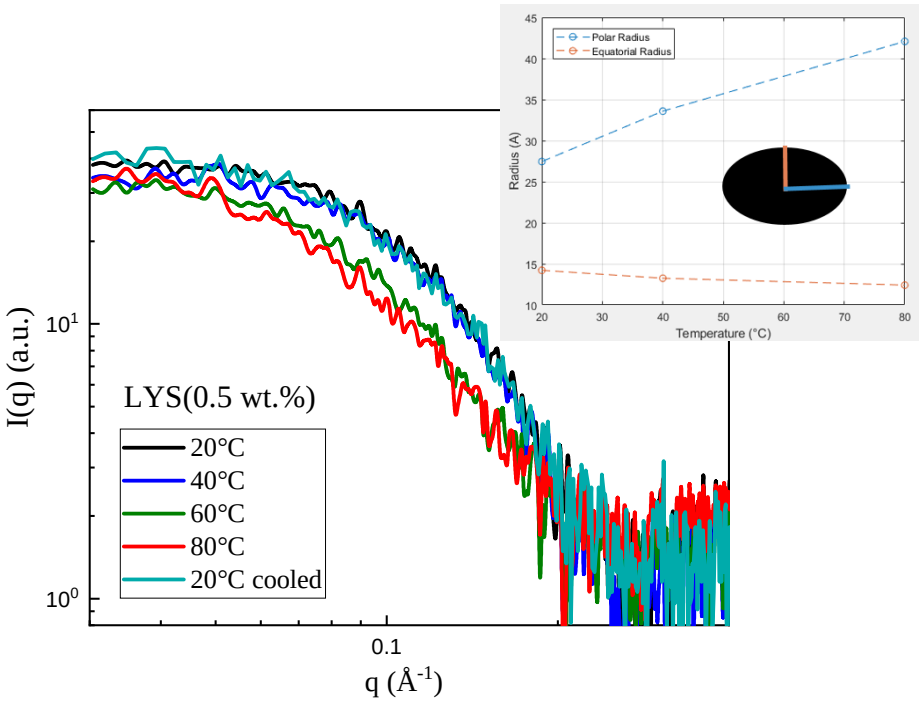

FIGURE 4.2: temperature dependence of the experimental scattering curve I(q), of a diluted 0.5 wt.% LYS solution at pH 1.8. The temperature was varied from 20 to 80°C.

Figure 4.2 shows that with elevating temperature the greatest variation of the scattering curve in the middle q range occurs between 40 and 60°C, suggesting that the thermal denaturation of LYS occurs in between [184, 185]. The radii values of LYS are obtained from the SAXS curves fitting, assuming an ellipsoidal shape of the LYS globular protein. The polar and the equatorial radii trends as a function of temperature are reported in the inset of figure 4.2 evidencing that the polar radius slightly increases with increasing temperature, while the equatorial radius value remains constant. The outcome highlights that LYS seems to have a preferred direction of unfolding in the used experimental conditions. In addition, a high thermal reversibility of the LYS structure is demonstrated. Indeed, in figure 4.2, the scattering curves collected at 20°C, before (black curve) and after (cyan curve) the thermal treatment, are perfectly superimposed. This suggests that even at low pH and after a drastic

heat treatment, LYS protein maintains a high structural reversibility. The outcomes is supported by previous literature finding on a similar system [184, 186].

To supplement the SAXS data, circular dichroism spectra of a very dilute solution of LYS are recorded as a function of temperature, the data are shown in the figure 4.3,

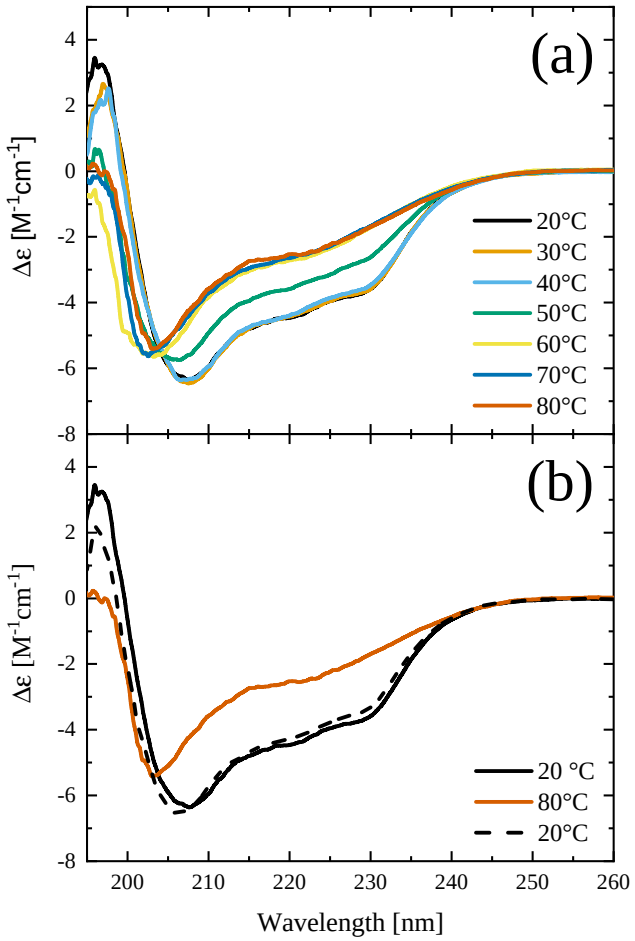

FIGURE 4.3: Circular dichroism spectra as a function of temperature of a LYS solution at pH 1.8. The top panel shows the heating thermal ramp from 20 to 80°C. The bottom panel shows the comparison between the spectra at 20°C performed before (black line) and after (green line) the thermal ramp.

The CD spectra show the typical features of LYS, a mixture of β-sheet and α-helix with the former dominating, similar to published data [154]. The negative peaks at 208 nm and 222 nm are attributed to the helical features, whereas the shoulder around 218 nm is reflecting the β-sheet components. By following the behaviour of these peaks as a function of temperature, it is possible to monitor changes in secondary structure qualitatively [187]. The influence of temperature on the spectra is shown in panel (a) at an interval of 10°C. The spectra between 20°C and 40°C coincide with the folded one. The most drastic change of the secondary structure of LYS, in the used experimental conditions, occurs between 40°C

and 60°C. The decrease and shift of the peak at 208 nm and the decrease in the shoulder at 222 nm are indicating a change from helical features to β-sheet components and random coil [154, 187]. Panel (b) shows the comparison between the CD spectra collected at 20°C before and after the thermal treatment. The solid and dotted black spectra indicate an almost full reversibility of protein secondary structure. Additionally, a isodichroic point at 204 nm was observed indicating a two-state cooperative unfolding process [188].

4.2.3 Thermal unfolding of LYS in self-crowded conditions

The thermal unfolding of LYS120 in self-crowded condition it has been characterized by different techniques. The spectroscopic bands of interest are Amide I (AI) and Amide II (AII), which are generated by different vibrational modes (see chapter 3). Amide I band is mainly due to C$=$O stretching, and depending on the involvement of the carbonyl groups in the formation of the different secondary structures of protein, the C$=$O groups vibrate at slightly different frequency. Following the evolution of the AI band as a function of temperature means following the development of the protein secondary structure. Figure 4.4 shows the FTIR spectra recorded from 25 to 87 °C of LYS120 solution.

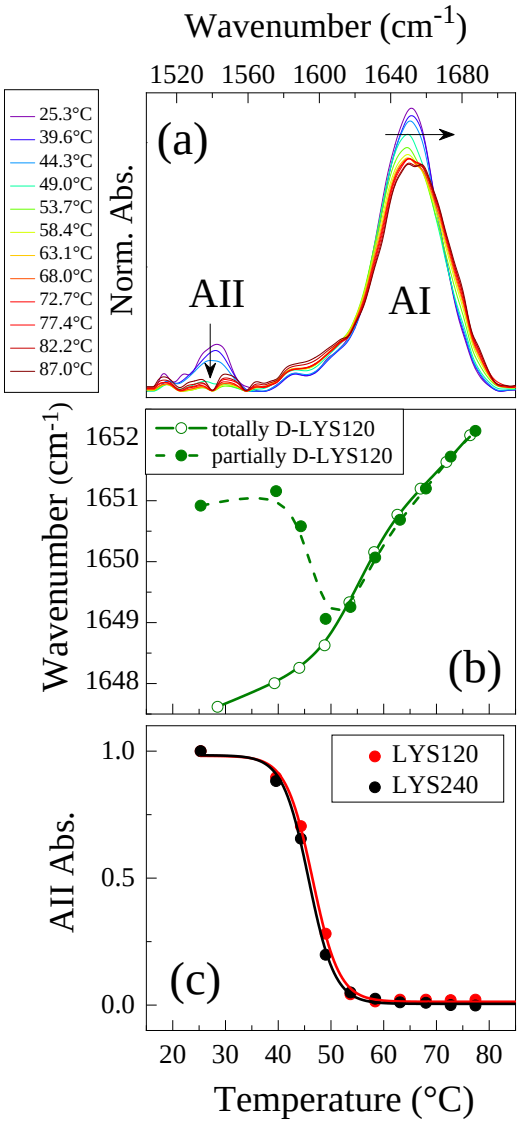

FIGURE 4.4: (a) FTIR spectra of the LYS120 solution recorded as a function of temperature in the amides spectral region. (b) AI frequency shift of the partially and the totally deuterated LYS120 samples. (c) AII absorbance of partially deuterated LYS samples determined at different temperatures: LYS 120 (red curve) and LYS240 (black curve) solutions.

The temperature dependence of the AI peak position is reported in figure 1b (green full circles): the band shifts to lower wavenumbers in the range 40-50 °C then progressively moves to higher wavenumbers. The observed red-shift is caused by the H/D exchange between the D_2O solvent and amide hydrogens localized in the core of the folded structure [189, 190]; this is also indicated by the parallel decrease of the AII band, which is mainly ascribed to a N——H bending vibration. The full H/D exchange is reached at Tex 50 °C (figure 4.4 c), a few degrees below the melting temperature T_m= 53 °C (see hereafter), as also observed in other cases [179, 189, 191]. This fact is related either to a change of the tertiary structure that precedes the global unfolding, giving rise to an intermediate with a native-like secondary structure, or to conformational changes of more local and transient character [179, 191]. The LYS behavior in self-crowded condition can be simply explained considering a cooperative two-state process, involving folded (F) and unfolded (U) species in thermal equilibrium [179, 189], as previously observed for the dilute LYS solution, from the CD data. In fact, if the exchange of internal N——H groups becomes fast enough in the U state, as expected, even the presence of a small fraction of U at $T < T_m$ will cause the rapid exchange of the total amount of protein in the sample. In these conditions, the signal depletion rate is expected to depend directly on the fraction of U species [192, 193, 194, 195]. The temperature dependence of the AI peak position, in the LYS120 sample totally exchanged after one-hour incubation at 50 °C, is reported in figure 4.4 b (green empty circles). The data follow a pseudo-sigmoidal functional form, evidencing a melting region at around 50-60 °C and both pre- and post-melting linear domains; for $T > T_{ex}$ the curves obtained with or without the pre-treatment recover. The unfolding process can be described by a two-state model, based on the equilibrium between folded (F) and unfolded (U) species [196, 197]. The spectroscopic observable y_T (band position or signal intensity) can be expressed as the sum of its value in the folded and in the unfolded states weighted for their corresponding population. Considering a linear temperature dependence of the observable within each of the states leads to the following expression:

$$y_T = \frac{y_F + m_F \cdot T + (y_U + m_U \cdot T) \cdot K_T}{1 + K_T} \tag{4.1}$$

K_T is the equilibrium constant at a given temperature, y_F and y_U are the values of the observable when the proteins are respectively in the folded and in the unfolded state at T= 0 K, m_F and m_U describe their temperature dependence in pre and post-melting region. The

equilibrium constant can be written as a function of the unfolding enthalpy (ΔH_{F-U}) and of the melting temperature (T_m):

$$ln(K_T) = \frac{\Delta H_{F-U}}{R} \cdot (\frac{1}{T_m} - \frac{1}{T}) \tag{4.2}$$

R is the gas constant. From the two relationships, the following one can be obtained:

$$y_T = \frac{y_F + m_F \cdot T + (y_U + m_U \cdot T) \cdot e^{\frac{\Delta H_{F-U}}{R} \cdot (\frac{1}{T_m} - \frac{1}{T})}}{1 + e^{\frac{\Delta H_{F-U}}{R} \cdot (\frac{1}{T_m} - \frac{1}{T})}} \tag{4.3}$$

This functional form was employed to reproduce the melting curves. Similar melting curves are previously observed for LYS solutions containing denaturing cosolvents (ethanol and DMSO) and are modelled based on a classical two-state picture, with a rather continuous thermal restructuring within the F and U states themselves [189, 196, 198]. Based on such a model, thermodynamic parameters are extracted at different pH values as shown in figure 4.5.

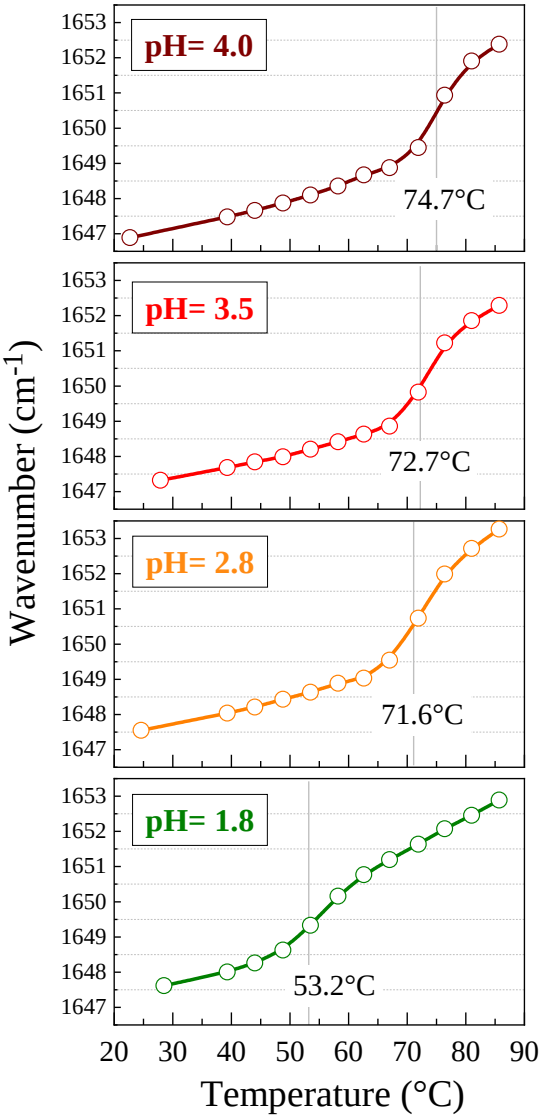

FIGURE 4.5: AI frequency shift of LYS solutions at different pH, as a function of temperature.

pH	T_m(°C)	ΔH_{F-U} (kcalmol^{-1})
4.0	74.7 ± 0.9	113 ± 20
3.5	72.7 ± 0.5	116 ± 15
2.8	71.6 ± 0.6	85 ± 8
1.8	53.2 ± 0.3	67 ± 4

TABLE 4.1: Thermodynamic parameters obtained by reproducing the experimental data (AI peak position) with the two-state model function.

Going from pH= 4.0 to 2.8 only leads to minor changes on T_m, from 75 to 72 °C, in line with other FTIR studies [157]. Relevant effects are instead observed at pH= 1.8, when both

the Tm and enthalpy change (ΔH_{F-U}) decrease down to 53 °C and about 70 kcal/mol, respectively. These results are reasonably consistent with those obtained for more diluted solutions using different approaches [154, 160, 178]. The T_m and ΔH_{F-U} obtained at pH= 1.8 are practically coincident with those (T_m= 51 °C and ΔH_{F-U} 70 kcal/mol) previously obtained for a LYS solution (120 mg/ml; pH= 3.0) in presence of ethanol (18 % mole fraction); yet, in that case, the development of a large amount of ordered β-sheet aggregates is observed in the 30-64 °C range [196] and rapid gelation at the macroscopic level [199]. Thus, even if at any given T the fraction of U species, prone to aggregation, must be similar in the two environments, the self-assembly is strongly suppressed at pH= 1.8. This can be mainly ascribed to the effect of coulombic repulsive interactions among heavily charged proteins (a net protein charge of 17-18 is predicted at the working pH) [200]; the role of ethanol in favoring aggregation might be also taken into account.

From a methodological point of view, we notice that the estimated T_{ex} is 3 °C lower than T_m, similarly to what found for LYS in other solvent conditions [189]; this indicates that T_{ex} is a reasonable approximation of the melting temperature T_m, as long as comparable FTIR acquisition procedures are considered.

Figure 4.6 shows the SAXS curves of the concentrated LYS120 solution as a function of temperature. The temperature variation of the scattering curve reflects the evolution of the LYS structure due to the unfolding process.

In this concentration regime I(q) is the results of both, P(q) and S(q) contribution, as explained in the appendix 6.1, and the statistics of the scattering data is high enough to make it possible to obtain information about the correlation between internal structures of LYS monomers, which will be the subject of future investigations.

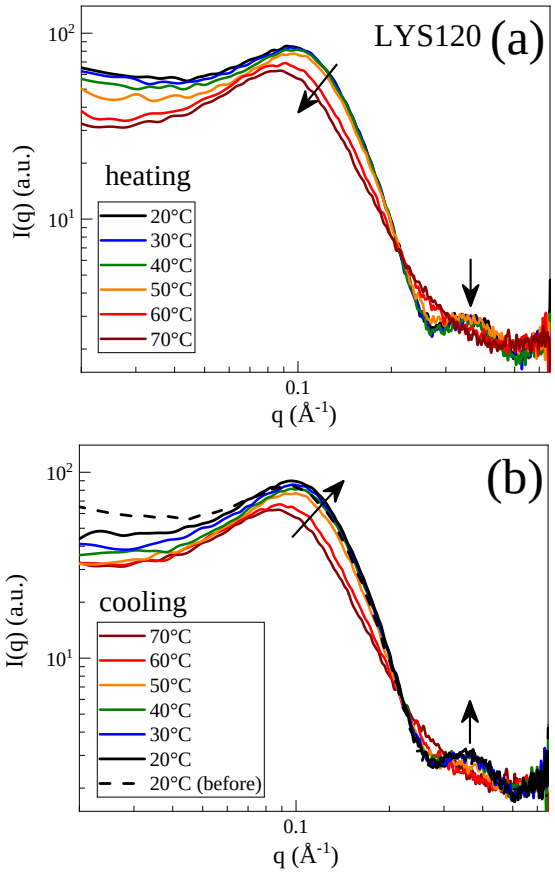

FIGURE 4.6: Experimental scattering curve I(q), of LYS120 solution at pH 1.8, as a function of temperature. (a) shows the heating treatment from 20 to 80°C. (b) shows the cooling ramp from 80 to 20°C.

Depending on the investigated q range, the scattering curve contains different structural information of proteins. The low q region gives information on the spatial correlation between monomers. The middle q region reflects the spatial arrangement of the polypeptide chain that provides protein's shape and size. The high q region reflects the spatial correlation between different chain domains, i.e. the intramolecular arrangement of the protein chain [184, 185, 186]. As shown from figure 4.6 (a) the middle q region (0.1-0.2 $Å^{-1}$) is characterized by a broad hump [184, 186], which remains unaltered until 40°C. This suggests that no significant structural variations of the protein occur in this temperature range. At 50°C the scattering curve move towards lower wave vectors, indicating that the globular shape of protein starts to unroll. In agreement with FTIR data, the major conformational variation occurs between 50 and 60°C, and the shape of LYS becomes more elongated. At 80°C the persistence of the broad peak highlights that, even at the highest temperature, LYS monomers continue to have a certain compactness. In the q range between 0.3-0.5 $Å^{-1}$ there

is another hump in the scattering profile [184, 186] which remains unchanged in shape and position until 50°C, and disappears at 60°C.

The SAXS data suggest that the greatest LYS structural variation occurs between 50 and 60°C. The almost negligible variations at low temperatures of the scattering curves are related to the flexibility of the protein chain, which allow some little conformational rearrangements. Even the SAXS outcomes confirm the possibility to describe the LYS unfolding process with two state model (folded $\longleftrightarrow$ unfolded) also in the high concentrated regime. Figure 4.6 (b) shows the SAXS curves during the cooling thermal treatment. The scattering profiles at 20°C before and after the heat treatment are similar in the middle/high q regions. This result highlight a good reversibility of the protein structure, even in self-crowded condition.

The structural changes of proteins in solution have a strong influence also on the interactions occurring between the macromolecules and the surrounding hydration water molecules. Indeed these changes could have a strong impact on the system viscoelastic behaviour. This latter is characterized by both the bulk and the shear moduli, and strongly influence the propagation of acoustic waves into the soft media [201]. The protein molecular composition mainly affect the bulk properties of the system, while its space organization has influence on the shear properties. The chemical and physical interaction between proteins and water molecules leads to relevant modification of the acoustic waves propagation [202]. Figure 4.7 reports the temperature dependence of the acoustic parameters of self-crowded LYS120 solution. In particular panel (a) shows the acoustic wave sound velocity C_S, and panel (b) the acoustic wave damping rate Γ_A. The function used to fit the HD-TG signal and to obtained the acoustic parameters, is expressed in chapter 2 in subsection 2.2.4.

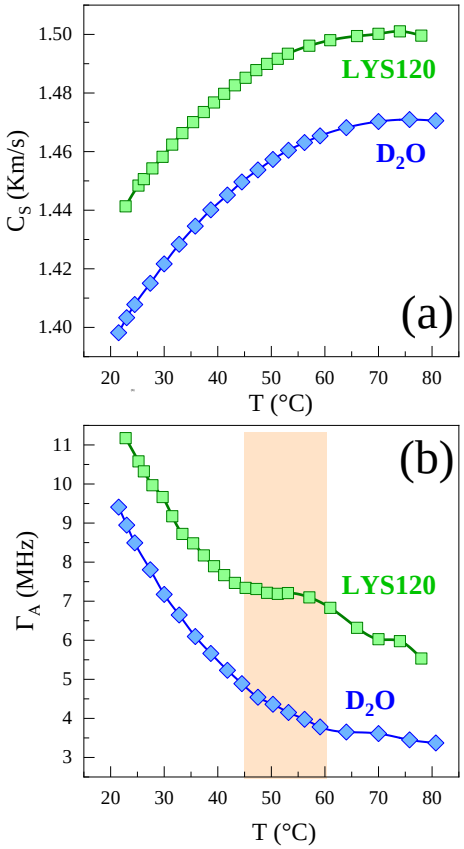

FIGURE 4.7: temperature dependence of self-crowded (9.8 *wt.*%) LYS solution: (a) sound velocity C_S, (b) damping rate Γ_A.

According to the elastic theory the absolute value of C_S is higher in the protein solution than in pure solvent, due to the higher density of the polymer solution. Instead the trend of C_S as a function of temperature retraces that of the pure solvent (D_2O). In particular C_S strongly increased with temperature until 50°C, less rapidly until 75 °C, and decreased after 75°C, as shown by the blue curve in figure 4.7 (a) and in previous experimental works on D_2O [166] and H_2O.

The temperature dependence of the acoustic wave damping rate Γ_A, shows a linear decrease until 45°C, like the thermal behaviour of a pure liquid [203]. In the range 45-60 °C, the acoustic wave damping rate remains constant, this behaviour is connected to the transition of protein from the folded structural conformation to the unfolded one [204, 161]. A compensation effect on the viscosity could occurs. On one hand the thermal motion that breaks the hydrogen bonds between water molecules, leads a viscosity decrease. On the other side the increases of temperature unfold the protein globule, inducing an exposition of the hydrophobic part. This process lead to a variation of the hydration shell, that could

increases the system viscosity [204, 205, 206]. The overall effect is the stationary value of the acoustic wave damping rate during unfolding. After 60°C the Γ_A trend recover the expected behaviour of the pure solvent.

4.2.4 Amyloid aggregation of LYS in self-crowded conditions

The same analysis previously performed for the LYS120 solution is conducted for the LYS240 sample. The corresponding thermal evolution of the AI and AII bands is shown in figure 4.8.

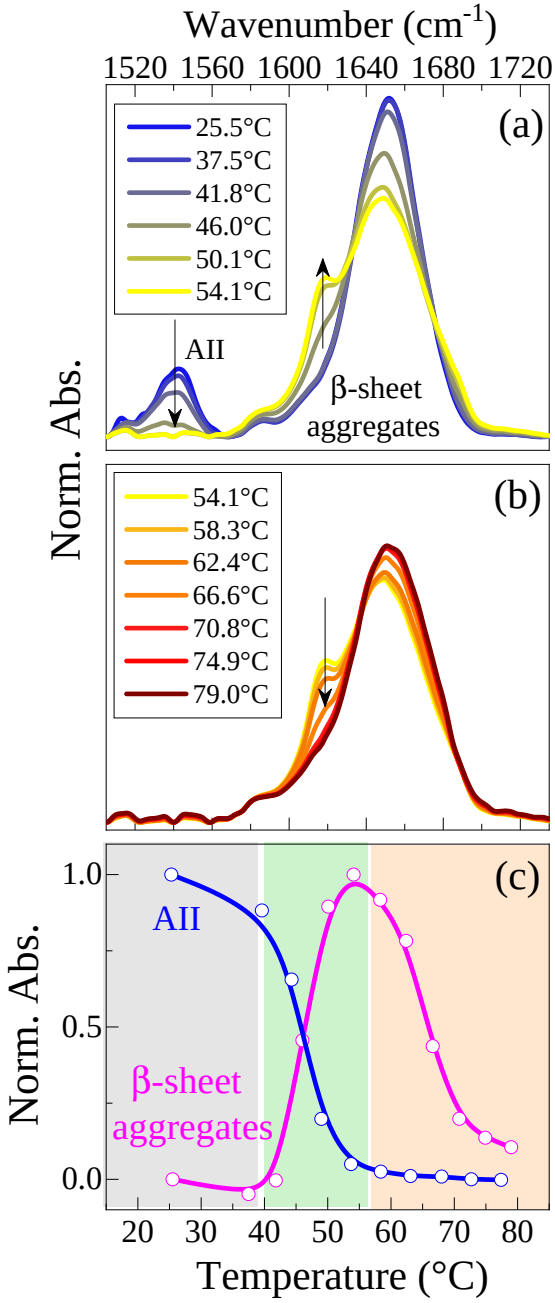

FIGURE 4.8: FTIR spectra in the amides spectral region obtained for LYS240 in two temperature ranges: (a) from 25.5 to 54.1 °C and (b) from 54.1 to 79.0 °C. Panel (c) shows the temperature dependence of the aggregate signal absorbance at 1618 cm^{-1} together with the AII absorbance depletion resulting from the depicted spectra in panels a and b.

In this crowded sample, within the range 30-55 °C, the protein self-association is found to occur, as testified by the increase of the two spectral components peaked at 1618 and 1690 cm^{-1}, typical for inter-protein antiparallel β-sheet [145, 146, 155, 179]. Following previous interpretations [196, 198, 207], β-sheet oligomers, rather than amyloid fibril, are expected to be formed in the actual conditions. This seems also to agree with the mechanism of amyloid growth proposed by Hill et al. [125], in more diluted conditions. In this case, LYS oligomers are found to develop soon at 50 °C without nucleation barrier, during the lag phase that precedes the protofibril nucleation step. This is also consistent with the conclusions of Zou et al. [155] who specifically attributed the two spectral components at around 1618 and 1690 cm^{-1} to antiparallel β-sheet configurations of LYS oligomers; whereas, parallel β-sheet arrangements, should characterize amyloid fibrils that form after long incubation periods (tens of hours) at higher temperatures (62 °C) [155].

Because of the occurrence of aggregation, it is challenging to monitor the unfolding process in this concentrated sample using the AI signal. On the other hand, we can easily follow the intensity decrease of the AII band at 1540 cm^{-1} due to the H/D exchange. As previously mentioned , the overall exchanging rate depends on the fraction of U species, thereby the intensity reduction of the AII band can be related to the position of the F $\leftrightarrow$ U equilibrium [189, 192, 193, 194, 195]. Figure 4.4 c shows similar depletion trends for the two LYS120 and LYS240 samples, leading to the same exchange temperature (T_{ex} 50 °C). This suggests that, at high concentrations, the melting process is basically independent on the protein content, even when strong self-association occurs. An analysis of the exchange kinetic at 45 and 50 °C further supports the notion that the F $\leftrightarrow$ U equilibrium is not affected by the protein content and amyloid self-assembly.

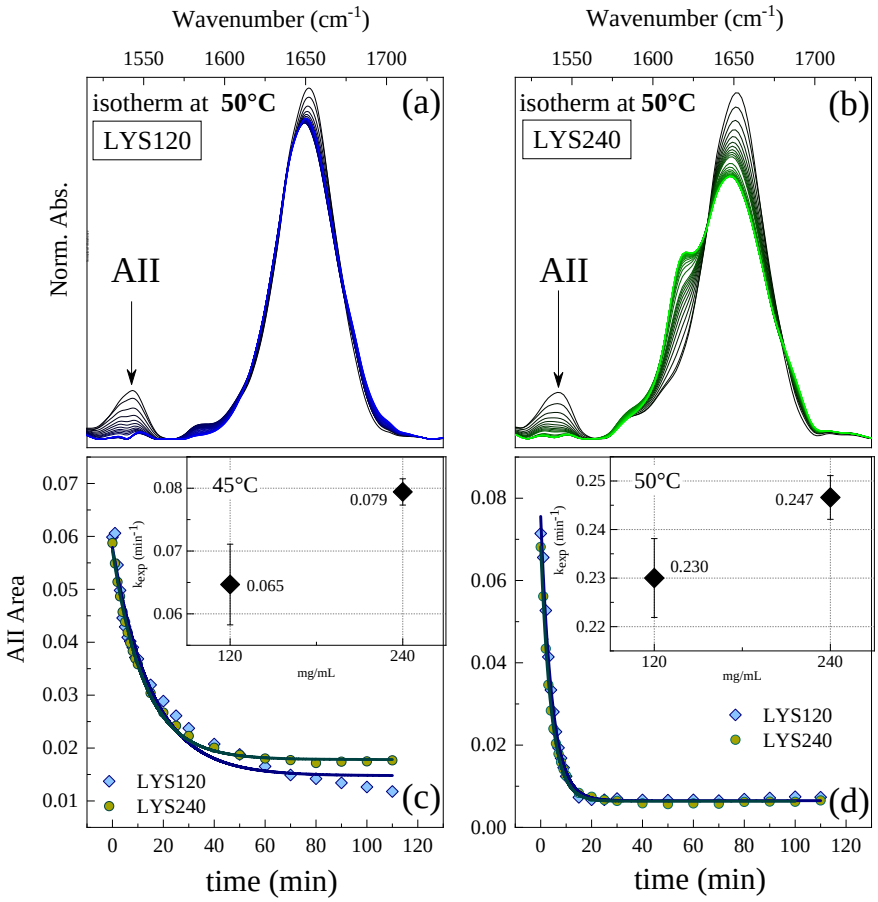

FIGURE 4.9: FTIR spectra of LYS120 (panel a) and LYS240 (panel b solutions recorded at 50 °C as a function of time. Panel (c) and (d) report the area values of AII band at 45 and 50 °C respectively. The experimental data are fitted using an exponential function, whose inverse value is the experimental exchange kinetic constant

To describe H/D exchange kinetic in proteins it is possible to adopt local unfolding and solvent penetration model [195, 208]:

$$F(H) \underset{}{\overset{k_1}{\rightleftharpoons}} U(H) \xrightarrow{k_s} U(D)$$

F(H) and U(H) are the hydrogenated folded and unfolded species, F(D) and U(D) the corresponding deuterated ones. k_1 and k_{-1} are the kinetic constant of unfolding and refolding, respectively, while k_s is the kinetic exchange constant when the protein in the unfolded state. The collective exchange pseudo constant is given by:

$$k_{ex} = \frac{k_1 k_s}{k_{-1} + k_s} \tag{4.4}$$

If $k_s >> k_1$, the hydrogen exchange constant is much greater than the refolding one and the experimental constant equals the unfolding one:

$$k_{ex} = k_1 \tag{4.5}$$

If $k_1 >> k_s$, the refolding constant is much greater than the isotopic exchange one and the experimental constant is given by:

$$k_{ex} = K_T k_s \tag{4.6}$$

In this limit the protein unfolds and refolds many times before that all the exchangeable hydrogens of the segment can be replaced by deuterium.

[LYS] (mg/ml)	T (°C)	K_T	k_{exp} (min^{-1})
120	45	0.07	0.065 ± 0.006
240	45	0.07	0.079 ± 0.002
120	50	0.36	0.230 ± 0.008
240	50	0.36	0.247 ± 0.005

TABLE 4.2: Equilibrium constant (K_T) and experimental exchange kinetic constant (k_{exp}) values at different experimental conditions.

The T-dependence of the aggregate band intensity at 1618 cm^{-1} is reported in figure 4.8 (c): the signal increases above 40°C, when a small fraction of U is present (1.4 %), in line with the idea that the formation of ordered aggregates requires unfolding. The band reaches a maximum at 54°C, close to the Tm, then start decreasing to practically disappear at 80°C; a characteristic "depletion temperature" Tdep about 65°C can be inferred. The disappearance of this band has been already observed in similar T-ranges, when LYS aggregates are formed under reducing conditions [179] or in presence of denaturing cosolvents [196, 198]. This depletion indicates the dissociation of the ordered oligomers formed at lower T and/or their rearrangement towards unordered aggregates. In fact, a protein precipitate, which recalls an opaque particulate gel[146], is observed at the end of the thermal treatment, suggesting that the formation of amorphous aggregates does occur at high T. We remark that the FTIR AI signal is not sensitive to aggregates of amorphous nature [209]. The initial loosening of β-sheet contacts starts at lower temperatures (10°C or more) than previously observed for analogous structures formed in different environments (presence of DMSO or ethanol and higher pH) [196, 198], suggesting that the thermal stability of amyloid oligomers depends on the solvating conditions. Likely, the high surface charge of lysozyme at pH= 1.8 [200]

might induce the formation of relatively small oligomers, with a lower thermal stability. To provide additional insights on the properties of concentrated systems, micro-DSC measurements are performed on the LYS60, LYS120 and LYS240 samples.

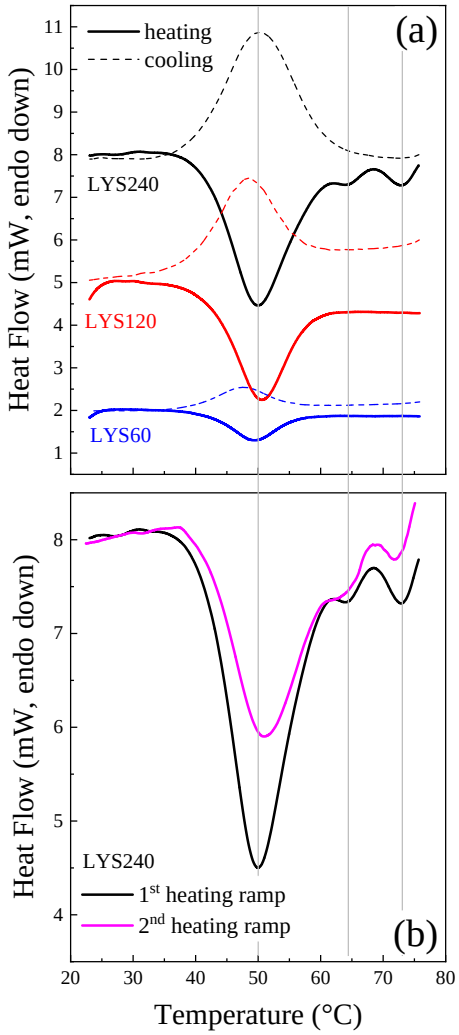

FIGURE 4.10: (a) Micro-DSC measures of LYS60, LYS120 and LYS240 solutions, the heating (solid line) and cooling (dashed line) thermograms are shown. The curves are rescaled to a better visualization. (b) Comparison between the first and the second heating ramp for the LYS240 sample.

The calorimetric scans reported in figure 4.10 (a) display an endothermic event centered at about 50°C consistent with the outcomes of the FTIR results, and with the trend reported in literature as regards the thermal unfolding of LYS at low pH and higher dilution [154, 160, 178]. For the LYS60 and LYS120 samples, the profile is typical of a two-state transition with a high degree of reversibility, as assessed by the cooling scans. An apparent enthalpy change of 50 ± 6 kcal/mol (LYS60) and 54 ± 6 kcal/mol (LYS120) can be estimated from the

thermograms, in reasonable agreement with the FTIR estimate 67 $\pm$ 4 kcal/mol (LYS120), also in view of the simplifying assumptions considered to extract these values. For the sake of comparison, recent DSC investigations on diluted samples led to enthalpy changes of 70 kcal/mol [178] and 100 kcal/mol [160] at pH= 2, while an average transition enthalpy of 97 kcal/mol (Tm= 58°C) result from previous independent studies (LYS concentration from 1 to 10 mg/ml and pH from 2.3 to 2.5) [210]. For the LYS240 sample in which development of ordered aggregates has been observed by FTIR the thermal behavior follows a more complex profile under which several transitions can be identified: after the first peak centered at 50°C due to unfolding, a transition at 64°C and a well-defined peak at 72°C can be also observed. Protein precipitation is found to take place at the end of the heating ramp, due to the formation of amorphous aggregates. The formation of opaque irreversible gels has been observed after incubation at 81°C of more diluted samples at neutral pH [132]. Figure 4.10 (a) indicates that, also in this case, significant reversibility of the unfolding process is observed by the cooling scan, suggesting that a large fraction of protein is still present in the monomeric form. This is confirmed by looking at the second heating scan reported in figure 4.10 (b). The melting temperature is not affected by the concentration increase and a rather minor reduction of the apparent enthalpy change is observed.

Sample	T_m(°C)	ΔH_{F-U} (kcalmol^{-1})
LYS60	49.4 $\pm$ 1.5	49.9 $\pm$ 5.5
LYS120	50.4 $\pm$ 1.6	53.7 $\pm$ 5.9
LYS240	50.3 $\pm$ 1.6	45.1 $\pm$ 5.1

TABLE 4.3: thermodynamic parameters of the melting temperature (T_m) and enthalpy (ΔH_{F-U}) obtained by the mDSC thermograms

This is likely due to the interference of amyloid self-aggregation occurring along the melting range. Interestingly, on the basis of a detailed DSC study on quite concentrated LYS solutions (up to 100 mg/ml) at higher pH values, the occurrence of irreversible aggregation, probably of amorphous nature, does not seem to modify very much the features of the unfolding endotherm during the heating cycle [211]. Overall, DSC results confirm that, self-crowding and supramolecular assembly do not alter considerably the F $\longleftrightarrow$ U equilibrium in these concentrated samples. The second and third endothermic peaks of figure 4.10 (b) at 64°C and 72°C are rather small: they might reflect either an entropy driven event (like a dissociation/association phenomenon) or a further conformational change of a partly

unfolded state [179]. Anyhow, the appearance of these features, not evidenced at lower concentrations, should be mainly connected to the development of ordered aggregates that form starting from 40°C and then tend to disappear at T $>$ 55°C (Figure 4.8 c). The fact that the depletion temperature T_{dep} about 65°C estimated form FTIR data is close to that at which the second endothermic feature appears, might suggest a common origin. Concerning the peak at 72°C, in the case of a LYS hydrogel thermally produced upon addition of DTT, an endothermic component found within 75-80 °C is assigned to the melting of gel aggregates [147]. On the other hand, higher melting points (110-115°C), assigned to the formation of strong fiber-fiber interaction, were obtained for gels of amyloid fibers formed starting from 10-100 mg/ml LYS solutions, after long incubation times at 55°C and pH= 2.5 [144]. A different explanation is needed in our case, since amyloid aggregates are not present for T $>$ 70°C. For the LYS240 sample, after the unfolding, several thermal events take place; these include the formation of amyloid oligomers, their dissociation, amorphous aggregation, and other possible conformational changes. Structural information regarding the formed oligomers, is obtained from SAXS measurements. In this respect figure 4.11 shows the scattering curves of the concentrated LYS240 solution as a function of temperature.

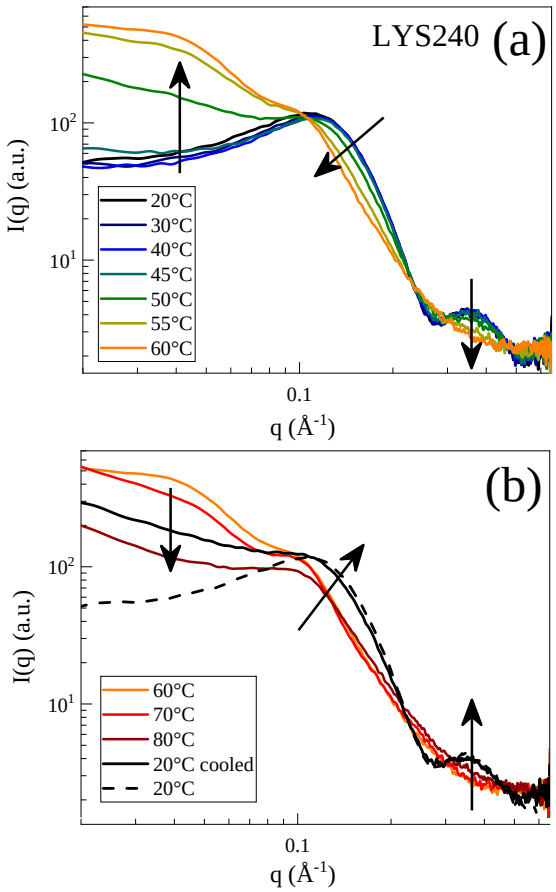

FIGURE 4.11: Experimental scattering curve I(q), of LYS240 solution at pH 1.8, as a function of temperature. (a) shows the curves at the temperatures in which the aggregation occurs. (b) shows those in which the aggregates dissociates.

The thermal evolution of the scattering curves (figure 4.11 (a)) is in total agreement with the FTIR and the mDSC findings, evidencing that the effect of protein concentration on the protein melting temperature is negligible, suggesting that the self-crowding and the supra-molecular assembly involved in the aggregation process, does not have an important influence on the transition from the folded to the unfolded state. At temperature higher than 40°C the inter-particle distance correlations due to attractive potential give rise to an enhancement of the low angle scattering. The formation of LYS aggregates is visible from the increase of I(q) in the low-q region. After 60°C the aggregates dissociation take place. Indeed in figure 4.11 (b), I(q) at low angle decreases. At temperatures above 60°C, the interactions that induce the proteins to form the amyloid-like aggregate structures are broken. Panel (b) shows the comparison between the SAXS curves collected at 20°C before and after the thermal treatment. The solid and dotted black curves overlap in the medium/high q

regions [184, 186]. Instead the curves differ in the low q region, still indicating the presence of some aggregates. However, it is important to remember that the speed of cooling is very important in the possibility of reactivating the kinetics of aggregation. Indeed in subsection 4.2.5 the aggregation kinetics at 4 different temperatures are investigated with the FTIR technique. The SAXS curve at 20°C after the heat treatment of the sample has a lower scattering intensity values at low q than the SAXS curves recorded at 55°C and 60°C, indicating that many aggregates have been dissociated. The reversibility of the system is to be understood as the structural reversibility of the protein monomer and not so much as the global reversibility of the system. Probably by implementing a much faster cooling it is also possible to achieve greater reversibility of the whole system. These findings suggest that the oligomers have a low thermal stability because are mainly generated by the establishment of physical interactions between the protein monomers.

Figure 4.12 reports the temperature dependence of C_S and Γ_A of LYS240 solution.

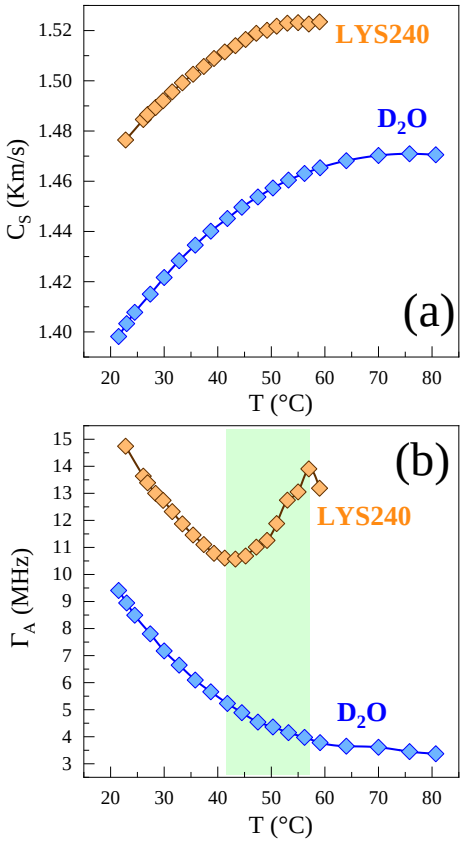

FIGURE 4.12: temperature dependence of LYS240 solution: (a) sound velocity C_S, (b) damping rate Γ_A.

The speed of sound shown in figure 4.12 (a) increases with LYS concentration in a linear

like manner, with C_S value greatest at the highest temperature. The speed of sound follows similar shaped curves as the LYS120 solution (figure 4.7). The speed of sound curves shift upwards with increasing concentration and the peak shift towards lower temperatures. There is a significant variation with concentration across the whole temperature range. Instead, the Γ_A behaviour shown in panel (b), is totally different with respect to that of LYS120 solution where the aggregation don't occurs. In particular, until 45°C, Γ_A decreases due to the reduction of solution viscosity. Above 45°C, Γ_A revers the trend and strongly increases with temperature due to the formation of LYS aggregates [206, 212, 161]. The formation of protein aggregates, increase the number of the physical phenomena that can contribute to efficiently dampen the acoustic wave in the material. This could be due to the system's viscosity increases due to the formation of interactions between the aggregates. To the increase in the degree of complexity of the aggregate itself compared to the protein monomer, which have more degrees of freedom and then a huge number of channels able to dissipate the acoustic wave energy [213]. Also acoustic scattering phenomena could occur [213].
Thanks to the multitechnical approach used to characterize the complex thermal behavior of the more concentrated solution of lysozyme, LYS240, it is possible to sketch a phase diagram that qualitatively synthesizes the thermal evolution of the protein under the used experimental conditions.

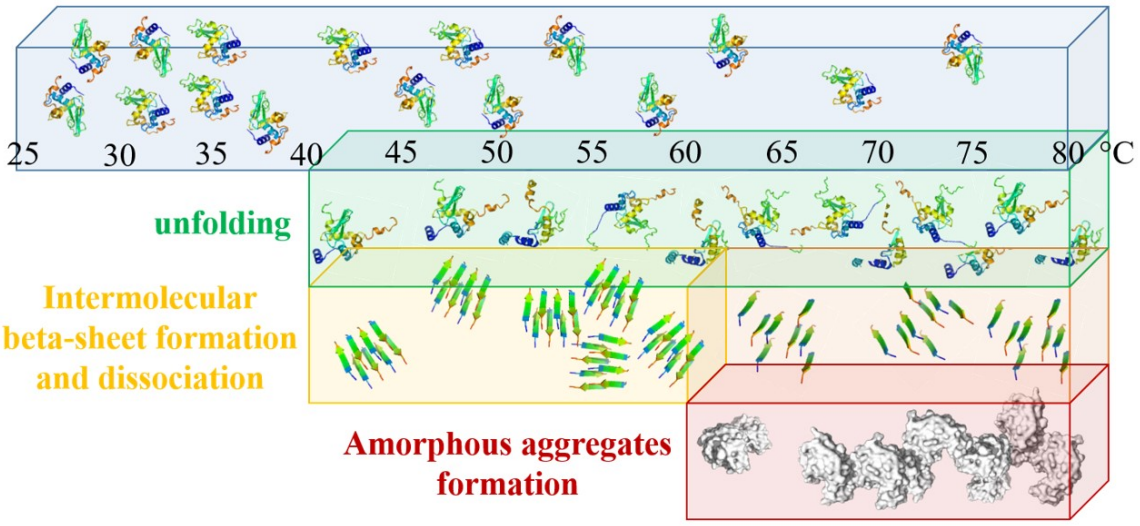

FIGURE 4.13: thermal behaviour of LYS240 solution: sketch of the phase diagram.

By combining the results of the different experiments, especially those obtained from the

FTIR and SAXS investigations, it is possible to draw the thermal history of the LYS240 sample. In particular, the monomers of the protein begin to unfold as the temperature increases. At 40°C, when the unfolded species fraction of 1.4% is present, the proteins begin to aggregate forming amyloid-like oligomers. A maximum amount of oligomers is reached at about 55°C. For temperatures above 60°C the oligomeric species become thermally unstable and dissociate. At these high temperatures it is even possible to form amorphous aggregates.

4.2.5 Thermal aggregation kinetic and gelation of LYS

Since the monomer folding/unfolding is relatively fast, in absence of aggregation, the FTIR spectra (recorded within a few minutes) would refer to F $\leftrightarrow$ U equilibrium conditions at any T. On the other hand, protein aggregation is kinetically controlled and it could take place at temporal scales longer than those considered in the presented experiments [196, 198, 199, 207, 210]. Thus, to gain more insights on the aggregation kinetics, FTIR spectra have been collected as a function of time at fixed temperatures. Figure 4.14 shows the time evolution of the absorbance at 1618 cm^{-1} at four temperatures around T_m.

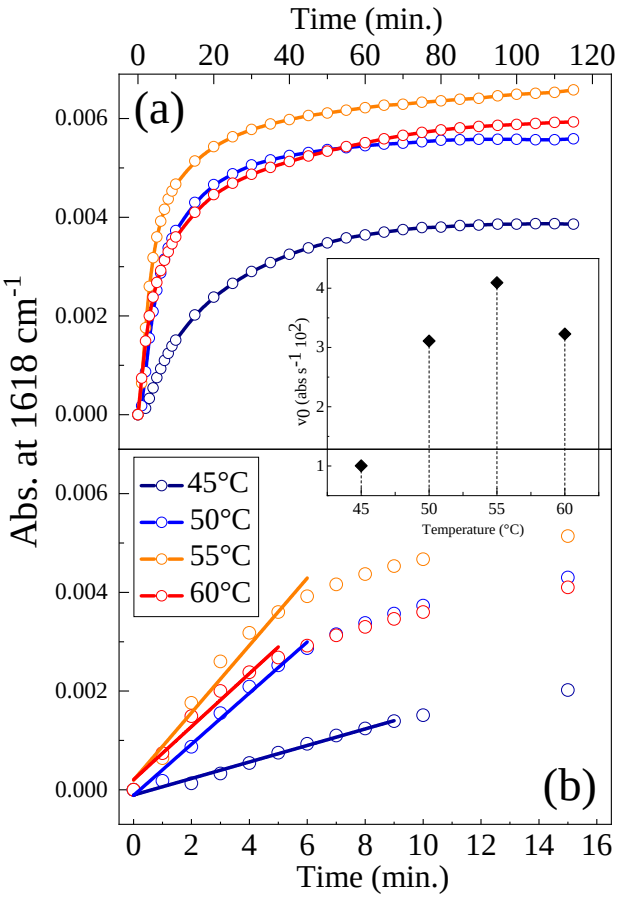

FIGURE 4.14: FTIR absorbance of LYS240 at 1618 cm_{-1} as a function of time, determined at different temperatures. Panel (a) shows the evolution obtained up to 120 minutes, while panel (b) highlights the first 16 minutes. Straight lines in panel (b) are obtained by a linear curve fitting procedure on the first data point, to estimate the initial aggregation rate (v_0). The temperature dependence of v_0 is shown in the inset.

No aggregate signals are observed below 45°C, due to the small fraction of unfolded species, and above 60°C, due to the thermal instability of the ordered oligomers. At intermediate temperatures (figure 4.14), the production of oligomer is fast within the first 10-20

minutes and then it levels out at longer times. Similar trends have been previously obtained in the presence of ethanol or DMSO as denaturants [196, 198]. Consistently with the findings reported in figure 4.8, the maximum production of aggregates is achieved at 55°C, which is close to T_m. In addition, the initial aggregation rate v_0, evaluated by a linear fitting of the first data points (figure 4.14 b), shows a maximum close to T_m (inset of figure 4.14 a). The decrease of v_0 observed at 60°C suggests that the dissociation (or rearrangement) of ordered aggregates starts to be of some relevance at this temperature. At all temperatures, the aggregation rate slows down quite rapidly with time, becoming considerably small after about 30-40 minutes. Even if the appearance of limiting concentration values (particularly evident for 45 and 50°C) might reflect a reversible aggregation process [126], in the present case, this is attributed to a kinetic arrest, related to the increased number and/or size of the aggregates. In fact, an increment of the solution viscosity is noticed at the end of the thermal treatment. The reported trends clearly show that after two-hours incubation, different (quasi-stationary) fractions of ordered aggregates are produced in the different cases. The subsequent rapid cooling to room T of the samples treated at 45 and 50°C, induces the formation of transparent gels within a few hours. This is often the case also for the sample incubated at 55°C, even if sometime a partially opaque gel is observed. Instead, thermal incubation at 60°C always caused the formation of an opaque gel already at high temperature, indicating that the amorphous aggregation becomes competitive starting from 55-60°C.

The SANS, SAXS and FTIR curves of the transparent hydrogels produced after curing at 45, 50 and 55°C, (hereafter referred to as GEL45, GEL50 and GEL55, respectively) are reported in figure 4.15, highlighting the different aggregates content depending on the thermal treatment used to form the gel, and therefore presumably a different degree of networking of the gel matrix.

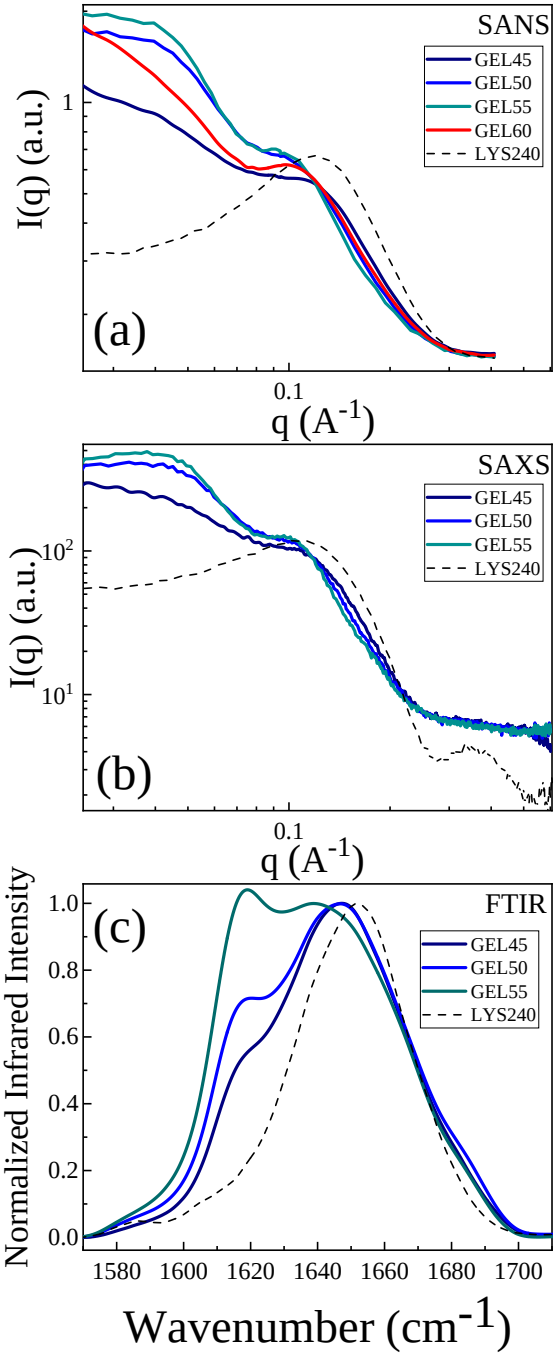

FIGURE 4.15: experimental scattering curve I(q) (panel a and b), and FTIR spectra (panel c) of the diffrent LYS based hydrogels.

The relative intensity of the band at 1618 cm^{-1} of the FTIR spectra in panel c, due to the ordered oligomers, increases with the incubation temperature in line with the trends of figure 4.14. A visual inspection of the samples indicates that stronger gels are formed at higher temperatures, suggesting a correlation between their mechanical properties and the size and/or number of ordered aggregates. Depicted spectra also show that the GEL45 and

GEL50 still contain a large amount of α-helix, suggesting that monomers are still present in the jellified samples, in line with the occurrence of a kinetic arrest of the aggregation process. Nevertheless the preservation of residual native-like structures in amyloid oligomers is also expected [135]. Comparison between the spectra of GEL45 and GEL50 with those of the corresponding viscous liquids (LYS240) recorded at the end of the incubation at 45 and 50°C (figure 4.16), evidences only minor relative intensity variations of the 1618 cm^{-1} signal.

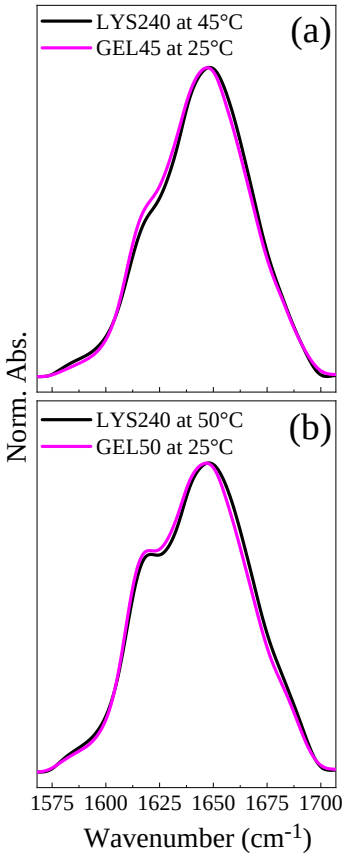

FIGURE 4.16: comparison between the spectra of LYS240 at 45 and 50°C after 2 hours of thermal cure and the spectra of the respective gels formed through the protocol: respectively 2 hours at 45°C (GEL45) in the panel (a), and 2 hours at 50°C (GEL50) in the panel (b).

Thus, interprotein β-sheet do not further develop significantly during the gelation process, in which links among ordered aggregates build up a percolating network. The shift of the main band highlights that refolding to native structure takes place upon cooling. This is mainly ascribed to the dispersed monomers. It can be hypothesized that the transparent gels (GEL45 and GEL50) are made by rather small amyloid oligomers interacting by weak (non-specific) interactions and contain a fraction of native monomers.

4.2.6 Structural and elastic properties of LYS hydrogel

To assess from a mechanical point of view, the formation of a true jellified system, a rheological characterization on the transparent GEL50 is performed. Mechanically, a gel is a semi-solid system in which the elastic modulus (G^I) is higher than the viscous modulus (G^{II}) as a function of frequency and temperature. Otherwise, even if the system does not flow visually after solicitation, it should be considered as a concentrated dispersion and not as a real jellified system. At this extent, frequency sweep tests are performed at different temperatures, as shown in figure 4.17 (a).

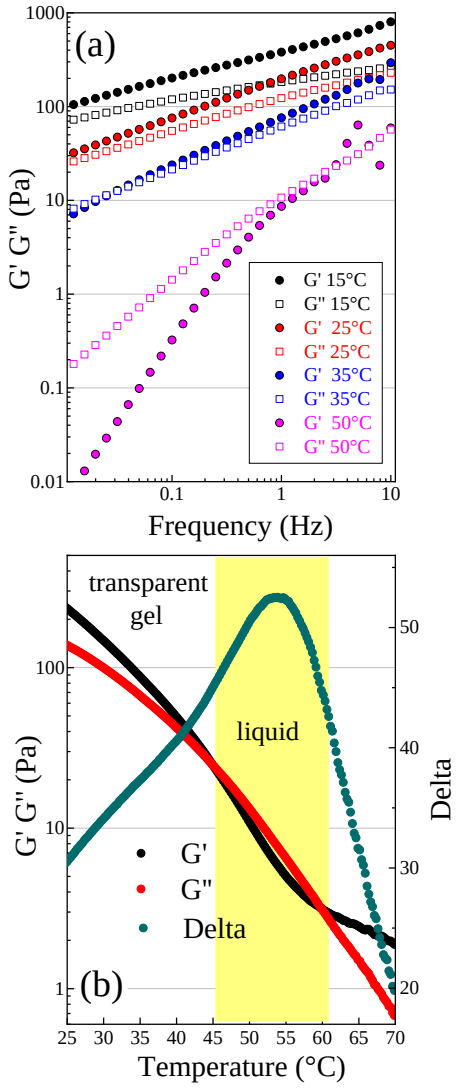

FIGURE 4.17: Panel (a) frequency sweep traces of the GEL50 at different temperatures (15, 25, 35 and 50°C) (a). Panel (b) effect of temperature on the elastic modulus (G^I), viscous modulus (G^{II}) and phase angle (Delta) of GEL50.

The values of G^I and G^{II} at a given frequency decrease with increasing temperature, reflecting the overall weakening of intermolecular interactions. At 15 and 25°C the value of G^I is higher than G^{II} in all range of analyzed frequencies, while at higher temperature (from 35 to 50°C), a crossover frequency between the two moduli appears. This crossover frequency is at around 0.03 Hz at 35°C, shifting to a higher frequency at 50°C (ca. 3 Hz). Thus, this system can be considered as a gel at 15°C and 25°C, but it behaves as a low consistency dispersion between 35°C and 50°C. The results obtained from the frequency sweep test are confirmed by temperature sweep test (figure 4.17 b), highlighting the effect of temperature on the elastic (G^I) and viscous (G^{II}) modulus of the hydrogel at the frequency of 1 Hz. At room temperature the sample is a true jellified system, being the elastic modulus (G^I) higher than the viscous (G^{II}) one. Both moduli decrease with increasing temperature: the material is becoming progressively softer, which can be attributed to the weakening of interactions among aggregates. At 45°C some of the links that build up the percolating network are broken. The system is not able to sustain itself anymore and starts to flow ($G^{II} > G^I$ modulus). This transition from gel to liquid phase is due to the reduction of the links between the amyloid-like oligomers. Indeed, these are thermally more labile than the cross β-sheet links inside the oligomers themselves, becoming unstable only at T $>$ 55-60°C (figure 4.8). This case seems to be different from that of the "strong-link" gels of LYS, produced at room temperature in denaturing conditions (using tetramethylurea as a cosolvent), in which interparticle links are more elastic than intraparticle ones [214]. We also notice that the elastic modulus of the oligomer hydrogel GEL50 is lower by at least one order of magnitude with respect to the self-supporting hydrogels developed Yan et al. (1-4kPa) [145, 147]. However, we recall that their preparation involves the heating up to 85°C (10 minutes) of more diluted LYS solutions (30-70 mg/ml) in the presence of the reductant DTT and then slow cooling to room conditions. In this way, β-sheet fibrils produced at high temperature, further develop during cooling, leading to a fibrillar network through the formation of inter-fibril junctions [145, 147]. The different stiffness of the GEL50 can be then rationalized based on its different nature, which encompasses the entanglement of small amyloid oligomers rather than more rigid fibrils. This seems also consistent with the findings of Navarra et al. who demonstrated the possibility of forming fibrillar hydrogels of BSA with different strength, after incubation at 60°C at various pH values: the weakest gel was formed at pH 7.4 when, together with long and thin fibrils, also numerous oligomers are present [215].

Figure 4.17 (b) shows that above 60°C the elastic becomes greater than the viscous modulus

once again, testifying a further structural change in the system. In fact, at the end of the thermal treatment an opaque solid-like phase appeared, the formation of which is expected to take place at 60°C, due to oligomers rearrangement and amorphous aggregation, as discussed before.

Transient grating spectroscopy provides an alternative and complementary non-contactless approach than rheology to study the phase transitions in soft materials, thanks to its sensitivity to the matter viscous and elastic properties [216]. In this respect, figure 4.18 reports the acoustic temperature behaviour of the gel system.

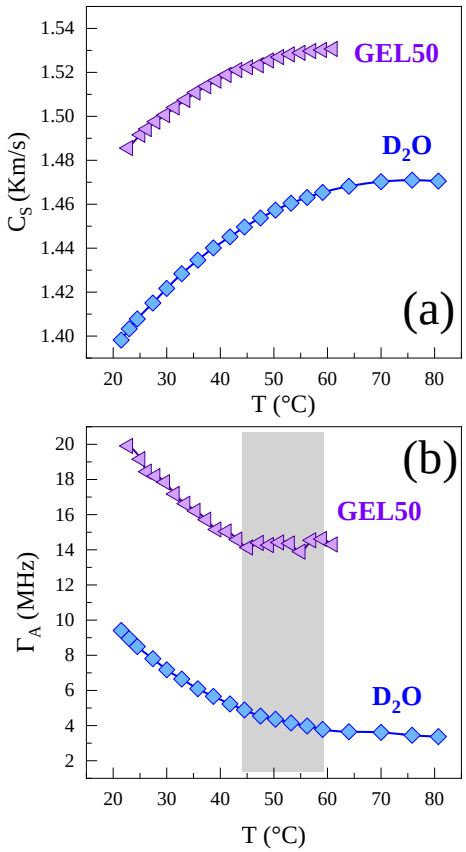

FIGURE 4.18: temperature dependence of LYS based hydrogel: (a) sound velocity C_S, (b) damping rate Γ_A.

The speed of sound of the LYS gel, have absolute value higher than that of the respective LYS solution from which the gel was formed. This is related to the viscosity increase due to the formation of physical interactions between the oligomers that make the system capable to retain water into the gel matrix and to self-sustaining [217]. The shaped curves as a function of temperature, is the same previously discussed in the LYS solutions. In this case, only a little signature of the gel to sol transition is recognizable at around 45°C in the speed

profile. On the contrary the acoustic wave damping rate shows a marked change passing from the gel to the liquid phase [212]. Since the Γ_A trend is approximately linear above and below the transition point, the kink in the data trend identify the gel to liquid transition temperature [218]. This trend is related with the breaking of the gel network that implies the transition to the liquid state, that occurs at 45°C. The increased sound attenuation in the gel phase appears to be a generic occurrence, and has already been observed in other biological systems like gelatin [219] and polysaccharides [220]. The notable sensitivity of the damping rate of the acoustic wave over the speed of sound to the LYS conformational rearrangements, aggregation and also to the physical state of the system, highlights the major role played by molecular relaxation.

DSC trace of this gel (figure 4.19) still displays an endothermic transition centered 52°C, as previously observed for LYS dispersions, indicating the presence of a fraction of native protein in the hydrogel. Differently from the dispersions, the heating of the hydrogel up to 80°C causes irreversible unfolding of the protein, since no transition is observed during the cooling back scan. From the ratio between the enthalpy associated to the transition of GEL50 (Δ H$_{F-U}$= 5.3 $\pm$ 0.3) and that to the main transition of the LYS240 dispersion (Δ H$_{F-U}$= 45.1 $\pm$ 5.1), a rough estimate of the fraction of native protein in the hydrogel could be attempted. An approximate value of 12 % is obtained, as long as interferences of concomitant processes are neglected.

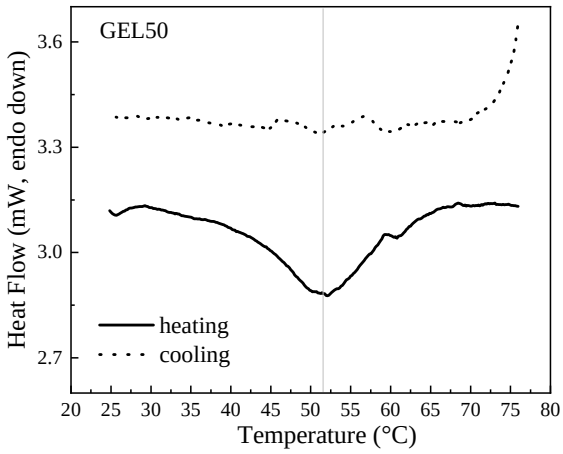

FIGURE 4.19: mDSC traces (heating and cooling back) of GEL50.

To explain on molecular and structural terms the rheological and thermal behavior of the hydrogel, FTIR and SAXS curves of the sample are recorded, shown respectively in figure

4.20 and figure 4.21. Figure 4.20 shows the FTIR spectra as a function of temperature, of the GEL50.

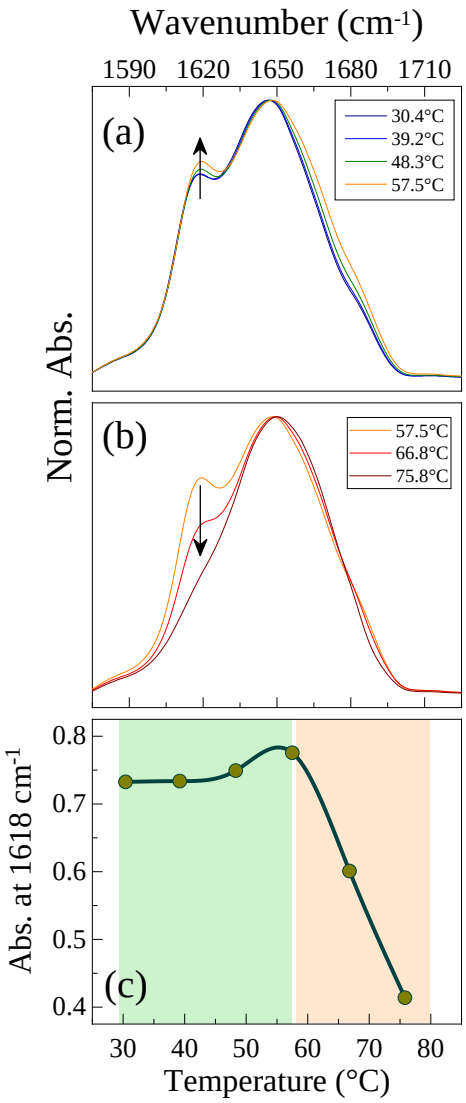

FIGURE 4.20: FTIR spectra of GEL50 recorded as a function of temperature. The arrows highlight the increase (a) and the decrease (b) of the aggregate signal. The temperature dependence of the absorbance at 1618 cm^{-1} due to ordered aggregates is reported in panel (c).

The plot of I(q) as a function of temperature, of the GEL50, is reported in figure 4.21.

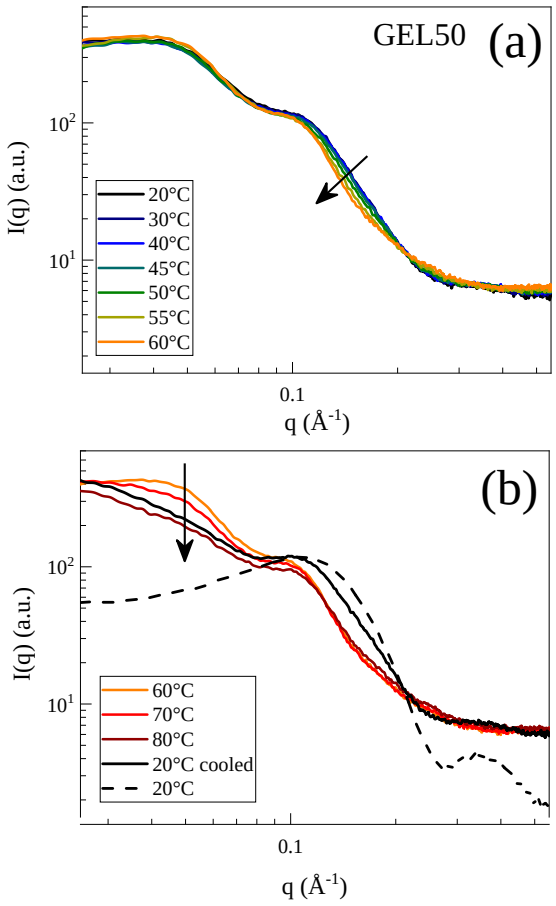

FIGURE 4.21: Experimental scattering curve I(q), of LYS based gel, as a function of temperature. (a) shows the curves at the temperatures in which the aggregation occurs. (b) shows those in which the aggregates dissociates.

The outputs obtained by FTIR and SAXS data highlights no changes of the experimental curves going from 30 to 40°C (figures 4.20 and 4.21) when the sample is in the gel phase, confirming that variations of G^I and G^{II} mainly relate to the reduction of (non-specific) interactions among oligomers, which do not involve the cross β-sheet motifs. As a matter of fact, spectral changes remain rather limited also up to about 60°C when the gel-to-liquid transition has occurred. The visible blue-shift of the main peak at 1650 cm^{-1} is ascribed to the unfolding of native monomers, still present within the jellified sample, while the small relative increase of the aggregate band observed at T $>$ 40°C (figure 4.20) is due to the restart of oligomers production. This clearly means that the gel-to-liquid transition is not connected with the number and/or size of amyloid oligomers but rather to the interactions among them. For T $>$ 60°C (figure 4.20) the depletion of the band at 1618 cm^{-1} and the shoulder at 1680 cm^{-1} reflects the breaking of the antiparallel β-sheet contacts: in these conditions the formation of amorphous aggregates is favored. The SAXS curves (figure 4.21) follow the

same behaviour as the FTIR spectra.

To better synthesize and visualize the dependence of the GEL50 on temperature, it is possible to schematize a phase diagram picture, as done before for the LYS240 solution (figure 4.13).

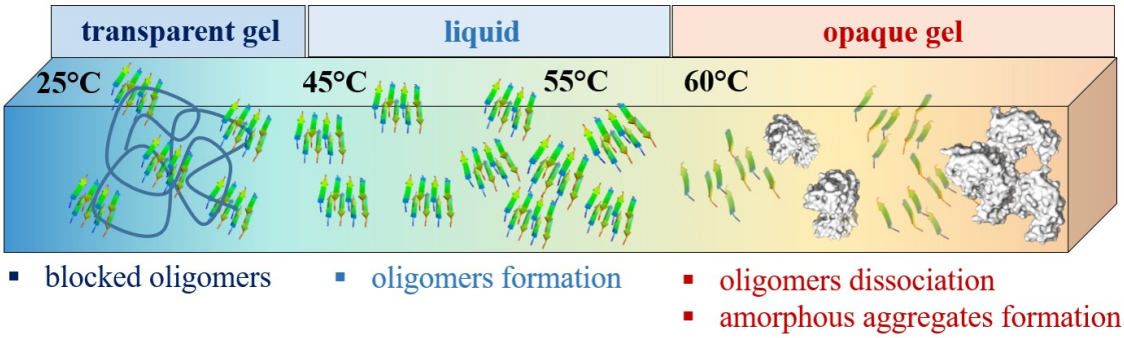

FIGURE 4.22: thermal behaviour of GEL50 sample: sketch of the phase diagram.

Combining both the molecular and macroscopic information obtained by the used multi-technical approach, it is possible to follow the thermal history of the protein based hydrogel, GEL50. In particular from room temperature until 45°C the system is dominated by the elastic component and can be described as a percolating system. At 45°C the transition from gel to liquid phase occurs, due to the breakdown of the physical interactions between oligomers. After the gel to sol transition, the oligomers can diffuse, and the aggregation kinetics restart. Indeed, between 45 and 60°C the intermolecular β-sheet connections reform, generating an higher content of oligomeric aggregates. For temperatures above 60°C this type of aggregates dissociate and other aggregation paths occur, which involve the formation of amorphous aggregates, as seen previously for the thermal history of the LYS240 solution shown in figure 4.13.

4.2.7 Thermo-reversibility and oligomers dissociation of LYS hydrogel

Figure 4.23 shows the results of the time sweep test, employed to investigate at selected temperatures the time response of rheological moduli (G^I and G^{II}) during the transition from the gel to the liquid states and vice versa. In particular, the elastic and viscous moduli of the hydrogel were measured as a function of time at 50°C to study the gel-to-liquid transition and then at 25°C to study the liquid-to-gel reverse process (first cycle); the same analysis was repeated on the resulting sample (second cycle).

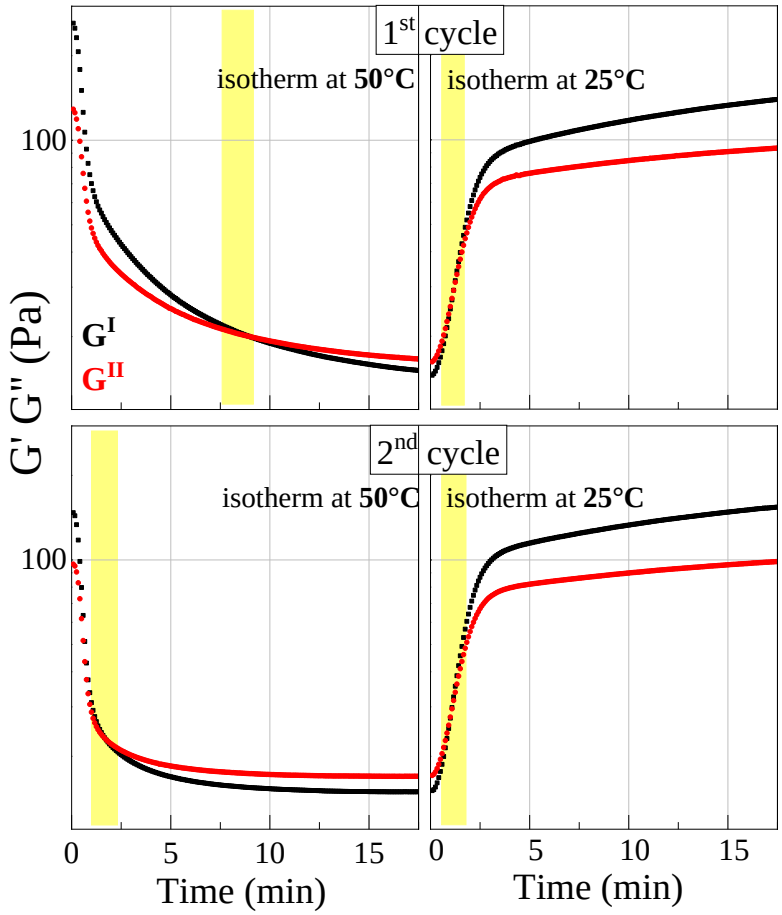

FIGURE 4.23: Elastic modulus (G^I) and viscous modulus (G^{II}) as a function of time. The GEL50 has been incubated at 50°C (20 minutes) to follow the gel-to-liquid transition and then cooled back to 25°C (20 minutes) to follow the reverse process (first cycle); the same treatment has been repeated on the resulting sample (second cycle).

During the first cycle the gel-to-liquid transition occurs after about 8 minutes at 50°C; this liquid sample reforms a gel when cooled back to 25°C; in this case, both moduli increase fast within the first 3 minutes then their increase slows down. The jellified sample becomes liquid again upon reheating to 50°C. We notice that now the transition is somewhat anticipated, consistently with the fact that the full stiffness of the gel is not reached at

the end of the first cycle, due to the limited incubation time. Finally, upon cooling the liquid sample to 25°C, reformation of the gel is observed again, with a time response analogous to that of the first cycle. Overall, the data indicate that from a mechanical point of view, this oligomer hydrogel can be considered a thermo-reversible one [145, 146, 147]. This capability is strictly related to the possibility of reversibly breaking and reforming the weak links among amyloid oligomers, while the number and size of these latter being unaltered in the 25 to 50°C range (figures 4.20 and 4.21).

An attempt has been made to reverse the oligomer formation, exploiting their instability at high temperature. Figure 10a shows the spectra obtained as a function of time for the GEL50 treated at 80°C. In the initial spectrum (acquisition time about 3 minutes) the aggregate band at 1618 cm^{-1} is strongly depleted, indicating that amyloid oligomers quickly rearrange at this temperature.

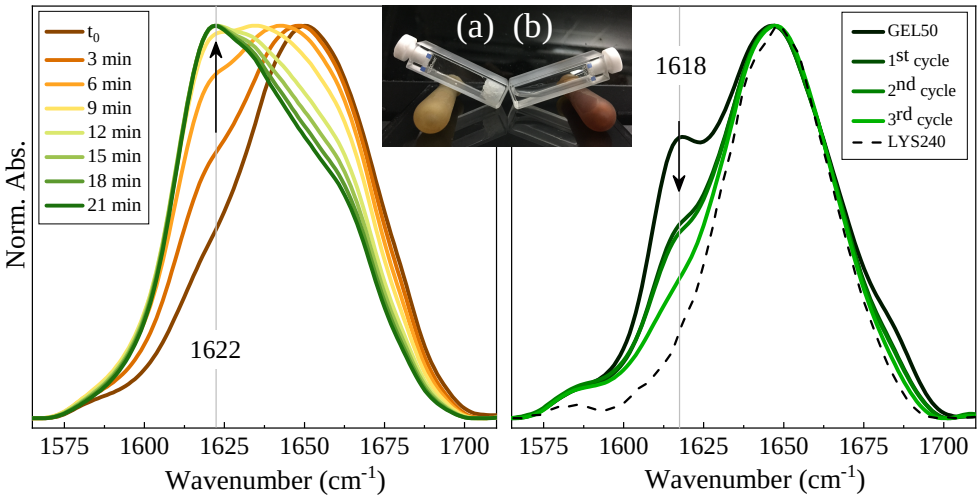

FIGURE 4.24: FTIR spectra of the system after the thermal treatments. Panel (a) long thermal treatment at 80°C. Panel (b) short thermal cycles at 80°C. In the picture: the two systems at the end of the thermal treatment.

Significant spectral modifications are then detected as a function of time, with an overall intensity redistribution towards lower frequencies. A strong decrease of the relative intensity of the signal at 1650 cm^{-1} is observed, whereas, surprisingly, a new spectral component located at 1622 cm^{-1} grows up, becoming dominant at about 20 minutes treatment. If the first effect can be ascribed to the progressive loss of any residual α structure in these drastic conditions, the assignment of the emerged low frequency component is more difficult to understand. Macroscopically, starting from the transparent gel, the sample transforms into an opaque solid-like system (figure 4.24 a), typically constituted by amorphous aggregates [130, 131, 146]. Yet, the presence of a 1622 cm^{-1} component might suggest that, together

with amorphous aggregates, also a fraction of different amyloid species with parallel β-sheet structure [156] and/or fibrillary nature were formed [135]. Their production could be facilitated by hydrolytic processes occurring at 80°C and low pH. Starting from these results, a procedure has been tested aimed at dissociating amyloid oligomers, characteristic of the transparent gel, to recover the native monomers. The gel was incubated at 80°C just for one minute and then quickly cooled down at 25°C (1st cycle); the procedure has been repeated two other times (2nd and 3rd cycles). The spectrum obtained after each cycle is compared to the spectrum of the initial GEL50 sample and to that of the (H/D exchanged) LYS240 solutions (figure 4.24 b). As it can be seen, a significant reduction of the 1618 cm^{-1} component is obtained in this way, avoiding other major spectral changes. After the 3rd cycle the spectrum resembles that of the starting solution employed to form the gel, even if the remaining shoulder around 1618 cm^{-1} indicates the persistence of a fraction of aggregates. At the same time, the viscosity of the sample visibly reduces with the number of cycles and a low viscosity liquid is obtained at the end of the treatment; the sample remains liquid also in the following days. These results indicate that amyloid oligomers of LYS can be dissociated into monomers at high temperatures and that a significant extent of refolding can be achieved by fast cooling. This is necessary to limit other competitive processes such as hydrolysis and/or formation of other ordered and amorphous aggregates.

Chapter 5

Conclusions

The identification of specific interactions of water molecules with a solute and its reciprocal activity on water structure is the main goal of this thesis. The present results highlight how hydration influences the structure and promotes different aggregation products of peptides and proteins. This study is developed within the frame of the basic chemical-physics properties investigation of biological systems. A deeper knowledge of how surrounding water molecules affect the conformational changes and self-aggregation mechanisms provides a basis for the control of self-assembly processes and thus a control over the properties of biomaterials.

The solvation of the tripeptide GSH in different experimental conditions of concentration, pH, temperature and presence of ionic species in solution is investigated in order to address the role of specific peptide-water interactions. The UVRR spectroscopy provides a powerful experimental tool taking advantage of its sensitivity and selectivity specifically probing the structural dynamics of water at the interface with both the peptide backbone and the side groups. MD calculations support experimental results and provide a detailed understanding of the solvation processes at a molecular level. The analysis of the OH stretching signal of water confirms its relevant attitude to probe the perturbation of the H-bond structure of water induced by the peptide. The band spectral features reveal an increased disruption of the more ordered H-bonded water induced by the tripeptide deprotonated form compared to the protonated one. The inspection of the amide signals that are well visible in the UVRR spectra also in diluted solutions gains insight to the hydrogen bonding network around the amide sites of tripeptide and its dependence as a function of different experimental conditions. Another remarkable result, the spectral changes observed mainly on Amide I signal, suggests that in diluted solution the number of hydrogen bonds between the peptide C$=$O group and water is larger than in concentrated solution. This behavior is observed

to be further promoted at basic pH, in accordance with the more marked capacity of deprotonated form of GSH in decreasing the intermolecular order of water. Potassium salts of the halogen group are used to investigate the ions effect on the GSH structure. The results are compared to imidazolium based ionic liquids of the halogen series. The UV Raman spectra shows marked variations depending on the different halogenic anions present in solution, while significant variations cannot be attributable to the cations.

MD simulations are able to give an explanation of the improved influence of ILs in comparison to the correspondent potassium salts as due to the higher propensity of inorganic salts to form ionic pairs in solution. Concerning the anion effect on the solvation shell of GSH, experiments and simulations are in total agreement. The results are explained by the resonance model of the peptide link. In particular, chloride and bromide anions show a similar interaction mechanism at the amide site, the effect is grater for chloride due to its higher charge density. Both anions interact with GSH at the N——H site resulting in a reduction of the hydrogen bond strength. They are responsible for a reduction of polarity of the surroundings in comparison to pure water. In such conditions the peptide neutral structure in the ground state is stabilized consequently strengthening the C═O and weakening the C——N bond. This structural effect results in a blue shift of Amide I band, a red shift of Amide II and increases the Amide I Raman cross-section. On the contrary, it is found that iodide anion increases the number of water molecules at the peptide link, creating a strong polar environment. In this case, the effect is the stabilization in the ground state of the dipolar resonance structure that weaken the C═O and strengthen the C——N bond. From a spectroscopic point of view, this structural effect involves a red shift of Amide I band, a blue shift of Amide II and an increasing of the Amide II Raman cross-section. The observed dependence on temperature of the frequencies of the amide bands reflects the progressive reduction in the strength of hydrogen bond interactions on amide sites of GSH due to water thermal motions. This effect is highlighted by the MD simulations showing a decrease in the distribution of water molecules around the C═O and the N——H sites. Spectroscopically this effect is reflected in a blue shift of the Amide I band due to the shortening of the C═O bond, and a red shift of the Amide II and Amide III_3 bands due to the lengthening of the C——N bond. The MD simulations do not find significant effects on the conformational changes of peptide bonds upon temperature. From the UVRR spectra at high temperature a signal at about 1500 cm^{-1} appears. In previous measurements this band is assigned to the cis-Amide II mode. The difference between the experimental results and

the simulation is attributable to the resonance effect. Using UV light in combination with temperature it is possible to promote the trans to cis isomerization. The ions effects on the trans-cis isomerization are explained by the variation of the solvation shell at the peptide site. Chloride and bromide anions stabilize the neutral resonance structure of the peptide link in the ground state but this form is suppressed in the excited state creating a hindrance to rotation around the C —— N bond. On the contrary, iodide anion stabilizes the ground state dipolar resonance form of GSH that is suppressed in the excited state allowing the rotation of the peptide link. The outcomes reported in chapter 3 provide a reference basis for a thorough understanding of the molecular mechanism driving the solvation dynamics of glutathione, representing a key step toward the comprehension of the biological functionality of this tripeptide.

Chapter 4 focuses on the thermal unfolding and aggregation of highly concentrated lysozyme aqueous solutions (pH= 1.8). Formation of protein hydrogels is monitored in situ and basic structure-property correlations are established. DC and FTIR experiments show that a two-state model (F $\leftrightarrow$ U) is appropriate to describe LYS thermal unfolding at low concentration and also at 120 mg/ml, when no aggregation is probed, leading to thermodynamic data (T_m= 53°C and Δ H_{F-U}= 70 kcal/mol) in line with literature results on diluted solutions. FTIR spectroscopy in conjunction with H/D exchange experiments demonstrate that the thermal stability of LYS does not change upon further self-crowding to 240 mg/ml, even when fast self-aggregation is observed. These findings are supported by DSC experiments. Thus, contrary to some expectations, at low pH values, self-crowding and aggregation only marginally affect the F $\leftrightarrow$ U equilibrium. SAXS data demonstrate also a great structural reversibility of LYS after the thermal treatment when temperature is decreased at room one. Furthermore HD-TG data show a marked modulation of the viscosity coefficient induced by the unfolding process, evidencing an important contribution of the molecular relaxation phenomena to the D_V trend. In the very concentrated sample (240 mg/ml), aggregates with antiparallel β-sheet structures develop at T $>$ 40°C (U percentages larger than 1.4 %), confirming that the aggregation is triggered by the unfolding. From metastable U species, amyloid aggregates quickly form in the adopted conditions, reaching a kinetically arrested state. The self-crowding and the high monomeric charge act together favoring the rapid formation of (kinetically trapped) amyloid oligomers, over that of amorphous aggregates or fibrils. These oligomers recall those described by Muschol and coworkers, as compact metastable species that might further originate curvilinear fibrils or oligomer precipitates [137]. The

HD-TG data confirm the aggregates presence above 40°C where a marked D_V trend deviation has been observed. Amyloid oligomers show a limited thermal stability: their content deceases above 55°C, close to T_m, becoming negligible at 75°C. Even if aggregation and other rearrangements take place going from 25 to 75°C, DSC and SAXS experiments evidence that a large fraction of LYS remains able to refold upon cooling. Isothermal aggregation kinetics indicate that amyloid oligomers do not form significantly below 45°C, due to the low content of U species, and above 60°C, due to their intrinsic thermal instability. Within 45 and 60°C their formation follows similar trends: the aggregation rate levels off after 20-30 minutes, leading to quasi-stationary oligomers fractions after two-hours incubation. The rapid cooling of the samples treated at 45 and 50°C leads to the formation of transparent hydrogels, whose mechanical properties relate to the amount of aggregates produced during the isothermal incubation. Indeed, these protein hydrogels are made by amyloid oligomers that build up a percolating network by interacting through rather weak (non-specific) interactions. The amyloid self-assembly is almost arrested upon cooling, which is ascribed to the slowing down of protein diffusion and to the rapid refolding of monomers. In fact, the gel phase still contains a reservoir of native LYS, as confirmed by DSC and SAXS measurements. A detailed rheological analysis of the protein hydrogel (GEL50) confirms its elastic character ($G^I > G^{II}$) at low temperatures, evidencing together with the HD-TG data the occurrence of a gel-to-liquid transition at 45°C. A comparative FTIR analysis indicates that this transition is related to the depletion of the weak links among the oligomers. The hydrogel is found to be thermo-reversible, due to the possibility of breaking and reforming these (non-specific) inter-aggregates interactions. The amyloid oligomers themselves can be dissociated back into monomers: a significant degree of refolding is obtained after consecutive cycles, involving short-time exposures at 80°C (one minute) and fast cooling. Thus, this hydrogel sample, made by rather small amyloid oligomers, can be retransformed back to a solution of native proteins. Overall, results demonstrate that protein hydrogels, constituted by amyloid oligomers interconnected by weak (reversible) links, can be easily formed in self-crowding conditions.

This type of oligomeric hydrogels might be relevant in cellular biology and pharmaceutical industry when denaturation occurs in concentrated environments. They could be also considered as a subclass of specific functional biomaterials, along with analogous systems of fibrillar nature. Containing high quantities of amyloid oligomers, these hydrogels can be further exploited to study the inter-aggregate entanglement, which must be a rather general

process, especially relevant in crowded conditions.

Chapter 6

Appendices

6.1 A basic principals of SAXS and SANS

Among the methods used in structural biology, small-angle scattering of X-rays (SAXS) and neutrons (SANS) are techniques that closely fulfil the above requirements for structural systems biology [221]. SAS provides information about the overall structure and structural transitions of biological macromolecules in solutions at a low resolution (1–2 nm) [222, 223]. Conceptually, the scattering experiment is relatively simple and it is performed on solutions, which do not require special sample treatment (growth of crystals, isotopic labelling, cryofreezing, etc.). The samples are exposed to a collimated monochromatic X-ray or neutron beam with the wave vector $k = \frac{2\pi}{\lambda}$ where λ is the radiation wavelength. The isotropic scattered intensity, I, is recorded as a function of the momentum transfer $q = \frac{4\pi}{\lambda} sin(\theta)$, where 2θ is the angle between the incident and scattered beam. The scattering from the solvent is measured separately and subtracted to remove the background signal. The difference between the X-ray and neutron scattering lies in the fact that the X-rays are scattered largely by electrons, whereas the neutrons interact with nuclei. The contrast, which is the difference between the scattering length density of the particle and that of the solvent, is therefore given by the electron density for X-rays and nuclear density for neutrons. SAXS and SANS are highly complementary methods, whereby the former technique is faster and requires less material. SANS is sensitive to isotopic H/D exchange, which is experimentally used for contrast variation involving measurements in different H_2O/D_2O mixtures and/or specific predeuteration of subunits, which provides unique information about complex particles [224]. Anyway, the basic equations and the methods used are similar for SAXS and SANS. The net SAS intensity I(q) after solvent subtraction contains two contributions. The so-called *form factor* P(q) emerges from the scattering by individual particles in solution and is used to extract the structural information. The *structure factor* S(q) is due to interference

effects between the different particles and yields information about the interparticle interactions. Once that the intensity of the sample is recorded and the background corrected, the equation that describe I(q) can be summarize as:

$$I(q) = KP(q)S(q) \tag{6.1}$$

There are tree components in the equation to be considered. One is, K, that is a constant which takes into account the particle contrast, volume and concentration. The other factors as anticipated above are the form factor, P(q), bears the shape and the internal density distribution of the particles, and the structure factor, S(q), carries the information about particle-particle interactions, such as inter-particle distances and degree of order [225].

6.2 List of publications

1. Catalini, S., Perinelli, D.R., Sassi, P., Comez, L., Palmieri, G.F., Morresi, A., Bonacucina, G., Foggi, P., Pucciarelli, S. and Paolantoni, M. (2021). *Amyloid Self-Assembly of Lysozyme in Self-Crowded Conditions: The Formation of a Protein Oligomer Hydrogel*. Biomacromolecules.

2. Ragnoni, E., Catalini, S., Becucci, M., Lapini, A. and Foggi, P. (2021). *Linear and Non-Linear Middle Infrared Spectra of Penicillin G in the CO Stretching Mode Region*. Symmetry, 13, 106.

3. Bottari, C., Catalini, S., Foggi, P., Mancini, I., Mele, A., Perinelli, D.R., Paciaroni, A., Gessini, A., Masciovecchio, C. and Rossi, B., (2021). *Base-specific pre-melting and melting transitions of DNA in presence of ionic liquids probed by synchrotron-based UV resonance Raman scattering*. Journal of Molecular Liquids, 115433.

4. Rossi, B., Bottari, C., Catalini, S., D'Amico, F., Gessini, A., and Masciovecchio, C. (2020). *Chapter 13 - Synchrotron-based ultraviolet resonance Raman scattering for material science*. Molecular and Laser Spectroscopy, Advances and Applications: Volume 2, 447-482.

5. Diener, M., Adamcik, J., Bergfreund, J., Catalini, S., Fischer, P., and Mezzenga, R. (2020). *Rigid Fibrillar Quaternary Structures Induced by Divalent Ions in a Carboxylated Linear Polysaccharide*. ACS Macro Letters, 9, 115-121.

6. Rossi, B., Catalini, S., Bottari, C., Gessini, A., and Masciovecchio, C. (2019, September). *Frontiers of UV resonant raman spectroscopy by using synchrotron radiation: the case of aqueous solvation of model peptides*. In UV and Higher Energy Photonics: From Materials to Applications 2019 (Vol. 11086, p. 110860N). International Society for Optics and Photonics.

7. Catalini, S., Rossi, B., Foggi, P., Masciovecchio, C., and Bruni, F. (2019). *Aqueous solvation of glutathione probed by UV resonance Raman spectroscopy*. Journal of Molecular Liquids, 283, 537-547.

8. Catalini, S., Taschin, A., Bartolini, P., Foggi, P., and Torre, R. (2019). *Probing Globular Protein Self-Assembling Dynamics by Heterodyne Transient Grating Experiments*. Applied Sciences, 9(3), 405.

6.3 List of conferences

1. 24/02/2021 (Perugia), online workshop, "Giornata di discussione sui Metodi Chimico Fisici utilizzati per lo studio di fasi condensate: informazioni dall'interazione tra fotoni e materiali - con dimostrazioni di laboratorio ed applicazioni", Oral contribution
   title: *Investigation of soft materials by linear and non-linear spectroscopies: linking molecular to macroscopic properties*.

2. 21-25/09/2020 (Bari), 4th online edition, Italian Soft Days 2020, Poster contribution
   title: *Self-Assembling of Lysozyme: Structural and Elastic Investigation*.
   Best Poster Award

3. 21-26/07/2019 (Erice) 5th Conference on Frontiers in Water Biophysics, Poster contribution
   title: *Vibrational and Elastic investigation of Lysozyme self-assembling processes*.

4. 23/05/2019 (Sesto Fiorentino), Participation at PhD day10, Oral contribution
   title: *Hydration of Glutathione probed by UV Raman Spectroscopy*.

5. 17-20/03/2019 (Andalo), Conference "XV International Workshop on Complex Systems"
   Oral contribution, title: *Self-Assembling of Lysozyme: Microscopic and Macroscopic investigations*
   Poster contribution, title: *Hydration of the tripeptide Glutathione probed by UV Raman Spectroscopy*.

6. 25/01/2019 (Sesto Fiorentino) Klein colloquium, Oral contribution
   title: *Self-Assembling of Lysozyme Molecular and Elastic investigations*.

7. 13-14/09/2018 (Padova), Conference "Italian Soft Days 2018", Poster contribution
   title: *Microscopic and macroscopic investigations of self-assembling proteins toward the formation of biocompatible hydrogels*.

8. 31/05/2018 (Sesto Fiorentino), Participation at PhD day9, Oral contribution
   title: *Self-Assembling of globular proteins: "Cross and Delight"*.

9. 21-25/05/2018 (Trieste, ICTP), Conference "Conference on the Complex Interactions of Light and Biological Matter: Experiments meet Theory", Oral contribution
   title: *Vibrational study of a self-assembling globular protein*.

10. 23-27/05/2017 (Erice), Participation at the 4th conference "Frontiers in Water Biophysics" (FWB), Poster contribution
    title: *Spectroscopic study of the unfolding and aggregation processes of lysozyme under denaturing conditions: toward the formation of protein hydrogels*.

11. 07-09/06/2017 (Trieste, ICTP), Participation at GISR (2017) 5th national congress "Raman spectroscopies and non-linear optical effects", Poster contribution
    title: *Study of the processes of unfolding, aggregation and gelation of lysozyme in denaturing conditions through vibrational spectroscopy*.

6.4 Experiences abroad

1. 01/06/2019-22/11/2019 (ETH of Zurich), group of the professor Raffaele Mezzenga, Laboratory of Food and Soft Materials, Department of Health Sciences and Technology, Institute of Food, Nutrition and Health.

2. 26/02/2018-09/03/2018 (Forschungszentrum Jülich GmbH, Germany), 49th IFF Spring School 2018 "Physics of Life".

6.5 Research activities at European large facilities

1. 09-15/03/2021 (IUVS) ELETTRA proposal number: 20205486
   title: *Thermal stability of Poly-L-Proline structural motif as a function of salts and protic ionic liquids*.
   I am the main proposer

2. 27-31/01/2021 (IUVS) ELETTRA proposal number: 20205312
   title: *Solvation of glutathione in presence of ionic liquids: denaturant or protectant effect?*

3. 21-25/09/2020 (IUVS) CERIC proposal number: 20202148
   title: *Topology, thermal stability and behaviour of DNA in deep-eutectic solvents*.

4. 04-08/03/2020 (IUVS) CERIC proposal number: 20197165
   title: *Systematic investigation of the effect of imidazolium-based ionic liquids on the structural stability of DNA*.

5. 07-09/12/2019 (EIS-TIMER), FERMI proposal number: 20184052
   title: *Coherent control of electronic transfer in the Donor-MgP-Acceptor molecule using a chirped X-ray pulse*.

6. 13-17/11/2019 (IUVS), ELETTRA proposal number: 20190354
   title: *Effect of polar heads on self-assembling behaviour of amino acid based surfactants*.

7. 26-28/09/2019 (SANDALS experiment at ISIS), CERIC proposal number: 20187115
   title: *Investigation of the hydration shell around the active site of Glutathione by means of a protic ionic liquid*.

8. 03-07/08/2019 (IUVS), CERIC proposal number: 20192179
   title: *Systematic investigation on self assembly in DNA ionogels*.

9. 11-15/04/2019 (IUVS experiment at ELETTRA), CERIC proposal number: 20187115
   title: *Investigation of the hydration shell around the active site of Glutathione by means of a protic ionic liquid*.

10. 11-16/09/2018, ELETTRA proposal number: 20180196 (IUVS)
    title: *Characterization of drop-casted deposited ibuprofen and aromatic amino acids*.

11. 31/07/2018-05/08/2018 (IUVS), ELETTRA proposal number: 20180128
    title: *Molecular rearrangements in ternary mixtures of a-cyclodextrin undergone inverse freezing*.

12. 26-29/11/2017, CERIC proposal number: 20172087
    title: *Investigation on the self-assembling behaviour of amino acid based surfactants: effect of polar heads*.

13. 01-05/08/2017 (IUVS) and 13-17/12/2017 (SANS), CERIC proposal number: 20167071
    title: *Structural study of aggregation of Lysozyme in water/ethanol solutions*.

14. 18-21/07/2016 (IUVS) and 29/11/2016-02/12/2016 (SISSI), CERIC proposal number: 20162085
    title: *Dynamics of water in concentrated lysozyme solutions and its dependence on protein unfolding and aggregation*.

Bibliography

[1] Pier Luigi Gentili. *Untangling complex systems: a grand challenge for science*. CRC Press, 2018.

[2] Eric A Appel et al. "Supramolecular polymeric hydrogels". In: *Chemical Society Reviews* 41.18 (2012), pp. 6195–6214.

[3] Yongzheng Xing et al. "Self-assembled DNA hydrogels with designable thermal and enzymatic responsiveness". In: *Advanced Materials* 23.9 (2011), pp. 1117–1121.

[4] Michael Diener et al. "Rigid, Fibrillar Quaternary Structures Induced by Divalent Ions in a Carboxylated Linear Polysaccharide". In: *ACS Macro Letters* 9.1 (2020), pp. 115–121.

[5] Chandrashekhar V Kulkarni et al. "Self-assembled lipid cubic phase and cubosomes for the delivery of aspirin as a model drug". In: *Langmuir* 33.38 (2017), pp. 9907–9915.

[6] Minkyu Kim, Shengchang Tang, and Bradley D Olsen. "Physics of engineered protein hydrogels". In: *Journal of Polymer Science Part B: Polymer Physics* 51.7 (2013), pp. 587–601.

[7] Martin Loose, Karsten Kruse, and Petra Schwille. "Protein self-organization: lessons from the min system". In: *Annual review of biophysics* 40 (2011), pp. 315–336.

[8] Hans Frauenfelder. "Proteins: paradigms of complexity". In: *Proceedings of the National Academy of Sciences* 99.suppl 1 (2002), pp. 2479–2480.

[9] Maria Florencia Pignataro, Maria Georgina Herrera, and Veronica Isabel Dodero. "Evaluation of Peptide/Protein Self-Assembly and Aggregation by Spectroscopic Methods". In: *Molecules* 25.20 (2020), p. 4854.

[10] Damien Laage, Thomas Elsaesser, and James T Hynes. "Water dynamics in the hydration shells of biomolecules". In: *Chemical Reviews* 117.16 (2017), pp. 10694–10725.

[11] D Thirumalai, Govardhan Reddy, and John E Straub. "Role of water in protein aggregation and amyloid polymorphism". In: *Accounts of chemical research* 45.1 (2012), pp. 83–92.

[12] Richard C Remsing, Erte Xi, and Amish J Patel. "Protein hydration thermodynamics: the influence of flexibility and salt on hydrophobin II hydration". In: *The Journal of Physical Chemistry B* 122.13 (2018), pp. 3635–3646.

[13] Song-Ho Chong and Sihyun Ham. "Interaction with the surrounding water plays a key role in determining the aggregation propensity of proteins". In: *Angewandte Chemie International Edition* 53.15 (2014), pp. 3961–3964.

[14] Zahraa S Al-Garawi et al. "The diversity and utility of amyloid fibrils formed by short amyloidogenic peptides". In: *Interface Focus* 7.6 (2017), p. 20170027.

[15] Kuen Yong Lee and David J Mooney. "Hydrogels for tissue engineering". In: *Chemical reviews* 101.7 (2001), pp. 1869–1880.

[16] Walter E Rudzinski et al. "Hydrogels as controlled release devices in agriculture". In: *Designed monomers and polymers* 5.1 (2002), pp. 39–65.

[17] Robert W Boyd. *Nonlinear optics*. Academic press, 2019.

[18] Renato Torre. *Time-resolved spectroscopy in complex liquids*. Springer, 2007.

[19] B Rossi et al. "Chapter 13 - Synchrotron-based ultraviolet resonance Raman scattering for material science". In: *Molecular and Laser Spectroscopy*. Ed. by V.P. Gupta and Yukihiro Ozaki. Elsevier, 2020, pp. 447–482.

[20] Adam Willitsford et al. "Resonance Raman measurements utilizing a deep UV source". In: *Laser Radar Technology and Applications XIII*. Vol. 6950. International Society for Optics and Photonics. 2008, 69500A.

[21] Thomas G Spiro. "Resonance Raman spectroscopy. New structure probe for biological chromophores". In: *Accounts of Chemical Research* 7.10 (1974), pp. 339–344.

[22] E Smith and G Dent. "The theory of Raman spectroscopy". In: *Modern Raman spectroscopy-A practical approach* (2005), pp. 71–92.

[23] Lasse Jensen et al. "Theory and method for calculating resonance Raman scattering from resonance polarizability derivatives". In: *The Journal of chemical physics* 123.17 (2005), p. 174110.

[24] Sanford A Asher. "UV resonance Raman studies of molecular structure and dynamics". In: *Annu. Rev. Phys. Chem* 39 (1988), pp. 537–588.

[25] Sanford A Asher. "UV resonance Raman spectroscopy for analytical, physical, and biophysical chemistry. Part 1". In: *Analytical chemistry* 65.2 (1993), 59A–66A.

[26] Sanford A Asher. "UV resonance Raman spectroscopy for analytical, physical, and biophysical chemistry. Part 2". In: *Analytical chemistry* 65.4 (1993), 201A–210A.

[27] Francesco D'Amico et al. "UV resonant Raman scattering facility at Elettra". In: *Nuclear Instruments and Methods in Physics Research Section A: Accelerators, Spectrometers, Detectors and Associated Equipment* 703 (2013), pp. 33–37.

[28] T Tanaka and H Kitamura. "Figure-8 undulator as an insertion device with linear polarization and low on-axis power density". In: *Nuclear Instruments and Methods in Physics Research Section A: Accelerators, Spectrometers, Detectors and Associated Equipment* 364.2 (1995), pp. 368–373.

[29] H Eichler, G Salje, and H Stahl. "Thermal diffusion measurements using spatially periodic temperature distributions induced by laser light". In: *Journal of Applied Physics* 44.12 (1973), pp. 5383–5388.

[30] DW Pohl, SE Schwarz, and V Irniger. "Forced rayleigh scattering". In: *Physical Review Letters* 31.1 (1973), p. 32.

[31] Hans Joachim Eichler, Peter Günter, and Dieter W Pohl. *Laser-induced dynamic gratings*. Vol. 50. Springer, 2013.

[32] Yuen-Ron Shen. "The principles of nonlinear optics". In: *wi* (1984).

[33] H Eichler. "Introduction to the special issue on dynamic gratings and four-wave mixing". In: *IEEE journal of quantum electronics* 22.8 (1986), pp. 1194–1195.

[34] N Bloembergen. *Nonlinear Optics, 3rd printing*. 1977.

[35] Yong-Xin Yan and Keith A Nelson. "Impulsive stimulated light scattering. I. General theory". In: *The Journal of chemical physics* 87.11 (1987), pp. 6240–6256.

[36] Yongwu Yang and Keith A Nelson. "T C of the mode coupling theory evaluated from impulsive stimulated light scattering on salol". In: *Physical review letters* 74.24 (1995), p. 4883.

[37] AA Maznev, KA Nelson, and JA Rogers. "Optical heterodyne detection of laser-induced gratings". In: *Optics letters* 23.16 (1998), pp. 1319–1321.

[38] Gregory D Goodno, Gami Dadusc, and RJ Dwayne Miller. "Ultrafast heterodyne-detected transient-grating spectroscopy using diffractive optics". In: *JOSA B* 15.6 (1998), pp. 1791–1794.

[39] Zhen Yang. "Hofmeister effects: an explanation for the impact of ionic liquids on biocatalysis". In: *Journal of biotechnology* 144.1 (2009), pp. 12–22.

[40] Esben Thormann. "On understanding of the Hofmeister effect: how addition of salt alters the stability of temperature responsive polymers in aqueous solutions". In: *Rsc Advances* 2.22 (2012), pp. 8297–8305.

[41] Jana Paterova et al. "Reversal of the Hofmeister series: specific ion effects on peptides". In: *The Journal of Physical Chemistry B* 117.27 (2013), pp. 8150–8158.

[42] Awanish Kumar and Pannuru Venkatesu. "Does the stability of proteins in ionic liquids obey the Hofmeister series?" In: *International journal of biological macromolecules* 63 (2014), pp. 244–253.

[43] Jared D Smith, Richard J Saykally, and Phillip L Geissler. "The effects of dissolved halide anions on hydrogen bonding in liquid water". In: *Journal of the American Chemical Society* 129.45 (2007), pp. 13847–13856.

[44] Rekha Gaba et al. "Solvation behavior of glycine and glycyl dipeptide in aqueous 1-butyl-3-methylimidazolium bromide ionic liquid solutions at different temperatures". In: *Journal of Molecular Liquids* 233 (2017), pp. 38–44.

[45] Younhee Cho et al. "Effects of Hofmeister anions on the phase transition temperature of elastin-like polypeptides". In: *The Journal of Physical Chemistry B* 112.44 (2008), pp. 13765–13771.

[46] Diana Constantinescu, Hermann Weingärtner, and Christian Herrmann. "Protein denaturation by ionic liquids and the Hofmeister series: a case study of aqueous solutions of ribonuclease A". In: *Angewandte Chemie International Edition* 46.46 (2007), pp. 8887–8889.

[47] Varadhi Govinda and Pannuru Venkatesu. "A Comprehensive Experimental Study to Understand the Hofmeister Series of Anions of Aqueous Imidazolium-Based Ionic Liquids on Glycine Peptides". In: *Industrial & Engineering Chemistry Research* 53.50 (2014), pp. 19628–19642.

[48] Youngseon Shim, Hyung J Kim, and YounJoon Jung. "Solvation of a small metal-binding peptide in room-temperature ionic liquids". In: *Bulletin of the Korean Chemical Society* 33.11 (2012), pp. 3601–3606.

[49] Sara Catalini et al. "Aqueous solvation of glutathione probed by UV resonance Raman spectroscopy". In: *Journal of Molecular Liquids* 283 (2019), pp. 537–547.

[50] Ralf Dringen. "Metabolism and functions of glutathione in brain". In: *Progress in neurobiology* 62.6 (2000), pp. 649–671.

[51] Dallas L Rabenstein and Mary T Fairhurst. "Nuclear magnetic resonance studies of the solution chemistry of metal complexes. XI. Binding of methylmercury by sulfhydryl-containing amino acids and by glutathione". In: *Journal of the American Chemical Society* 97.8 (1975), pp. 2086–2092.

[52] Danyelle M Townsend, Kenneth D Tew, and Haim Tapiero. "The importance of glutathione in human disease". In: *Biomedicine & pharmacotherapy* 57.3-4 (2003), pp. 145–155.

[53] Juan Sastre, Federico V Pallardó, and Jose Viña. "Glutathione, oxidative stress and aging". In: *Age* 19.4 (1996), pp. 129–139.

[54] Gosk Jerzy, Rutowski Roman, and Rabczyński Jerzy. "Peripheral nerve tumours in own material". In: *Folia Neuropathologica* 42.4 (2004), pp. 203–207.

[55] John A Rupley and Giorgio Careri. "Protein hydration and function". In: *Advances in protein chemistry*. Vol. 41. Elsevier, 1991, pp. 37–172.

[56] Ernesto Scoppola et al. "Water-peptide site-specific interactions: A structural study on the hydration of glutathione". In: *Biophysical journal* 106.8 (2014), pp. 1701–1709.

[57] Sulayman A Oladepo et al. "Elucidating peptide and protein structure and dynamics: UV resonance Raman spectroscopy". In: *The journal of physical chemistry letters* 2.4 (2011), pp. 334–344.

[58] Ming Xu et al. "Hen egg white lysozyme fibrillation: a deep-UV resonance Raman spectroscopic study". In: *Journal of biophotonics* 1.3 (2008), pp. 215–229.

[59] Ryan S Jakubek et al. "Ultraviolet resonance Raman spectroscopic markers for protein structure and dynamics". In: *TrAC Trends in Analytical Chemistry* 103 (2018), pp. 223–229.

[60] Alexander V Mikhonin et al. "Assignments and conformational dependencies of the amide III peptide backbone UV resonance Raman bands". In: *The Journal of Physical Chemistry B* 108.49 (2004), pp. 19020–19028.

[61] David Punihaole et al. "UV resonance Raman investigation of the aqueous solvation dependence of primary amide vibrations". In: *The Journal of Physical Chemistry B* 119.10 (2015), pp. 3931–3939.

[62] David A Case et al. *Amber 10*. Tech. rep. University of California, 2008.

[63] KG Sprenger, Vance W Jaeger, and Jim Pfaendtner. "The general AMBER force field (GAFF) can accurately predict thermodynamic and transport properties of many ionic liquids". In: *The Journal of Physical Chemistry B* 119.18 (2015), pp. 5882–5895.

[64] Jan Picalek et al. "Aqueous solutions of ionic liquids: study of the solution/vapor interface using molecular dynamics simulations". In: *Physical Chemistry Chemical Physics* 10.37 (2008), pp. 5765–5775.

[65] Wei Jiang et al. "Molecular dynamics simulation of the energetic room-temperature ionic liquid, 1-hydroxyethyl-4-amino-1, 2, 4-triazolium nitrate (HEATN)". In: *The Journal of Physical Chemistry B* 112.10 (2008), pp. 3121–3131.

[66] Jose Mario Martinez and Leandro Martinez. "Packing optimization for automated generation of complex system's initial configurations for molecular dynamics and docking". In: *Journal of computational chemistry* 24.7 (2003), pp. 819–825.

[67] L Martinez et al. "Software news and update packmol: a package for building initial configurations for molecular dynamics simulations". In: *J. Comput. Chem* 30.13 (2009), pp. 2157–2164.

[68] B Hess, H Bekker, and HJC Berendsen. "Fraaije JGEM. LINCS: A linear constraint solver for molecular simulations". In: *J Comput Chem* 18.12 (1997), pp. 1463–72.

[69] Tom Darden, Darrin York, and Lee Pedersen. "Particle mesh Ewald: An N · log (N) method for Ewald sums in large systems". In: *The Journal of chemical physics* 98.12 (1993), pp. 10089–10092.

[70] Walter Brand et al. "Interaction of hesperetin glucuronide conjugates with human BCRP, MRP2 and MRP3 as detected in membrane vesicles of overexpressing baculovirus-infected Sf9 cells". In: *Biopharmaceutics and drug disposition* 32.9 (2011), pp. 530–535.

[71] HJC Berendsen et al. "GROMACS: fast, flexible, and free". In: *J. Comput. Chem* 26.16 (2005), pp. 1701–1718.

[72] Erik Lindahl, Berk Hess, and David Van Der Spoel. "GROMACS 3.0: a package for molecular simulation and trajectory analysis". In: *Molecular modeling annual* 7.8 (2001), pp. 306–317.

[73] HJC Berendsen. "D. vanderSpoel, R. vanDrunen". In: *Comput. Phys. Commun* 91 (1995), pp. 43–56.

[74] William Humphrey, Andrew Dalke, and Klaus Schulten. "VMD: visual molecular dynamics". In: *Journal of molecular graphics* 14.1 (1996), pp. 33–38.

[75] Hiromi Kitano, Kohei Takaha, and Makoto Gemmei-Ide. "Raman spectroscopic study on the structure of water in aqueous solution of α, ω-amino acids". In: *Journal of colloid and interface science* 283.2 (2005), pp. 452–458.

[76] Hiromi Kitano, Kohei Takaha, and Makoto Gemmei-Ide. "Raman spectroscopic study of the structure of water in aqueous solutions of amphoteric polymers". In: *Physical Chemistry Chemical Physics* 8.10 (2006), pp. 1178–1185.

[77] Xi Zhang et al. "HCl, KCl and KOH solvation resolved solute-solvent interactions and solution surface stress". In: *Applied Surface Science* 422 (2017), pp. 475–481.

[78] Shohei Saita et al. "Ionic liquids showing phase separation with water prepared by mixing hydrophilic and polar amino acid ionic liquids". In: *Chemical Communications* 49.79 (2013), pp. 8988–8990.

[79] WB Monosmith and GE Walrafen. "Temperature dependence of the Raman OH-stretching overtone from liquid water". In: *The Journal of chemical physics* 81.2 (1984), pp. 669–674.

[80] JL Green, AR Lacey, and MG Sceats. "Spectroscopic evidence for spatial correlations of hydrogen bonds in liquid water". In: *The Journal of Physical Chemistry* 90.17 (1986), pp. 3958–3964.

[81] Paola Sassi et al. "Water/alcohol mixtures: A spectroscopic study of the water-saturated 1-octanol solution". In: *The Journal of Physical Chemistry B* 108.50 (2004), pp. 19557–19565.

[82] Alessandro Di Michele et al. "Modulation of hydrophobic effect by cosolutes". In: *The Journal of Physical Chemistry B* 110.42 (2006), pp. 21077–21085.

[83] Vladimir S Marinov, Zhorro S Nickolov, and Hiroatsu Matsuura. "Raman spectroscopic study of water structure in aqueous nonionic surfactant solutions". In: *The Journal of Physical Chemistry B* 105.41 (2001), pp. 9953–9959.

[84] JD Eaves et al. "Hydrogen bonds in liquid water are broken only fleetingly". In: *Proceedings of the National Academy of Sciences* 102.37 (2005), pp. 13019–13022.

[85] Cettina Bottari et al. "Hydration properties and water structure in aqueous solutions of native and modified cyclodextrins by UV R aman and B rillouin scattering". In: *Journal of Raman Spectroscopy* 49.6 (2018), pp. 1076–1085.

[86] Sunho Song et al. "Assignment of a new conformation-sensitive UV resonance Raman band in peptides and proteins". In: *Journal of the American Chemical Society* 110.25 (1988), pp. 8547–8548.

[87] Zhenhuan Chi and Sanford A Asher. "Ultraviolet resonance Raman examination of horse apomyoglobin acid unfolding intermediates". In: *Biochemistry* 38.26 (1999), pp. 8196–8203.

[88] Sanford A Asher et al. "Dihedral ψ angle dependence of the amide III vibration: A uniquely sensitive UV resonance Raman secondary structural probe". In: *Journal of the American Chemical Society* 123.47 (2001), pp. 11775–11781.

[89] Sunho Song and Sanford A Asher. "UV resonance Raman studies of peptide conformation in poly (L-lysine), poly (L-glutamic acid), and model complexes: the basis for protein secondary structure determinations". In: *Journal of the American Chemical Society* 111.12 (1989), pp. 4295–4305.

[90] Janet SW Holtz et al. "Applications of a new 206.5-nm continuous-wave laser source: UV Raman determination of protein secondary structure and CVD diamond material properties". In: *Applied spectroscopy* 50.11 (1996), pp. 1459–1468.

[91] Sulayman A Oladepo et al. "UV resonance Raman investigations of peptide and protein structure and dynamics". In: *Chemical reviews* 112.5 (2012), pp. 2604–2628.

[92] Issei Harada et al. "Preresonance Raman spectra of simple amides using ultraviolet lasers". In: *Journal of Raman Spectroscopy* 4.1 (1975), pp. 91–98.

[93] Yoko Sugawara et al. "Preresonance Raman studies of poly (L-lysine), poly (L-glutamic acid), and deuterated N-methylacetamides". In: *Biopolymers: Original Research on Biomolecules* 17.6 (1978), pp. 1405–1421.

[94] XG Chen et al. "UV Raman Determination of the $\pi \rightarrow \pi^*$ Excited State Geometry of N-Methylacetamide: Vibrational Enhancement Pattern". In: *Journal of the American Chemical Society* 117.10 (1995), pp. 2884–2895.

[95] XG Chen et al. "Resonance Raman examination of the electronic excited states of glycylglycine and other dipeptides: Observation of a carboxylate $\rightarrow$ amide charge transfer transition". In: *Journal of the American Chemical Society* 118.40 (1996), pp. 9705–9715.

[96] Renee D JiJi et al. "Intermediacy of poly (L-proline) II and β-strand conformations in poly (L-lysine) β-sheet formation probed by temperature-jump/UV resonance Raman spectroscopy". In: *Biochemistry* 45.1 (2006), pp. 34–41.

[97] Michel Picquart et al. "Vibrational spectroscopic study of glutathione complexation in aqueous solutions". In: *Biospectroscopy* 5.6 (1999), pp. 328–337.

[98] Jipei Shi and Jianping Wang. "Interaction between metal cation and unnatural peptide backbone mediated by polarized water molecules: Study of infrared spectroscopy and computations". In: *The Journal of Physical Chemistry B* 118.43 (2014), pp. 12336–12347.

[99] Nataliya S Myshakina, Zeeshan Ahmed, and Sanford A Asher. "Dependence of amide vibrations on hydrogen bonding". In: *The Journal of Physical Chemistry B* 112.38 (2008), pp. 11873–11877.

[100] Aleksandr V Mikhonin et al. "Peptide secondary structure folding reaction coordinate: Correlation between UV Raman amide III frequency, ψ Ramachandran angle, and hydrogen bonding". In: *The Journal of Physical Chemistry B* 110.4 (2006), pp. 1928–1943.

[101] Yang Wang et al. "UVRR spectroscopy of the peptide bond. 1. Amide S, a nonhelical structure marker, is a C. alpha. H bending mode". In: *Journal of the American Chemical Society* 113.17 (1991), pp. 6359–6368.

[102] Cheng-Yen Huang, Gurusamy Balakrishnan, and Thomas G Spiro. "Protein secondary structure from deep-UV resonance Raman spectroscopy". In: *Journal of Raman Spectroscopy: An International Journal for Original Work in all Aspects of Raman Spectroscopy, Including Higher Order Processes, and also Brillouin and Rayleigh Scattering* 37.1-3 (2006), pp. 277–282.

[103] Gurusamy Balakrishnan et al. “Protein dynamics from time resolved UV Raman spectroscopy”. In: *Current opinion in structural biology* 18.5 (2008), pp. 623–629.

[104] Aleksandr V Mikhonin and Sanford A Asher. “Uncoupled peptide bond vibrations in α-helical and polyproline II conformations of polyalanine peptides”. In: *The Journal of Physical Chemistry B* 109.7 (2005), pp. 3047–3052.

[105] Eric S Manas et al. “Infrared spectra of amide groups in α-helical proteins: evidence for hydrogen bonding between helices and water”. In: *Journal of the American Chemical Society* 122.41 (2000), pp. 9883–9890.

[106] Reinhard Schweitzer-Stenner. “Advances in vibrational spectroscopy as a sensitive probe of peptide and protein structure: A critical review”. In: *Vibrational Spectroscopy* 42.1 (2006), pp. 98–117.

[107] Sanford A Asher, Alexander V Mikhonin, and Sergei Bykov. “UV Raman demonstrates that α-helical polyalanine peptides melt to polyproline II conformations”. In: *Journal of the American Chemical Society* 126.27 (2004), pp. 8433–8440.

[108] Pusheng Li et al. “UV resonance Raman ground and excited state studies of amide and peptide isomerization dynamics”. In: *Journal of the American Chemical Society* 119.5 (1997), pp. 1116–1120.

[109] Sunho Song et al. “Ultraviolet resonance Raman studies of trans and cis peptides: photochemical consequences of the twisted. pi.* excited state”. In: *Journal of the American Chemical Society* 113.4 (1991), pp. 1155–1163.

[110] Trace Jordan and Thomas G Spiro. “UV resonance Raman spectroscopy of cis—-amides”. In: *Journal of Raman Spectroscopy* 26.8-9 (1995), pp. 867–876.

[111] Erik Sedlák, Loren Stagg, and Pernilla Wittung-Stafshede. “Effect of Hofmeister ions on protein thermal stability: roles of ion hydration and peptide groups?” In: *Archives of Biochemistry and Biophysics* 479.1 (2008), pp. 69–73.

[112] Janet SW Holtz, Pusheng Li, and Sanford A Asher. “UV resonance Raman studies of cis-to-trans isomerization of glycyglycine derivatives”. In: *Journal of the American Chemical Society* 121.15 (1999), pp. 3762–3766.

[113] Ludmilla A Morozova-Roche et al. “Amyloid fibril formation and seeding by wild-type human lysozyme and its disease-related mutational variants”. In: *Journal of structural biology* 130.2-3 (2000), pp. 339–351.

[114] Erica Frare et al. "A highly amyloidogenic region of hen lysozyme". In: *Journal of molecular biology* 340.5 (2004), pp. 1153–1165.

[115] Fabrizio Chiti and Christopher M Dobson. "Protein misfolding, amyloid formation, and human disease: a summary of progress over the last decade". In: *Annual review of biochemistry* 86 (2017), pp. 27–68.

[116] Nunilo Cremades and Christopher M Dobson. "The contribution of biophysical and structural studies of protein self-assembly to the design of therapeutic strategies for amyloid diseases". In: *Neurobiology of disease* 109 (2018), pp. 178–190.

[117] AH Clark, GM Kavanagh, and SB Ross-Murphy. "Globular protein gelation—theory and experiment". In: *Food Hydrocolloids* 15.4-6 (2001), pp. 383–400.

[118] Walraj S Gosal et al. "Novel amyloid fibrillar networks derived from a globular protein: β-lactoglobulin". In: *Langmuir* 18.19 (2002), pp. 7174–7181.

[119] Walraj S Gosal, Allan H Clark, and Simon B Ross-Murphy. "Fibrillar β-lactoglobulin gels: Part 1. Fibril formation and structure". In: *Biomacromolecules* 5.6 (2004), pp. 2408–2419.

[120] Dmitry Kurouski, Richard P Van Duyne, and Igor K Lednev. "Exploring the structure and formation mechanism of amyloid fibrils by Raman spectroscopy: a review". In: *Analyst* 140.15 (2015), pp. 4967–4980.

[121] Christopher J Roberts. "Kinetics of irreversible protein aggregation: analysis of extended Lumry- Eyring models and implications for predicting protein shelf life". In: *The Journal of Physical Chemistry B* 107.5 (2003), pp. 1194–1207.

[122] Martino Calamai et al. "Reversal of protein aggregation provides evidence for multiple aggregated states". In: *Journal of molecular biology* 346.2 (2005), pp. 603–616.

[123] Rajaram Swaminathan et al. "Lysozyme: a model protein for amyloid research". In: *Advances in protein chemistry and structural biology*. Vol. 84. Elsevier, 2011, pp. 63–111.

[124] Mark RH Krebs et al. "Formation and seeding of amyloid fibrils from wild-type hen lysozyme and a peptide fragment from the β-domain". In: *Journal of molecular biology* 300.3 (2000), pp. 541–549.

[125] Shannon E Hill et al. "Amyloid protofibrils of lysozyme nucleate and grow via oligomer fusion". In: *Biophysical journal* 96.9 (2009), pp. 3781–3790.

[126] Samuele Raccosta, Vincenzo Martorana, and Mauro Manno. "Thermodynamic versus conformational metastability in fibril-forming lysozyme solutions". In: *The Journal of Physical Chemistry B* 116.40 (2012), pp. 12078–12087.

[127] Sian-Yang Ow and Dave E Dunstan. "The effect of concentration, temperature and stirring on hen egg white lysozyme amyloid formation". In: *Soft Matter* 9.40 (2013), pp. 9692–9701.

[128] Ming Xu et al. "Lysozyme fibrillation: deep UV Raman spectroscopic characterization of protein structural transformation". In: *Biopolymers: Original Research on Biomolecules* 79.1 (2005), pp. 58–61.

[129] Victor Shashilov et al. "Probing a fibrillation nucleus directly by deep ultraviolet Raman spectroscopy". In: *Journal of the American Chemical Society* 129.22 (2007), pp. 6972–6973.

[130] Mark RH Krebs, Glyn L Devlin, and AM Donald. "Protein particulates: another generic form of protein aggregation?" In: *Biophysical journal* 92.4 (2007), pp. 1336–1342.

[131] Lisa C Burnett et al. "A lysozyme concentration, pH, and time-dependent isothermal transformation diagram reveals fibrous amyloid and non-fibrous, amorphous aggregate species". In: *Open Journal of Biophysics* 2014 (2014).

[132] Samuele Raccosta et al. "Irreversible gelation of thermally unfolded proteins: structural and mechanical properties of lysozyme aggregates". In: *European Biophysics Journal* 39.6 (2010), pp. 1007–1017.

[133] Giovanna Navarra et al. "Characterization of the nucleation process of lysozyme at physiological pH: Primary but not sole process". In: *Biophysical Chemistry* 177 (2013), pp. 24–33.

[134] Shannon E Hill et al. "Spatial extent of charge repulsion regulates assembly pathways for lysozyme amyloid fibrils". In: *PLoS One* 6.4 (2011), e18171.

[135] Joseph Foley et al. "Structural fingerprints and their evolution during oligomeric vs. oligomer-free amyloid fibril growth". In: *The Journal of chemical physics* 139.12 (2013), 09B602_1.

[136] Mentor Mulaj, Joseph Foley, and Martin Muschol. "Amyloid oligomers and protofibrils, but not filaments, self-replicate from native lysozyme". In: *Journal of the American Chemical Society* 136.25 (2014), pp. 8947–8956.

[137] Tatiana Miti et al. "Stable, metastable, and kinetically trapped amyloid aggregate phases". In: *Biomacromolecules* 16.1 (2015), pp. 326–335.

[138] Filip Hasecke et al. "Origin of metastable oligomers and their effects on amyloid fibril self-assembly". In: *Chemical science* 9.27 (2018), pp. 5937–5948.

[139] Anika M Jonker, Dennis WPM Löwik, and Jan CM van Hest. "Peptide-and protein-based hydrogels". In: *Chemistry of Materials* 24.5 (2012), pp. 759–773.

[140] Subhadeep Das et al. "Amyloid fibrils: Versatile biomaterials for cell adhesion and tissue engineering applications". In: *Biomacromolecules* 19.6 (2018), pp. 1826–1839.

[141] Owen Griffith Jones and Raffaele Mezzenga. "Inhibiting, promoting, and preserving stability of functional protein fibrils". In: *Soft Matter* 8.4 (2012), pp. 876–895.

[142] Gang Wei et al. "Self-assembling peptide and protein amyloids: from structure to tailored function in nanotechnology". In: *Chemical Society Reviews* 46.15 (2017), pp. 4661–4708.

[143] Létitia Jean, Alex C Foley, and David JT Vaux. "The physiological and pathological implications of the formation of hydrogels, with a specific focus on amyloid polypeptides". In: *Biomolecules* 7.4 (2017), p. 70.

[144] Ruizhi Wang et al. "Gels of amyloid fibers". In: *Biomolecules* 9.6 (2019), p. 210.

[145] Hui Yan et al. "Thermoreversible protein hydrogel as cell scaffold". In: *Biomacromolecules* 7.10 (2006), pp. 2776–2782.

[146] Hui Yan et al. "Thermo-reversible protein fibrillar hydrogels as cell scaffolds". In: *Faraday Discussions* 139 (2008), pp. 71–84.

[147] H Yan et al. "Thermoreversible lysozyme hydrogels: properties and an insight into the gelation pathway". In: *Soft Matter* 4.6 (2008), pp. 1313–1325.

[148] Nicholas P Reynolds et al. "Engineered lysozyme amyloid fibril networks support cellular growth and spreading". In: *Biomacromolecules* 15.2 (2014), pp. 599–608.

[149] Ulyana Shimanovich et al. "Protein microgels from amyloid fibril networks". In: *ACS nano* 9.1 (2015), pp. 43–51.

[150] Taco Nicolai and Dominique Durand. "Controlled food protein aggregation for new functionality". In: *Current Opinion in Colloid & Interface Science* 18.4 (2013), pp. 249–256.

[151] Koen JA Jansens et al. “Rational design of amyloid-like fibrillary structures for tailoring food protein techno-functionality and their potential health implications”. In: *Comprehensive Reviews in Food Science and Food Safety* 18.1 (2019), pp. 84–105.

[152] Yiping Cao and Raffaele Mezzenga. “Food protein amyloid fibrils: Origin, structure, formation, characterization, applications and health implications”. In: *Advances in colloid and interface science* 269 (2019), pp. 334–356.

[153] Koen JA Jansens et al. “Conditions governing food protein amyloid fibril formation—Part I: Egg and cereal proteins”. In: *Comprehensive Reviews in Food Science and Food Safety* 18.4 (2019), pp. 1256–1276.

[154] Luben N Arnaudov and Renko de Vries. “Thermally induced fibrillar aggregation of hen egg white lysozyme”. In: *Biophysical journal* 88.1 (2005), pp. 515–526.

[155] Ye Zou et al. “Parallel β-sheet fibril and antiparallel β-sheet oligomer: New insights into amyloid formation of hen egg white lysozyme under heat and acidic condition from FTIR spectroscopy”. In: *The Journal of Physical Chemistry B* 117.15 (2013), pp. 4003–4013.

[156] Ye Zou et al. “New insight into amyloid fibril formation of hen egg white lysozyme using a two-step temperature-dependent FTIR approach”. In: *The Journal of Physical Chemistry B* 118.33 (2014), pp. 9834–9843.

[157] Sathyadevi Venkataramani, Jeremy Truntzer, and Denis R Coleman. “Thermal stability of high concentration lysozyme across varying pH: A Fourier Transform Infrared study”. In: *Journal of pharmacy & bioallied sciences* 5.2 (2013), p. 148.

[158] Chikashi Ota, Shintaro Noguchi, and Kouhei Tsumoto. “The molecular interaction of a protein in highly concentrated solution investigated by R aman spectroscopy”. In: *Biopolymers* 103.4 (2015), pp. 237–246.

[159] SR Al-Ayoubi et al. “Influence of cosolvents, self-crowding, temperature and pressure on the sub-nanosecond dynamics and folding stability of lysozyme”. In: *Physical Chemistry Chemical Physics* 19.22 (2017), pp. 14230–14237.

[160] Arne Schön et al. “Temperature stability of proteins: analysis of irreversible denaturation using isothermal calorimetry”. In: *Proteins: Structure, Function, and Bioinformatics* 85.11 (2017), pp. 2009–2016.

[161] Sara Catalini et al. “Probing Globular Protein Self-Assembling Dynamics by Heterodyne Transient Grating Experiments”. In: *Applied Sciences* 9.3 (2019), p. 405.

[162] Saba Suladze et al. “Probing volumetric properties of biomolecular systems by pressure perturbation calorimetry (PPC)–The effects of hydration, cosolvents and crowding”. In: *Methods* 76 (2015), pp. 67–77.

[163] N Harn et al. “Highly concentrated monoclonal antibody solutions: direct analysis of physical structure and thermal stability”. In: *Journal of pharmaceutical sciences* 96.3 (2007), pp. 532–546.

[164] Steven J Shire, Zahra Shahrokh, and JUN Liu. “Challenges in the development of high protein concentration formulations”. In: *Journal of pharmaceutical sciences* 93.6 (2004), pp. 1390–1402.

[165] Irina M Kuznetsova, Konstantin K Turoverov, and Vladimir N Uversky. “What macromolecular crowding can do to a protein”. In: *International journal of molecular sciences* 15.12 (2014), pp. 23090–23140.

[166] Germán Rivas and Allen P Minton. “Macromolecular crowding in vitro, in vivo, and in between”. In: *Trends in biochemical sciences* 41.11 (2016), pp. 970–981.

[167] Mimi Gao et al. “Crowders and cosolvents—major contributors to the cellular milieu and efficient means to counteract environmental stresses”. In: *ChemPhysChem* 18.21 (2017), pp. 2951–2972.

[168] R John Ellis and Allen P Minton. “Join the crowd”. In: *Nature* 425.6953 (2003), pp. 27–28.

[169] Jacob Blaffert et al. “Spectroscopic methods for assessing the molecular origins of macroscopic solution properties of highly concentrated liquid protein solutions”. In: *Analytical biochemistry* 561 (2018), pp. 70–88.

[170] Larissa A Munishkina et al. “The effect of macromolecular crowding on protein aggregation and amyloid fibril formation”. In: *Journal of Molecular Recognition* 17.5 (2004), pp. 456–464.

[171] Prasad S Sarangapani et al. “Critical examination of the colloidal particle model of globular proteins”. In: *Biophysical journal* 108.3 (2015), pp. 724–737.

[172] John T King et al. "Crowding induced collective hydration of biological macromolecules over extended distances". In: *Journal of the American Chemical Society* 136.1 (2014), pp. 188–194.

[173] Allen P Minton. "Influence of macromolecular crowding upon the stability and state of association of proteins: predictions and observations". In: *Journal of pharmaceutical sciences* 94.8 (2005), pp. 1668–1675.

[174] S Perticaroli et al. "Hydration and aggregation of lysozyme by extended frequency range depolarized light scattering". In: *Journal of Non-Crystalline Solids* 407 (2015), pp. 472–477.

[175] Francesco Sciortino et al. "Equilibrium cluster phases and low-density arrested disordered states: the role of short-range attraction and long-range repulsion". In: *Physical review letters* 93.5 (2004), p. 055701.

[176] Anna Stradner et al. "Equilibrium cluster formation in concentrated protein solutions and colloids". In: *Nature* 432.7016 (2004), pp. 492–495.

[177] Frédéric Cardinaux et al. "Cluster-driven dynamical arrest in concentrated lysozyme solutions". In: *The Journal of Physical Chemistry B* 115.22 (2011), pp. 7227–7237.

[178] Sha Wu, Yanwei Ding, and Guangzhao Zhang. "Mechanic insight into aggregation of lysozyme by ultrasensitive differential scanning calorimetry and sedimentation velocity". In: *The Journal of Physical Chemistry B* 119.52 (2015), pp. 15789–15795.

[179] Filip Meersman and Karel Heremans. "Temperature-induced dissociation of protein aggregates: accessing the denatured state". In: *Biochemistry* 42.48 (2003), pp. 14234–14241.

[180] Sara Catalini et al. "Amyloid Self-Assembly of Lysozyme in Self-Crowded Conditions: The Formation of a Protein Oligomer Hydrogel". In: *Biomacromolecules* (2021).

[181] Françoise Bonnete, S Finet, and A Tardieu. "Second virial coefficient: variations with lysozyme crystallization conditions". In: *Journal of crystal growth* 196.2-4 (1999), pp. 403–414.

[182] S Finet et al. "The Hofmeister effect as seen by SAXS in protein solutions". In: *Current Opinion in Colloid & Interface Science* 9.1-2 (2004), pp. 112–116.

[183] Andre Guinier and Gerard Fournet. "Small angle X-ray scattering". In: *New York* (1955).

[184] Mitsuhiro Hirai et al. "Small-angle X-ray scattering and calorimetric studies of thermal conformational change of lysozyme depending on pH". In: *The Journal of Physical Chemistry B* 102.7 (1998), pp. 1308–1313.

[185] Mitsuhiro Hirai et al. "Hierarchical map of protein unfolding and refolding at thermal equilibrium revealed by wide-angle X-ray scattering". In: *Biochemistry* 43.28 (2004), pp. 9036–9049.

[186] Shigeki Arai and Mitsuhiro Hirai. "Reversibility and hierarchy of thermal transition of hen egg-white lysozyme studied by small-angle X-ray scattering". In: *Biophysical journal* 76.4 (1999), pp. 2192–2197.

[187] Jenny Jie Yang, Maureen Pitkeathly, and Sheena E Radford. "Far-UV Circular Dichroism Reveals a Conformational Switch in a Peptide Fragment from the. beta.-Sheet of Hen Lysozyme". In: *Biochemistry* 33.23 (1994), pp. 7345–7353.

[188] Marcus Fändrich et al. "Myoglobin forms amyloid fibrils by association of unfolded polypeptide segments". In: *Proceedings of the National Academy of Sciences* 100.26 (2003), pp. 15463–15468.

[189] Paola Sassi et al. "Conformational changes in the unfolding process of lysozyme in water and ethanol/water solutions". In: *Journal of Molecular Liquids* 159.1 (2011), pp. 112–116.

[190] Alessandra Giugliarelli et al. "Vibrational circular dichroism spectra of lysozyme solutions: solvent effects on thermal denaturation processes". In: *The Journal of Physical Chemistry B* 117.9 (2013), pp. 2645–2652.

[191] Alain Hédoux et al. "Evidence of a two-stage thermal denaturation process in lysozyme: a Raman scattering and differential scanning calorimetry investigation". In: *The Journal of chemical physics* 124.1 (2006), p. 014703.

[192] Jane Clarke and Laura S Itzhaki. "Hydrogen exchange and protein folding". In: *Current opinion in structural biology* 8.1 (1998), pp. 112–118.

[193] Debra M Ferraro, Noel D Lazo, and Andrew D Robertson. "EX1 hydrogen exchange and protein folding". In: *Biochemistry* 43.3 (2004), pp. 587–594.

[194] Mallela MG Krishna et al. "Hydrogen exchange methods to study protein folding". In: *Methods* 34.1 (2004), pp. 51–64.

[195] David L Smith, Yuzhong Deng, and Zhongqi Zhang. "Probing the non-covalent structure of proteins by amide hydrogen exchange and mass spectrometry". In: *Journal of mass spectrometry* 32.2 (1997), pp. 135–146.

[196] Paola Sassi et al. "Unfolding and aggregation of lysozyme: A thermodynamic and kinetic study by FTIR spectroscopy". In: *Biophysical chemistry* 158.1 (2011), pp. 46–53.

[197] Sophie E Jackson. "How do small single-domain proteins fold?" In: *Folding and Design* 3.4 (1998), R81–R91.

[198] Alessandra Giugliarelli et al. "Denaturation and preservation of globular proteins: the role of DMSO". In: *The Journal of Physical Chemistry B* 116.45 (2012), pp. 13361–13367.

[199] A Giugliarelli et al. "Heat-denatured lysozyme aggregation and gelation as revealed by combined dielectric relaxation spectroscopy and light scattering measurements". In: *The Journal of Physical Chemistry B* 116.35 (2012), pp. 10779–10785.

[200] Daniel E Kuehner et al. "Lysozyme net charge and ion binding in concentrated aqueous electrolyte solutions". In: *The Journal of Physical Chemistry B* 103.8 (1999), pp. 1368–1374.

[201] Piero Chiarelli et al. "High frequency poroelastic waves in hydrogels". In: *The Journal of the Acoustical Society of America* 127.3 (2010), pp. 1197–1207.

[202] Piero Chiarelli et al. "Poroelastic longitudinal wave equation for soft living tissues". In: *Journal of Biorheology* 28.1 (2014), pp. 29–37.

[203] Andrea Taschin et al. "Supercooled water relaxation dynamics probed with heterodyne transient grating experiments". In: *Physical Review E* 74.3 (2006), p. 031502.

[204] LW Kessler and F Dunn. "Ultrasonic investigation of the conformal changes of bovine serum albumin in aqueous solution". In: *The Journal of physical chemistry* 73.12 (1969), pp. 4256–4263.

[205] G Pavlovskaya, DJ McClements, and MJW Povey. "Ultrasonic investigation of aqueous solutions of a globular protein". In: *Food hydrocolloids* 6.3 (1992), pp. 253–262.

[206] Milena Corredig and Douglas G Dalgleish. "Effect of temperature and pH on the interactions of whey proteins with casein micelles in skim milk". In: *Food Research International* 29.1 (1996), pp. 49–55.

[207] Alessandra Giugliarelli et al. “Spectroscopic and microscopic studies of aggregation and fibrillation of lysozyme in water/ethanol solutions”. In: *The Journal of Physical Chemistry B* 119.41 (2015), pp. 13009–13017.

[208] Irving M Klotz and Bruce H Frank. “Catalysis by imidazole of deuterium-hydrogen exchange in amide NH groups”. In: *Science* 138.3542 (1962), pp. 830–831.

[209] Paola Sassi et al. “Reversible and irreversible denaturation processes in globular proteins: from collective to molecular spectroscopic analysis”. In: *Journal of Raman Spectroscopy* 43.2 (2012), pp. 273–279.

[210] Hans-Jürgen Hinz and Frederick P Schwarz. “Measurement and analysis of results obtained on biological substances with dsc”. In: *The Journal of Chemical Thermodynamics* 33.11 (2001), pp. 1511–1525.

[211] Alice Blumlein and Jennifer J McManus. “Reversible and non-reversible thermal denaturation of lysozyme with varying pH at low ionic strength”. In: *Biochimica et Biophysica Acta (BBA)-Proteins and Proteomics* 1834.10 (2013), pp. 2064–2070.

[212] Milena Corredig, Marcela Alexander, and Douglas G Dalgleish. “The application of ultrasonic spectroscopy to the study of the gelation of milk components”. In: *Food research international* 37.6 (2004), pp. 557–565.

[213] Cory M Bryant and D Julian McClements. “Ultrasonic spectroscopy study of relaxation and scattering in whey protein solutions”. In: *Journal of the Science of Food and Agriculture* 79.12 (1999), pp. 1754–1760.

[214] Marcelo A Da Silva and Elizabeth PG Arêas. “Solvent-induced lysozyme gels: Rheology, fractal analysis, and sol–gel kinetics”. In: *Journal of colloid and interface science* 289.2 (2005), pp. 394–401.

[215] Giovanna Navarra et al. “Heat-and pH-induced BSA conformational changes, hydrogel formation and application as 3D cell scaffold”. In: *Archives of biochemistry and biophysics* 606 (2016), pp. 134–142.

[216] J Rzeszotarska and J Ranachowski. “The possibility of applying of acoustic methods for the monitoring of sol-gel processes”. In: *Archives of Acoustics* 25.1 (2000).

[217] David Linton Johnson. “Elastodynamics of gels”. In: *The Journal of Chemical Physics* 77.3 (1982), pp. 1531–1539.

[218] NG Parker and MJW Povey. "Ultrasonic study of the gelation of gelatin: phase diagram, hysteresis and kinetics". In: *Food Hydrocolloids* 26.1 (2012), pp. 99–107.

[219] J-C Bacri et al. "Ultrasonic waves: a tool for gelation process measurements". In: *Journal de Physique Lettres* 41.15 (1980), pp. 369–372.

[220] Michel Audebrand et al. "Investigation of gelation phenomena of some polysaccharides by ultrasonic spectroscopy". In: *Food hydrocolloids* 9.3 (1995), pp. 195–203.

[221] Dmitri I Svergun. "Small-angle X-ray and neutron scattering as a tool for structural systems biology". In: *Biological chemistry* 391.7 (2010), pp. 737–743.

[222] LA Feigin, Dimitrij I Svergun, et al. *Structure analysis by small-angle X-ray and neutron scattering*. Vol. 1. Springer, 1987.

[223] Dmitri I Svergun and Michel HJ Koch. "Small-angle scattering studies of biological macromolecules in solution". In: *Reports on Progress in Physics* 66.10 (2003), p. 1735.

[224] Andrew E Whitten and Jill Trewhella. "Small-angle scattering and neutron contrast variation for studying bio-molecular complexes". In: *Micro and nano technologies in bioanalysis*. Springer, 2009, pp. 307–323.

[225] Heimo Schnablegger and Yashveer Singh. "The SAXS guide: getting acquainted with the principles". In: *Austria: Anton Paar GmbH* (2011), pp. 1–124.